Fundamental Analysis of Self-healing Phenomena in Asphalt Mixtures

Samuel C. Leworthy
Thesis submitted to the University of Nottingham
for the degree of Doctor of Philosophy
Student No: 4243387

May 2022

Abstract

When asphalt becomes cracked it will slowly begin a self-healing process, during which, the crack is either partially or fully repaired over a period of time. Upon reaching a certain temperature the bitumen in the asphalt becomes a Newtonian fluid and the rate of this self-healing is greatly increased. This research discusses ways to model this process using flow within a porous medium and using the results produced to compare current popular methods of triggering self-healing in asphalt.

The first step of the research is to create a mathematical model for a gravity and surface tension driven self-healing process to model the flow of fluid within a porous medium. This was followed by the use of conformal mapping to discover a small time asymptotic solution to the movement of the bitumen into the crack. This precluded the creation of a numerical solution which used boundary integral methods combined with Green's functions to provide the equipment needed to allow the calculation of the crack healing with time. Next the numerical model was verified against the small time asymptotic solution as well as analytical solutions to ensure its reliability. In addition, experiments were conducted throughout the research to ensure the validity of the created model. The results of the numerical solution are then used to calibrate an equation which can predict the flow of bitumen into a crack in asphalt over time in a computationally cheap manner.

The next stage of the research uses the equation derived in the chapter previous to it and calibrates it to the results of experiments which use three point bending to analyse different healing methods. A set of these experiments are conducted as part of this research, while many experiments carried out in the literature are also studied. Three-point bending tests conducted in this research were performed on asphalt containing large quantities of calcium alginate capsules to aid the self-healing process. These tests showed consistently better healing in asphalt containing capsules, with the peak performance occurring in asphalt containing 1% or 1.25% capsules. Comparisons were then made between the various healing methods studied in the chapter.

The research concludes by creating new models to simulate the healing of different orientations of cracks in asphalt. The orientations are an inverted vertical crack, a horizontal crack and two vertical cracks in the same piece of asphalt. A numerical solution to the pressure gradient was found for each class of crack using boundary integral methods combined with Green's functions to select an appropriate domain for the calculations. These calculations were then validated through comparison to multiple series of laboratory experiments.

Acknowledgements

First and foremost I would like to thank my supervisors for the support and wisdom they have provided over the course of this research.

Secondly I would like to thank my family for all the moral support they gave as well as putting up with me moving back home this last year.

This research was funded by the Engineering and Physical Sciences Research Council.

Contents

Chapter 1

Introduction

1.1 Project Background

When asphalt gets cracked it will heal naturally over time [Menozzi et al., 2015]. This process is known as self-healing and if it can be enhanced greatly improves the lifespan of a road [Menozzi et al., 2015]. This research will focus on the creation of a gravity and surface tension driven model to describe the self-healing process as flow within a porous medium and using this to analyse various common methods used to accelerate the healing process.

Recently there has been a lot of research done on self-healing asphalt mixtures e.g. [Magnanimo et al., 2012, García et al., 2013, Menozzi et al., 2015], however there are still multiple conflicting viewpoints on which mechanics govern the process e.g. [Agzenai et al., 2015, García, 2012]. One of the main potential processes states that the flow of the bitumen into the crack is primarily being driven by gravity [García, 2012]. This research aims to investigate the mechanics behind a primarily gravity driven self-healing process accompanied by the effects of surface tension.

1.1.1 Varieties of Asphalt

In this research the main material being studied will be asphalt. This section will give an insight into what asphalt is, what it is composed of and the different types of asphalt available.

Asphalt is made of two main components, bitumen, also known as binder and aggregates. Bitumen is a long chain hydrocarbon and aggregates are small stones. When mixed together they form asphalt or tarmac.

As a clarification differences in American English and British English can cause some confusion with regards to asphalt. In American English the words asphalt and bitumen are interchangeable and refer to the British English bitumen or binder. Also, asphalt concrete is used to describe the combined mixture of aggregates and bitumen as opposed to the British English name of asphalt or tarmac. Here the British English convention will be used throughout.

Asphalt has two main uses, the most obvious being in roads. In addition, asphalt is also used to make approximately 94% of pavements worldwide [Agzenai et al., 2015].

The main types of asphalt used in road manufacture are asphalt concrete, rolled asphalt, mastic asphalt, porous asphalt, gussaphalt and stone mastic asphalt [Nicholls, 2014]. The differences in these types are caused by the proportions of aggregate and binder used to produce the asphalt, the sizes of the aggregates involved and the type of bitumen used.

Asphalt concrete is used in roads predominantly in the US and in Europe [Nicholls, 2014]. It uses a continuously graded aggregate to give it the highest proportion of aggregate to bitumen of all the varieties of asphalt listed here.

Rolled asphalt is also found in UK roads [Nicholls, 2014]. It is gap graded with no intermediate sized aggregates included in the mixture. The structure is such that the larger aggregates generally do not touch but are suspended in the binder. Rolled asphalt has a high bitumen content and relatively few air voids.

Mastic asphalt sees most of its use in bridges and other localized areas which require a high impermeability [Nicholls, 2014]. It is made up of only very large and very small aggregates, with no aggregates of intermediate size. Mastic asphalt has a relatively large proportion of bitumen to aggregate and a very low air void content.

Gussaphalt is another binder rich mixture which sees most of its use in Germany and surrounding countries [Nicholls, 2014]. It is similar to mastic asphalt in that it is gap graded with few intermediate size aggregates and a high proportion of bitumen.

Stone mastic asphalt is used when a more abrasion-resistant style of asphalt is required than gussphalt. It sees use in continental Europe and is slowly being introduced to the UK and US [Nicholls, 2014]. Stone mastic asphalt is gap graded and uses a strong skeleton of large stones as a base of the mixture, with gaps filled by binder and comparatively small aggregates.

Porous asphalt is seeing increased use due to its unique qualities [Nicholls, 2014] and is already used extensively in the Netherlands covering 90% of roads in the country [Liu, 2012]. Porous asphalt is open graded and contains mainly large aggregates and only enough bitumen to coat the asphalt. This means that it has by far the largest air void content of all the types of asphalt listed here with a minimum of 20% [Liu, 2012]. This type of asphalt has a few unique advantages over others when used in roads [Liu, 2012]. Firstly water can drain through the road meaning that puddles do not collect on its surface reducing the risk of skidding related accidents. It also reduces the noise pollution of cars by 3-4 dB compared to standard dense graded asphalt concrete. This however is contrasted by its decreased durability and vulnerability to ravelling, the loss of aggregate particles from the road surface [Liu, 2012].

1.1.2 Bitumen

Bitumen is one of the main components of asphalt and as such is worth investigating in more detail to lay a firm grounding for the topic. This section will cover the uses and composition of bitumen.

Bitumen has been used in road building as early as 2000 BC in Babylon [Nicholls, 2014]. It is a black tar-like substance which is mainly produced as a by-product of the fractional distillation of crude oil to produce more valuable materials often used as fuels. Bitumen is formed from the heavier compounds in crude oil which cannot be effectively used as commercial fuel. It is then sold on to companies for use mainly in roads, pavements and roof tiling.

By elemental composition bitumen is comprised of 80-88 wt.% carbon, 8-12 wt.% hydrogen, 0-9 wt.% sulphur, 0-2 wt.% oxygen and 0-2 wt.% nitrogen. Some trace metals can also found in most varieties [Lesueur, 2009]. In terms of molecular structure, according to the SARA model bitumen is made up of four main categories: saturates, asphaltenes, resins and aromatics [Lesueur, 2009].

Asphaltenes are a black powder at 20°C with a density of approximately 1.15 g/cm^3. They are mainly polar particles which are insoluble in n-heptane but soluble in toluene. In total asphaltenes make up 5-20 wt.% of bitumen and individually have a relatively high number average-molecular weight going from 800-3,500 g/cm^3. They have a solubility ranging from 17.6-21.7 MPa$^{0.5}$ [Lesueur, 2009].

Resins constitute 30-45 wt.% of a sample of bitumen. They are polar with an average molar mass of 1100 g/mol. Resins are a black solid at 20°C with a density of around 1.07 g/cm^3. They have a solubility parameter from 18.5-20 MPa$^{0.5}$ [Lesueur, 2009].

Aromatics usually make up the joint largest proportion of bitumen with resins at 30-45 wt.%. On average they have a relatively low molar mass of 800 g/mol. Aromatics are yellow to red in colour and are liquids at room temperature. Aromatics have a solubility parameter ranging from 17-18.5 MPa$^{0.5}$. At 20°C their density is approximately 1 g/cm^3 [Lesueur, 2009].

Saturates are the last of the main components of bitumen. They make up 0-15 wt.% of the total compound, are a colourless or lightly coloured at 20°C and density is roughly 0.9 g/cm^3. They have a solubility parameter of 15-17 MPa$^{0.5}$ [Lesueur, 2009].

As should be evident from the widely varying make up of bitumen, different samples can vary in properties but there are some generalisations which we can make. At low temperatures or high loading frequencies bitumen acts as an elastic solid however at high temperatures or low loading frequencies it acts as a Newtonian viscous fluid [García et al., 2013]. At intermediate temperatures and loading frequencies it demonstrates a viscoelastic response.

1.1.3 Crack Formation

As this research will go into detail on how cracks in asphalt can be healed it is first worth examining the types of cracks which can occur in asphalt and how they are formed.

There are many different types of cracks that can form in roads, all with varying causes. Often they are triggered by the repeated pressure or loading caused by traffic passing over the surface. Other causes include the road repeatedly shrinking and expanding with changes in temperature as well as degradation in an underlying layer of asphalt reflecting to the surface layer.

Block cracks are a series of large rectangular cracks [Juang and Amirkhanian, 1992] typically caused by shrinkage of the asphalt pavement as a result of temperature cycles. They are usually 30 cm or more.

Fatigue or alligator cracks form a group of blocks with an appearance resembling an alligator's skin. These differ from block cracks due to their irregular shape and are usually caused by load from traffic. The size of the blocks can range from a few centimetres to 0.914 m [Juang and Amirkhanian, 1992].

Transverse cracks run perpendicular to the centreline of the road while longitudinal cracks run parallel to the centreline of the road. They are usually found near the wheel tracks [Juang and Amirkhanian, 1992]. Neither type of crack are related to traffic loading and instead can be caused by shrinkage of the asphalt layer or cracks reflecting up from a covered layer of deteriorating asphalt. Edge cracks are a special type of longitudinal crack which can form at the edge of a road due to lack of support.

Potholes are bowl shaped holes in a layer of asphalt. They are a result of localised degradation under traffic [Juang and Amirkhanian, 1992].

1.1.4 Healing Mechanisms

After looking in detail on the subject of how cracks form, we now move on to the question of how these cracks can be repaired. In a generic material the process of healing or fatigue crack growth delay can be split into five different classifications [Suresh, 1998]. These range from mechanisms which act as the crack forms to those which act long-term.

The first of these classifications is plasticity induced healing. This is when the tip of the crack gets plastically deformed as the crack forms. When the pressure which caused the crack to form is removed some residual stress remains which reduces the initial size of the crack.

Oxide induced healing occurs when foreign material enters the crack and oxide on the surface of the crack. Depending on the size of the oxide layer formed this can go some way to reducing the size of a crack.

Thirdly there can be roughness induced effects. In a crack in a material there can be irregularities in the surface of said crack. These irregularities generally act counter to the healing process and can go as far as to prevent the crack from closing completely during healing.

Transformation induced healing occurs when the pressure change which results from the crack forming causes the material to undergo a change in phase. This can alter the propagation of the crack as it first forms.

When a viscous fluid can enter a fatigue crack this leads to viscous fluid induced healing. This can have two effects. Firstly, during the formation of the crack the fluid can change the initial propagation. Secondly when the crack begins to fill with fluid this unsurprisingly reduces the size of the crack.

This research will be looking at the last of these processes, viscous fluid induced healing. While some of the other types of crack growth delay do have some effect on the initial formation of a crack in asphalt; once the crack has formed this is the dominant healing process [Agzenai et al., 2015].

This naturally leads to the question of how the fluid, in this case bitumen, enters the crack. There are currently two main schools of thought on the driving process behind the bitumen entering the crack. Firstly, that it spreads from points in the crack which are in contact. The second possible process is gravity driven. Here bitumen fills the crack from the bottom upwards.

The thinking behind the first of these processes is that when part of the two faces of the crack are in contact molecules will diffuse from one face to the other [Little and Amit, 2007]. This initial contact of the two surfaces is compounded by van der Waals forces [Lytton, 2000]. The idea is that this diffusion will continue until the crack has completely healed [Little and Amit, 2007].

Another possibility is that the flow of bitumen into the crack is driven largely by gravity [García, 2012]. In this case bitumen from the surrounding asphalt would flow into the crack which would fill with bitumen, with the bottom of the crack healing first. In Fig. 1.1 and Fig. 1.2 it can clearly be seen that the crack begins to heal from the bottom, indicating the possible validity of this process. Gravity driven healing will be the main focus of this research.

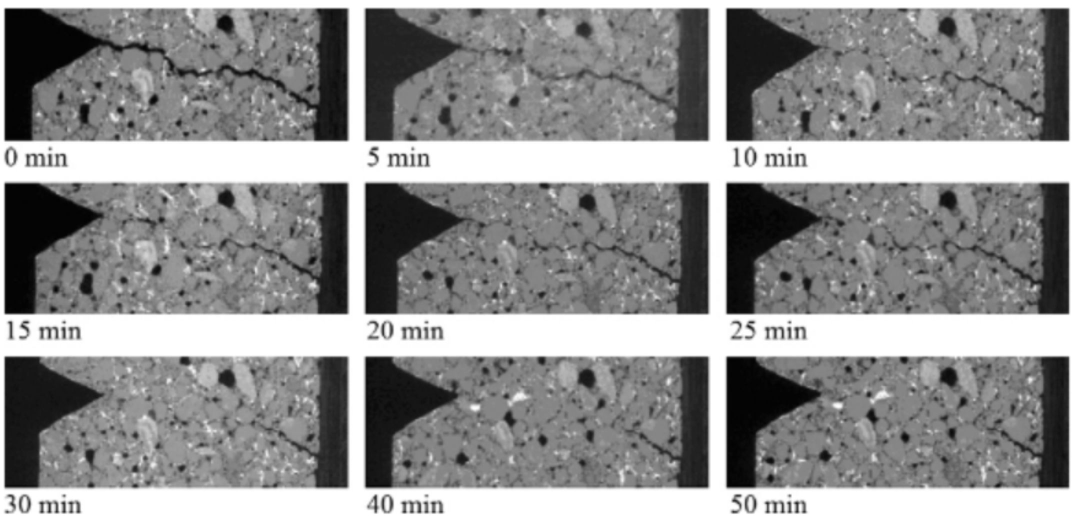

Figure 1.1: CT-scan images of a crack in asphalt healing. The images are turned 90°, during the experiment the triangular notch was at the bottom of the beam. Taken from [García, 2012].

1.1.5 Methods of Triggering Self-Healing

While the self-healing process does occur naturally the healing is too slow to repair roads under real conditions unless it can be triggered manually. To do this the viscosity of the bitumen in the road must be decreased or the crack must be healed by the introduction of another material. Currently there are three main ways of doing this, the first is introducing a chemical into the road which heals the crack. The second is to heat the road for long enough for the crack to heal. Finally something can be introduced to the road to cause the bitumen around the crack to soften. This section takes a closer look at exactly how these methods can be carried out.

One way of heating the road is to add steel wool to the asphalt during the mixing process. An induction heater can then be used to heat the steel wool which in turn heats

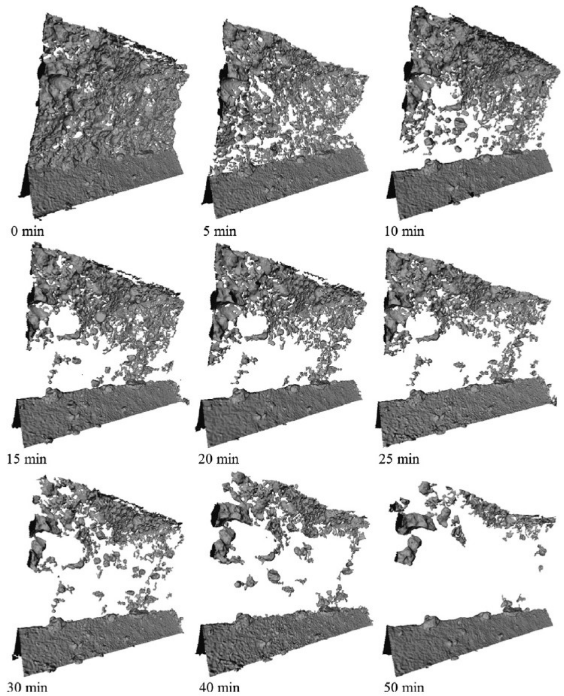

Figure 1.2: CT-scan of a crack healed at 70°C in an experiment done by García [2012].

the bitumen [García et al., 2013, García et al., 2012]. Roads with steel wool incorporated for this purpose have already been built [Liu, 2012].

Another way to heat the road is to use microwaves [Gallego et al., 2013, Norambuena-Contreras and Gonzalez-Torre, 2017, González et al., 2018, Norambuena-Contreras and Garcia, 2016]. These can be used to heat the surface of the road, the heat then diffuses through to the rest of the road. This process can be sped up by introducing steel wool into the asphalt to increase the thermal conductivity of the material. Microwaves need a smaller quantity of steel wool in the road than induction heating to be effective and the process uses less electricity than induction heating [Gallego et al., 2013].

On the chemical side of things microcapsules filled with a healing agent as well as catalysts can be mixed into asphalt when it is made [White et al., 2001]. These microcapsules then naturally break open when the asphalt around them cracks releasing the healing agent. When the crack grows large enough for the healing agent to also contact a catalyst the healing agent becomes polymerized and hardens, healing the crack. This process can be seen in Fig. 1.3.

One of the methods which will be examined in this research relates to the final method used to trigger the self-healing process. This method uses a different type of microcapsule, this time containing oil. When cracks form in the asphalt the capsules also crack and release oil into the surrounding asphalt. This lowers the viscosity of the surrounding bitumen and allows the crack to heal efficiently [Al-Mansoori et al., 2017b, Micaelo et al., 2016, Zhang et al., 2018, García et al., 2010, Norambuena-Contreras et al., 2018].

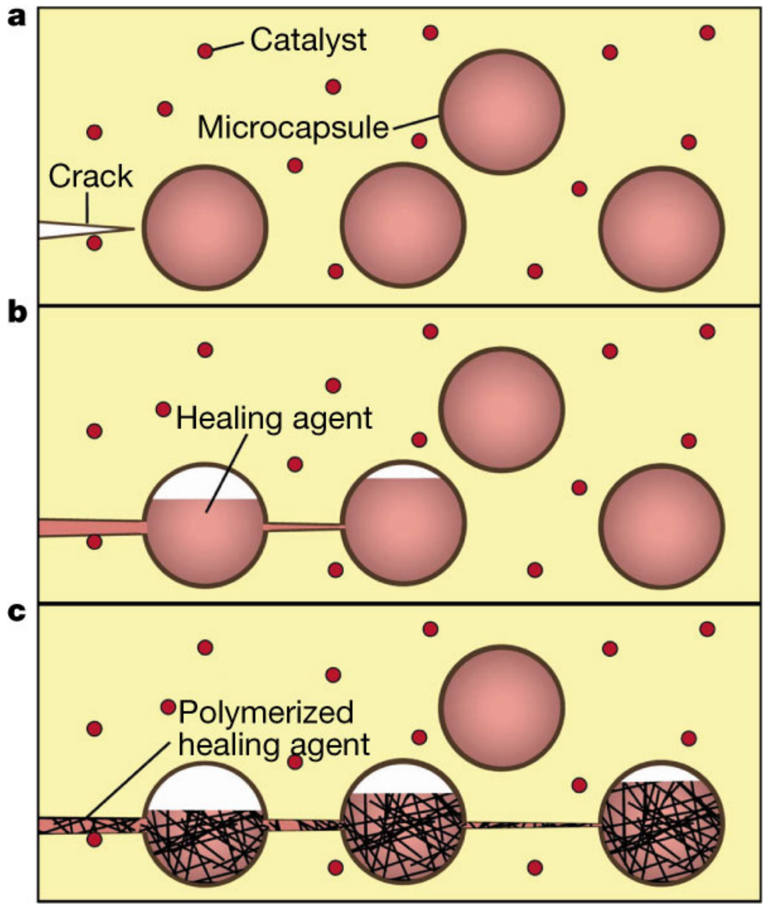

Figure 1.3: A visual explanation of the healing process assisted by micro-capsules. Section a. shows a crack forming. Section b. displays the crack breaking a microcapsule and the healing agent spreading through the crack. In section c. the healing agent comes into contact with the catalyst and becomes polymerized. Taken from [White et al., 2001].

1.1.6 Surface Tension, Surface Energy and Surface Free Energy

Now that the main methods of healing asphalt are understood it can be beneficial to look further into the role of surface tension which acts as one of the drivers in the healing process.

Surface energy and surface tension are quantities which for a liquid are numerically equal [Mondal et al., 2015, Hui and Jagota, 2013]. This has led the terms as well as surface free energy to sometimes be used interchangeably. However, there are differences between them.

Surface tension is a property of liquids caused by cohesive inter-molecular forces. These forces act to attract like molecules of the liquid to reduce its surface area. Surface tension has dimensions of force per unit length or equivalently energy per unit area and can be defined in terms of force by the equation [Egon, 1970]

$$\gamma = \frac{1}{2}\frac{F}{L}, \tag{1.1}$$

where γ is the surface tension of the liquid, F the force applied to it and L the length over which the force is applied.

The Laplace pressure, p_γ, is the component of the pressure difference on the surface of a fluid caused by surface tension. Across the interface of a curved surface with principal radii R_1 and R_2 this is given by the Young Laplace equation [Liu and Cao, 2016, Shuttleworth, 1950, Hui and Jagota, 2013]

$$p_\gamma = \gamma\left(\frac{1}{R_1} + \frac{1}{R_2}\right) \tag{1.2}$$

or equivalently [Duchesne et al., 2019]

$$p_\gamma = \gamma\kappa. \tag{1.3}$$

Here κ is the curvature of the surface, given by the sum of the principal radii. For a spherical surface this reduces to [Goldman, 2009, Pellicer et al., 2000]

$$p_\gamma = \frac{2\gamma}{r}, \tag{1.4}$$

where r is the radius of the surface.

Surface energy or interfacial free energy is the energy needed to create a unit area of new surface of a material by the process of division [Mondal et al., 2015].

The definition of surface energy is given by [Ip and Toguri, 1994]

$$u^s = \frac{U^s}{A}, \tag{1.5}$$

where u^s is the surface energy of a material, U^s is the internal energy of the surface and A is the area of the interface.

Surface free energy is similar to surface energy but instead of being defined by the internal energy of the material it is instead defined using the Helmholtz free energy, F^s, given by [Timmes and Swesty, 2000, Ip and Toguri, 1994]

$$F^s = U^s - TS, \tag{1.6}$$

where T is the absolute temperature of the surroundings and S is the entropy of the system. The surface free energy, f^s, is given by [Ip and Toguri, 1994]

$$f^s = \frac{F^s}{A}. \tag{1.7}$$

While for a one component system surface free energy and surface tension are numerically equal [Ip and Toguri, 1994], for an isotropic substance or crystal face the relationship between surface tension and surface free energy is given by [Shuttleworth, 1950, Egon, 1970]

$$\gamma = f^s + A\left(\frac{df^s}{dA}\right). \tag{1.8}$$

Multiple methods can be used to discover the surface energy. Most common are the contact angle methods including the Wilhelmy plate measurement e.g. [Cheng, 2003, Elphingstone Jr, 1998, Drelich and Miller, 1994, Drelich et al., 1994, Hefer et al., 2006a] and sessile drop e.g. [Tan and Guo, 2013, Papirer et al., 1987, Vargha-Butler et al., 1988, Wei et al., 2014] measurement due to their convenience. In addition other methods can be used, such as inverse gas chromatography e.g. [Hefer et al., 2006b, Papirer et al., 1985, Puig et al., 2004], atomic force microscopy e.g. [Pauli et al., 2003] and nuclear magnetic resonance e.g. [Miknis et al., 2005].

To find the surface energy of a solid using contact angles place a drop of liquid with known surface energy γ_l, as well as dispersion γ_l^{d} and polar components γ_l^{p}. Next measure the contact angle θ and plot

$$\gamma = \frac{1+\cos\theta}{2}\frac{\gamma_1}{\sqrt{\gamma_l^{\mathrm{d}}}} \tag{1.9}$$

against

$$\sqrt{\frac{\gamma_l^{\mathrm{p}}}{\gamma_l^{\mathrm{d}}}}. \tag{1.10}$$

Here the square of the slope and the intercept result in the polar and dispersion components of the surface area of the solid respectively [Wei and Zhang, 2010].

1.1.7 Boundary Integral Methods

After looking at the underlying mechanics which impact the healing process thought now needs to be given to how best to calculate the movement of the interface of the bitumen with time. This research will use boundary integral methods to construct a numerical solution to the healing of a crack in asphalt.

Boundary integral methods can be used to compute the movement of an interface over time and are often applied to problems where the properties of a fluid or material change abruptly at an interface [Hou et al., 2001]. While it is very common for boundary integral methods to be applied to two dimensional flow e.g. [Boulton-Stone, 1993, Toose et al., 1995, Rahimian et al., 2010, Meiron, 1986, Power, 1993] using them to model three dimensional flow is also an active area of research e.g. [Klaseboer et al., 2009, Sheng et al., 1998, Cao et al., 1991]. In addition to their common use in fluid mechanics boundary integral methods also see use in acoustics e.g. [Chandler-Wilde et al., 2012, Hsiao and Wendland, 2000, Meyer et al., 1978], electromagnetics e.g. [Liu and Jin, 2001, Collino et al., 2008, Schlemmer et al., 1992] where the technique is usually referred to as the method of moments as well as fracture mechanics e.g. [Minghao et al., 1994, Mi and Aliabadi, 1992, Tan and Fenner, 1979] and contact mechanics e.g. [Alessandri and Mallardo, 1999, Liu and Tan, 1992]. Boundary integral methods are of particular interest for this research because they offer an efficient method of calculating the movement of an interface over time. This lends itself well to the problem of viscous flow with a defined boundary layer moving through a porous medium.

Other methods which can be used to solve similar problems include: volume of fluids e.g. [Hirt and Nichols, 1981, Welch and Wilson, 2000], immersed interface methods e.g. [Lee and LeVeque, 2003, Xu and Wang, 2006], level set e.g. [Olsson and Kreiss, 2005, Sussman et al., 1998], front-tracking e.g. [Unverdi and Tryggvason, 1992, Hua et al., 2008] and finite differences methods e.g. [Narasimhan and Witherspoon, 1976, van Vossen et al., 2002]. When the restrictions of the method allow boundary integral methods to be applied to a problem it generally outperforms the others in terms of accuracy and efficiency [Hou et al., 2001]. This efficiency is due to the fact that using boundary integral methods requires only the interface to be discretised as opposed to having to discretise the entire domain as is the case with many of the above methods [Khalid, 2015].

Boundary integral methods usually function by forming an integral equation along the interface, referred to as a boundary integral equation [Khalid, 2015]. These boundary integral equations are either formulated using complex variable methods such as those seen in [Huang et al., 2006, Wang et al., 2003, Schultz and Hong, 1989] or based on Green's third identity e.g. [Martin and Rizzo, 1995, Bigoni and Capuani, 2005, Jensen and Freeze, 1998]. The method used to formulate the equation in this research will take a Green's identity approach.

1.1.8 Modelling Porous Media Using a Hele-Shaw Cell

Now that a method of calculating the flow of bitumen has been found there is value in examining how the conditions which will be modelled can be replicated as closely as possible in a laboratory setting. For this a Hele-Shaw cell will be used.

The Hele-Shaw cell was developed by Henry Selby Hele-Shaw as a means of showing the movement of a fluid around an obstacle in a flow using a lantern as a projector and consists of a viscous fluid in between two parallel plates [Vasil'ev, 2009].

Experimentally a porous medium can be approximated to by using a Hele-Shaw cell [Oltean et al., 2008]. This is because a Hele-Shaw cell acts as one large pore in a porous medium but provided the distance between the plates is minimal the fluid will at all points be close to a stationary surface and so is subject physical constraints similar to those which would be found in a true porous medium.

For the approximation of a Hele-Shaw cell to a porous medium to hold

$$\frac{h}{\delta} \ll 1 \tag{1.11}$$

and

$$\frac{Uh^2}{\nu\delta} \ll 1 \tag{1.12}$$

must must be true within the cell [Nield and Bejan, 2006]. Here h is the size of the gap in between the two plates, δ is the smallest length scale of the motion to be modelled, U is the fluid's velocity and ν is the kinematic viscosity of the fluid. The first restriction is necessary to ensure that there is negligible advection of vorticity, acting to reduce the spread of any rotational motion in the fluid. The second enforces rapid diffusion of vorticity. This makes sure that the intensity of any rotational movement in the fluid will decrease with time.

In addition, when thermal diffusivity is being studied in a Hele-Shaw cell

$$\frac{Uh^2}{\alpha_f \delta} \ll 1 \tag{1.13}$$

must hold [Nield and Bejan, 2006], where α_f is the thermal diffusivity of the liquid. This restriction ensures that any changes in temperature will quickly diffuse across the material in the cell.

The Hele-Shaw-cell forms an ideal porous medium and has a permeability, k of [Gupte and Advani, 1997]

$$k = \frac{1}{12}h^2. \tag{1.14}$$

When the inside of the Hele-Shaw cell is entirely comprised of the fluid being studied the porosity, $\phi = 1$ by definition.

The ability of a Hele-Shaw cell to approximate a porous medium is one which will be used throughout this research to in order to perform experiments which can be used to validate the numerical results produced.

1.2 Outline of Thesis Contributions

This research is split into three main sections. The first examines the two dimensional case of a crack in bitumen healing over time. The second uses the results from the first section to investigate the behaviour of asphalt being cracked and re-healed in laboratory conditions. The third section of the research uses similar methods to the first section to investigate the behaviour of two dimensional cracks in different orientations.

Firstly, the construction of a model based on gravity and surface tension driven flow will take place. The model will feature an incompressible fluid flowing through a semi-infinite porous medium. Here it will be assumed that the flow of bitumen throughout the system will be characterised as flow within a porous medium including within the crack.

A novel result presented in this thesis will be the use of conformal mapping to calculate the pressure field of the surroundings of a crack. Multiple cases will be examined here including that of an infinitesimally thin crack and an idealised triangular crack. In addition an approximate solution to the pressure profile for a generic crack and the tip of a crack will be given. The calculations from this will give a small time asymptotic solution to the initial movement of the bitumen.

After this, the boundary integral method will be applied to provide a numerical solution to the problem being modelled across multiple different domain types. The novelty of this is its use to create simulations of a crack evolving in this context.

Next, a series of novel experiments will be discussed. These will examine flow of bitumen within a Hele-Shaw cell to simulate a porous medium. In this research the results of these experiments will be used to validate the model.

The chapter will conclude with the numerical results being used to calibrate a novel equation which can predict the healing level of a crack with time. This will result in a computationally cheap method of predicting the healing of a crack with time. This equation will also be used when analysing various healing methods in the next chapter.

In the third chapter of the thesis a series of three-point bending tests on asphalt containing a large quantity of oil capsules will be performed. Here the novelty lies in the large proportion of oil capsules which make up the asphalt being broken and healed.

The equation for crack healing from chapter 2 will be utilised to generate a novel equation to calculate the force required to break a partially healed beam using three-point bending. A large sample of healing results using different healing methods and different styles of asphalt will be analysed and used to calibrate the equation for crack healing with time for the appropriate healing method and type of asphalt.

To test the safety of using high quantities of oil capsules in asphalt pendulum tests have been conducted on the beams. The results from these experiments will show that asphalt containing high levels of oil capsules meets the frictional requirements for road surfaces.

The last novel result of the chapter will be derived by extrapolating the healing profiles of three-point bending experiments in the literature. Here the conclusion is reached that the lack of apparent healing which occurs in asphalt when samples have healed to 50% of their original strength is in fact only a temporary plateau caused by the mechanics of the three-point bending test commonly used to test healing.

To begin the next chapter of the thesis, a mathematical model will be constructed for three different types of crack to predict the flow of bitumen under the effects of surface tension and gravity. The flow here will be assumed to be characterised as flow within a porous medium in all parts of the system including within the crack. This will order to build a strong framework for the rest of the chapter to draw from. Here the differences in healing mechanics and initial conditions will be clarified.

Next, the boundary integral method will be applied to the cracks detailed in the model, providing a numerical solution. This will take place over multiple different domain types and for three distinct styles of crack. Here the novelty is in the use of the method to create simulations of cracks healing in this context.

To conclude the chapter another series of experiments, similar in style to those from the 2nd chapter of this research will be discussed. These experiments provide a novel way of approximating flow of bitumen into a crack in a porous medium. Here they will also be used to validate the model produced in the chapter.

Chapter 2

Slow, Gravity and Surface Tension Driven Filling of a Crack in a Porous Medium

2.1 Introduction

The main property of asphalt that is under investigation in this research is its self-healing ability. When asphalt becomes cracked the bitumen in the asphalt will slowly flow back into the crack [Tabaković and Schlangen, 2016], a process which, when triggered manually, can increase the lifetime of roads by up to 31% [Menozzi et al., 2015]. This process has been looked at from a variety of perspectives from focused discussions of the chemistry of asphalt e.g. [Pauli, 2014] to more general mathematical models of crack propagation e.g. [Roper and Lister, 2005, Roux et al., 1998]. Heating the bitumen in the road causes it to become a Newtonian fluid, decreasing its viscosity and dramatically increases the speed of the process [García et al., 2013].

The main approach used in current research on the healing of cracks in asphalt is to assume that bitumen mainly spreads from points in the crack which are in contact [Magnanimo et al., 2012, Agzenai et al., 2015, Menozzi et al., 2015]. Here when part of the two faces of the crack are in contact molecules will diffuse from one face to the other [Little and Amit, 2007]. This initial contact of the two surfaces is compounded by van der Waals forces [Lytton, 2000]. The idea is that this diffusion will continue until the crack has completely healed [Little and Amit, 2007].

However research by [García, 2012] indicates that flow of bitumen into the crack is driven largely by gravity. In this case bitumen from the surrounding asphalt would flow into the crack which would heal the bottom of the crack much faster than the top. Here the effects of gravity and surface tension will both be used to simulate the self healing of asphalt. This gives a new perspective on the self-healing of asphalt and allows detailed predictions to be made to describe the rate at which it occurs.

Firstly a model will be constructed based on the flow of bitumen within a driven by gravity and surface tension. The flow will be characterised as flow within a porous medium throughout the system, including within the crack. After this the small time asymptotic solution using conformal mapping will be examined to give an initial time step when simulating the movement of bitumen. This will be followed by a numerical solution using boundary integral methods. Next the numerical solution will be trialled against real world experiments to validate the reliability of the simulation. Finally the results of the numerical method will be used to calibrate an equation for the progress of a crack healing in asphalt. This equation will offer a computationally cheap method of predicting the progress of the healing of cracks in asphalt with time.

2.2 Theory

This section of the thesis will focus on creating a theoretical framework on which the research will be based.

This will begin with the creation of a mathematical model which will lay out the base assumptions of the research and describe the problem being investigated in detail.

Next this will be followed by the calculation of the small time asymptotic solution for each case. This solution obtained via conformal mapping will allow for the calculation of the initial movement of the system for each domain being examined.

This will be followed by an explanation of how boundary integral methods can be used to compute a numerical solution to the movement of the interface of the bitumen over time.

2.2.1 The Mechanics of Fluid Moving into a Crack in a Porous Medium

Initially we consider the two dimensional movement of bitumen, a Newtonian fluid in a semi-infinite domain. We assume that both the width and depth of the system as seen in Fig. 2.1 is large enough to be considered infinite.

The model assumes that the bitumen is encased in a porous medium and flows into a thin crack absent of bitumen, filling it over time under the dual influences of gravity and surface tension. Here movement of bitumen within the crack itself is also characterised as flow within a porous medium. This assumption of movement within the crack being considered movement within a porous medium is made because it is not uncommon for asphalt to have areas between aggregates measuring multiple millimetres. As cracks in asphalt are in general of negligible distance in comparison to this, any movement of bitumen within the crack will take place sufficiently close to aggregates for it to be influenced by them as it would be throughout the rest of the material. For wider cracks this assumption breaks down and the internals of the crack should be modelled as a void with the movement of the bitumen inside governed by Stokes flow, however this case is outside the scope of this research.

The boundary of the fluid at time t lies at $y = Y(x,t)$. At $t = 0$ this is $y = Y_0(x)$. The pressure and velocity fields are given by $p(x,y,t)$ and $\mathbf{u}(x,y,t)$ respectively. Here x and y are Cartesian co-ordinates in the horizontal and vertical directions respectively. Under these conditions the fluid in the porous medium is subject to Darcy's law [Neuman,

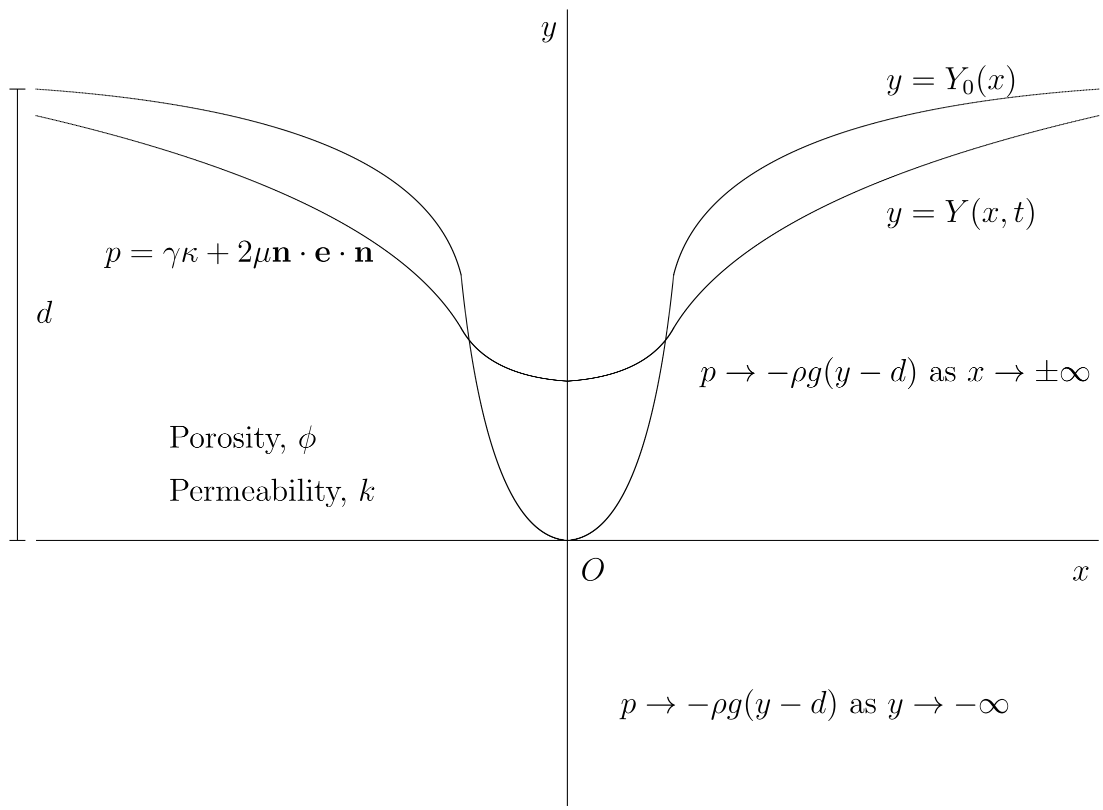

Figure 2.1: A crack of height d formed in asphalt with porosity ϕ and permeability k. The line $y = Y(x)_0$ gives the initial position of the boundary of the bitumen and the line $y = Y(x,t)$ gives the position of the boundary of the bitumen at a later time t.

1977, Liu and Ma, 2020, Niessner et al., 2011], which can be written as

$$\mathbf{u} = -\frac{k}{\phi\mu}\nabla\left(p - \rho g y\right). \tag{2.1}$$

The fluid is also subject to conservation of mass [Markov, 2007, Whitaker, 1986, Liu and Ma, 2020, Gresho and Sani, 1987] which for an incompressible fluid is given by

$$\nabla\cdot\mathbf{u} = 0 \tag{2.2}$$

or if you substitute (2.1) into this

$$\frac{k}{\phi\mu}\nabla^2\left(p - \rho g y\right) = 0. \tag{2.3}$$

In these equations k is the permeability of the porous medium, μ is the kinematic viscosity of the bitumen, ϕ is the porosity of the asphalt, ρ is the density of the fluid and g is acceleration due to gravity.

For an incompressible Newtonian fluid the stress tensor, $\boldsymbol{\sigma}$, on the interface is given by [Batchelor, 2000, Duchesne et al., 2019]

$$\boldsymbol{\sigma} = -p\mathbf{I} + 2\mu\mathbf{e}, \tag{2.4}$$

where $\mathbf{I}$ is the identity matrix and $\mathbf{e}$ is the rate of strain tensor which is expressed by

$$\mathbf{e} = \frac{1}{2}\left(\nabla\mathbf{u} + (\nabla\mathbf{u})^T\right), \tag{2.5}$$

with $(\nabla\mathbf{u})^T$ being the transpose of $\nabla\mathbf{u}$. At each point on the surface this can be split into a normal and tangential component.

As the interface of the bitumen is considered to be a free surface the tangential term vanishes [Batchelor, 2000]. This is expressed by the equation

$$\mathbf{n} \cdot \left(\nabla\mathbf{u} + (\nabla\mathbf{u})^\top\right) \cdot \mathbf{t} = 0, \tag{2.6}$$

where $\mathbf{n}$ and $\mathbf{t}$ represent the normal and tangential vectors to the surface respectively.

The normal component is given by

$$p - p_\mu = p_e + p_\gamma. \tag{2.7}$$

Here p_μ, the viscous pressure can be represented by

$$p_\mu = 2\mu\mathbf{n} \cdot \mathbf{e} \cdot \mathbf{n}. \tag{2.8}$$

In the model it is assumed that external pressures are negligible and so the external pressure term, p_e, is taken to be 0. Finally the Laplacian pressure, p_γ, resulting from surface tension at the free surface is given by the Young-Laplace equation [Liu and Cao, 2016, Shuttleworth, 1950, Hui and Jagota, 2013]

$$p_\gamma = \frac{\gamma}{r} = \gamma\kappa. \tag{2.9}$$

Here γ is surface tension and κ is the curvature of the surface. Given that the surface here is modelled as 2D the radius of curvature with axis in the x direction is considered to be infinite meaning that the radius of curvature on the axis parallel to the surface, r, is the only radius of curvature which needs to be considered. The sign of r is taken to be positive when the surface is convex and negative when the surface is concave, a factor which varies depending on the part of the surface being observed. Given these substitutions (2.7) reduces to

$$p = \gamma\kappa + 2\mu\mathbf{n} \cdot \mathbf{e} \cdot \mathbf{n}. \tag{2.10}$$

At the free surface these equations also need to be solved subject to the kinematic condition [Cruse and Rizzo, 1968], which relates the motion of the free surface to the fluid velocity at the surface. This is given by

$$\frac{\partial Y}{\partial t} + u\frac{\partial Y}{\partial x} = v, \tag{2.11}$$

where u is velocity in the x direction and v is velocity in the y direction.

Now the substitution $\bar{p} = p + \rho g\,(y - d)$ will be used to create a modified pressure field $\bar{p}$ and simplify many of the following equations. Here d is the initial height of the crack.

In addition, from this point forwards all quantities will be given in dimensionless variables with length, pressure, time and velocity being scaled with d, $\rho g d$, $\frac{\phi \mu d}{\rho g k}$ and $\frac{\rho g k}{\phi \mu}$ respectively. Therefore let the new non-dimensionalised variables be given by $\hat{x} = \frac{x}{d}$, $\hat{y} = \frac{y}{d}$, $\hat{Y} = \frac{Y}{d}$, $\hat{p} = \frac{\bar{p}}{\rho g d}$, $\hat{t} = t\frac{\rho g k}{\phi \mu d}$, $\hat{\mathbf{e}} = \mathbf{e}\frac{\phi \mu d}{\rho g k}$, $\hat{\mathbf{u}} = \mathbf{u}\frac{\phi \mu}{\rho g k}$ and $\hat{\kappa} = d\kappa$.

Given this, for $\hat{t} \geqslant 0$ and $-\infty < \hat{x} < \infty$ the governing equations can be simplified to

$$\hat{\mathbf{u}} = -\nabla \hat{p} \tag{2.12}$$

as well as

$$\nabla^2 \hat{p} = 0 \tag{2.13}$$

when $\hat{y} \leqslant \hat{Y}\left(\hat{x}, \hat{t}\right)$.

On the surface of the fluid the stress jump condition becomes

$$\hat{p} = \frac{\hat{\kappa}}{Bo} + (\hat{y} - 1) + \delta \hat{\mathbf{n}} \cdot \hat{\mathbf{e}} \cdot \hat{\mathbf{n}} \tag{2.14}$$

and

$$\delta \hat{\mathbf{n}} \cdot \hat{\mathbf{e}} \cdot \hat{\mathbf{t}} = 0 \tag{2.15}$$

when expressed in the dimensionless variables. Here $\hat{\mathbf{n}}$ and $\hat{\mathbf{t}}$ represent the normal and tangential vectors in the dimensionless co-ordinate system. The Bond number is given by the equation

$$Bo = \frac{\rho g d^2}{\gamma}, \tag{2.16}$$

while the dimensionless parameter δ can be expressed as

$$\delta = 2\frac{k}{\phi d^2}. \tag{2.17}$$

Examining the expected values of δ here can help justify an approximation which simplifies the mathematics of the model considerably. In the case of asphalt, the value of δ can be determined by calculating from experimental values. The asphalt created for use in the next chapter of this research has a bitumen content of 4.5% and an air void content of 4.5% so here we can take the porosity as $\phi = 0.09$. The height of asphalt samples used in the next chapter was 60 mm so we can take $d = 0.06$ as a representative quantity here. In a study by [Giompalo, 2010] permeability of representative samples of hot mix asphalt with binder content between 5.2-6.7% with air void content between 3.9-8.5% was found to be between $4 \times 10^{-9} - 2.367 \times 10^{-6}$. Here values of permeability increased rapidly with larger air void contents. This gives a reasonable range of expected values of δ in asphalt as $2.4 \times 10^{-5} - 1.5 \times 10^{-2}$ ms^{-1}.

The other case of relevance to this research is that of a Hele-Shaw cell, in which experiments can be performed in a manner which simulates a porous medium. Here k can be found using (1.14) which can be combined with the fact that by definition $\phi = 1$ within a Hele-Shaw cell to reduce the relationship to

$$\delta = \frac{h^2}{6d^2}. \tag{2.18}$$

Here h is the width of the Hele-Shaw cell. This means that in the situations evaluated in this research where $d \gg h$ the condition $\delta \ll 1$ will hold for the movement of fluid in a Hele-Shaw cell.

Given these values it will be assumed throughout this research that $\delta \ll 1$. This means that at leading order (2.14) reduces to

$$\hat{p} = \frac{\hat{\kappa}}{Bo} + \hat{y} - 1. \tag{2.19}$$

When expressed in dimensionless variables the kinematic condition remains as

$$\frac{\partial \hat{Y}}{\partial \hat{t}} + \hat{u}\frac{\partial \hat{Y}}{\partial \hat{x}} = \hat{v}. \tag{2.20}$$

Here $\hat{u}$ and $\hat{v}$ are the dimensionless velocity components in the $\hat{x}$ and $\hat{y}$ directions respectively.

In addition the following boundary conditions apply:

$$\hat{\mathbf{u}} \to 0,\ \hat{p} \to 0 \ \text{ as } \ \hat{y} \to -\infty \tag{2.21}$$

as well as

$$\hat{\mathbf{u}} \to 0,\ \hat{p} \to 0 \ \text{ as } \ \hat{x} \to \pm\infty \tag{2.22}$$

and

$$\hat{\mathbf{u}} = 0,\ \hat{Y}\left(\hat{x}, \hat{t}\right) = \hat{Y}_0\left(\hat{x}\right) \ \text{ when } \ \hat{t} = 0. \tag{2.23}$$

Here $\hat{Y}_0\left(x\right)$ is the initial displacement of the free surface.

While a semi-infinite domain is better suited to modelling the reality of a crack in asphalt being healed, a series of experiments will be conducted throughout this research which can be better modelled by using a finite domain. When comparing the model to experiments the system will have boundaries at a known depth and width through which bitumen cannot pass. Here the velocity of the bitumen on the boundaries will be 0 in accordance with the no-slip and no-penetration conditions [Richardson, 1973].

2.2.2 Conformal Mapping of an Infinitesimally Thin Crack

The most basic form of this problem is looking at a scenario with an infinitesimally thin crack at time $\hat{t} = 0$ as can be seen in Fig. 2.2. Here we can use conformal mapping to transform layout the crack into a half plane in the complex plane. This will allow the pressure across the domain to be calculated which in turn can be used to find the small time asymptotic solution to the advection of the interface of the crack.

For the infinitesimally thin crack being reviewed here the surface is flat meaning that the curvature of the interface is 0 when $\hat{t} = 0$, with the exception of the corners of the surface. Hence, the small time asymptotic solution will be valid in the neighbourhood away from a small area containing the corners of the system. Given this the surface tension term is 0 on the edges of the interface and the pressure in the crack is taken to be $\hat{p} = \hat{y}_1 - 1$. Conformal mapping can then be used to obtain the small time asymptotic solution for the simulation as follows.

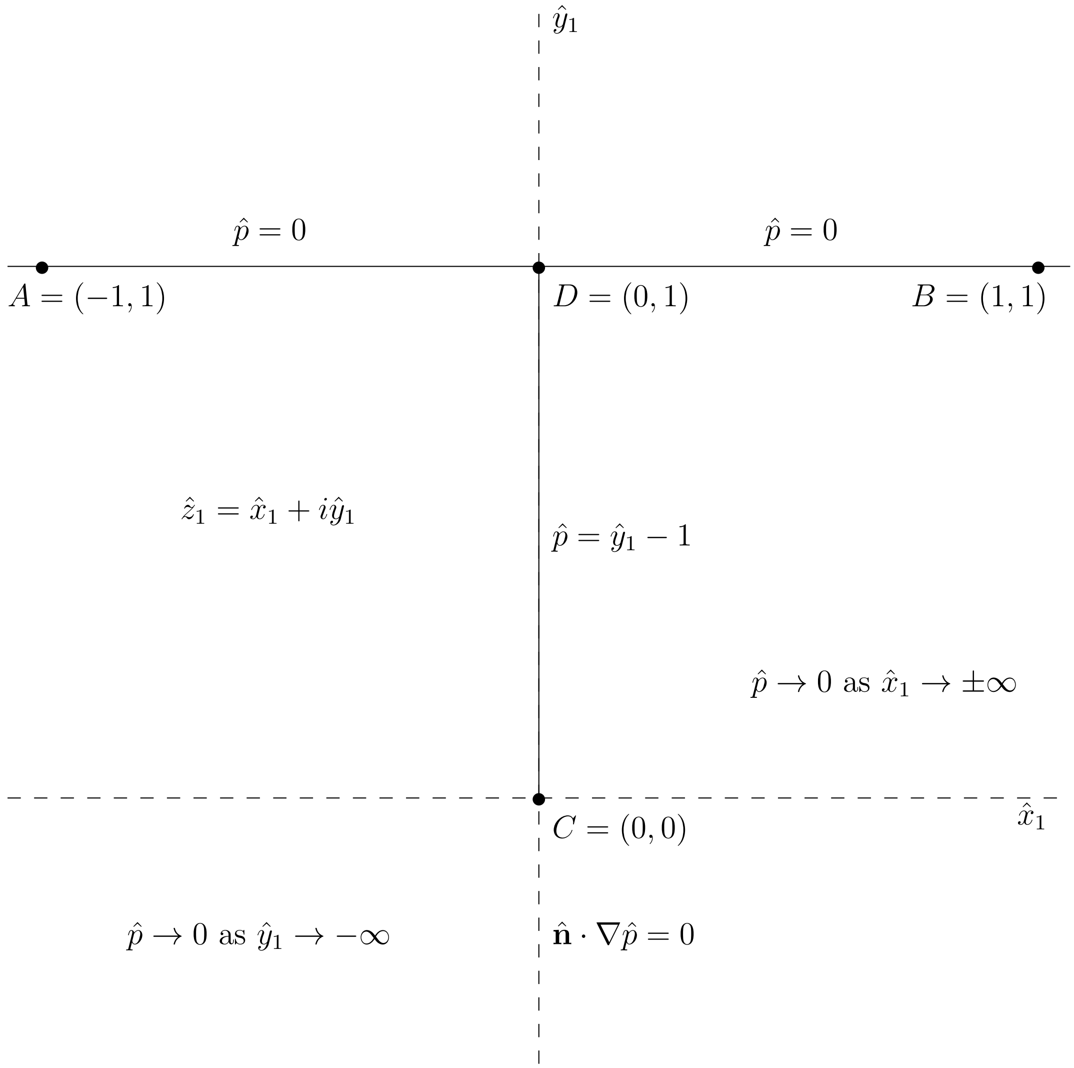

Figure 2.2: A model of an infinitesimally thin crack in a semi-infinite block of bitumen. The pressure along the crack is $\hat{p} = \hat{y}_1 - 1$ and the surface of the crack is given by the solid black line. Here the letters $A - D$ represent points along the surface of the crack.

By defining the domain of the bitumen to be $\hat{z}_1 = \hat{x}_1 + i\hat{y}_1$ in the complex plane, conformal mapping can be used to transform this problem into a version that is solvable. By using the co-ordinate transformation

$$\hat{z}_2 = \left(2i\hat{z}_1 - \hat{z}_1^2\right)^{\frac{1}{2}} \tag{2.24}$$

the model takes the form seen in Fig. 2.3. Here the new coordinate system is defined by the relationship $\hat{z}_2 = \hat{x}_2 + i\hat{y}_2$. The pressure on the crack in this new co-ordinate system is given by

$$\hat{p} = -\left(1 - \hat{y}_2^2\right)^{\frac{1}{2}}. \tag{2.25}$$

Here the negative square root is taken to remain consistent with the fact that $\hat{p} \leq 0$ throughout the system.

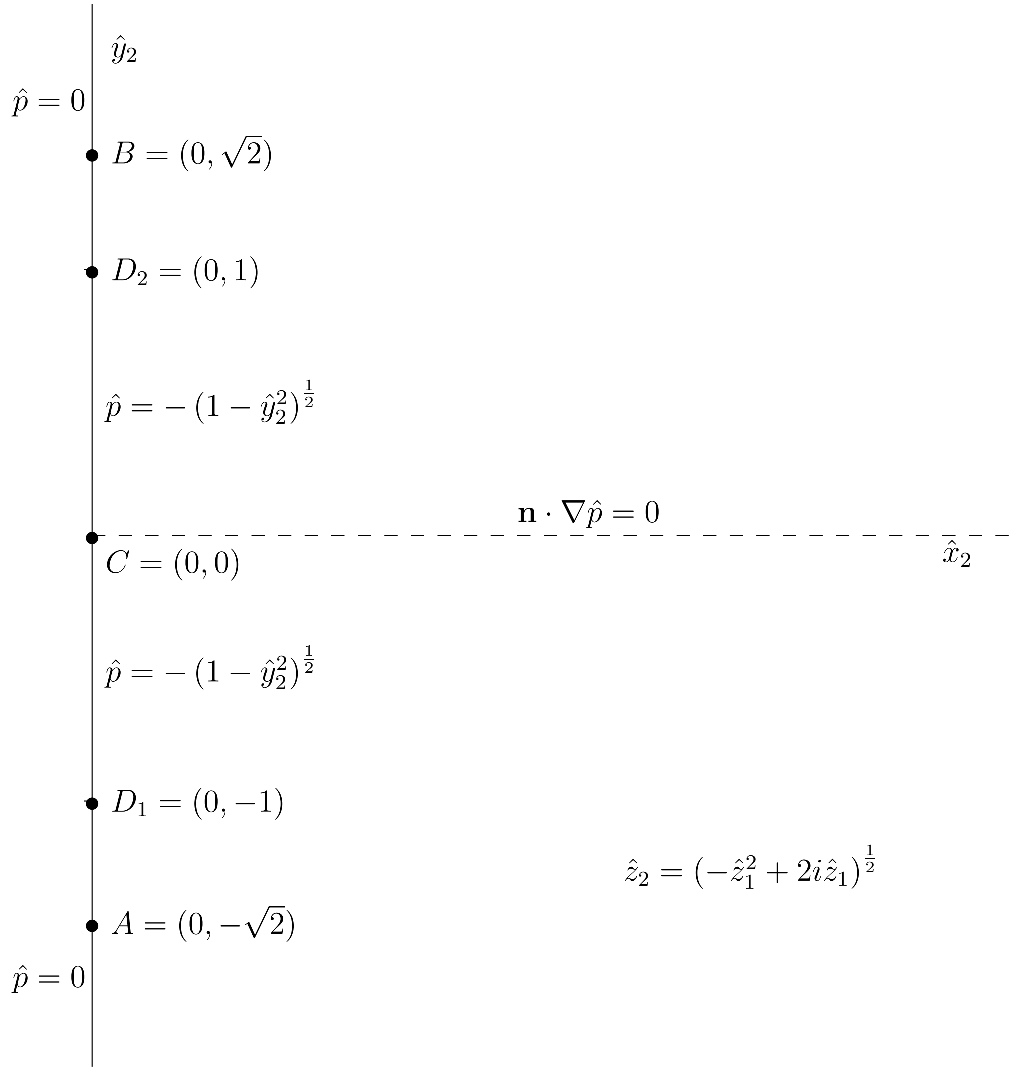

Figure 2.3: After all the transformations are completed the pressure acting on the crack becomes $\hat{p} = -\left(1 - \hat{y}_2^2\right)^{\frac{1}{2}}$. The solid black line represents the surface of the crack in the new co-ordinate system. Points $A - C$ correspond to the new locations of points $A - C$ in Fig. 2.2. Point D has been split into D_1 and D_2 to correspond to the two sides of the crack opening in the new co-ordinate system.

After this is done a variant of Poisson's formula for a half plane

$$\hat{p}(\hat{x}_2, \hat{y}_2) = \frac{\hat{x}_2}{\pi} \int_{-\infty}^{\infty} \frac{f_{\hat{p}}\left(s_1\right)}{\hat{x}_2^2 + \left(\hat{y}_2 - s_1\right)^2} ds_1 \tag{2.26}$$

can be used [King et al., 2003] to give the pressure at any point in the system. In this equation $f_{\hat{p}}\left(s_1\right)$ is the pressure on the crack in the final co-ordinate system. Here

s_1 has been used as a dummy variable in place of $\hat{y}_2$ to prevent confusion with spatial co-ordinates.

In this particular problem $f_{\hat{p}}\left(s_1\right) = -\left(1 - s_1^2\right)^{\frac{1}{2}}$ so

$$\hat{p}(\hat{x}_2, \hat{y}_2) = -\frac{\hat{x}_2}{\pi} \int_{-1}^{1} \frac{\left(1 - s_1^2\right)^{\frac{1}{2}}}{\hat{x}_2^2 + \left(\hat{y}_2 - s_1\right)^2} ds_1 \tag{2.27}$$

can be used. Here the limits of the integral have been changed to -1 and 1 as the pressure on the surface is zero for areas outside of the crack and so only the region the crack has been mapped to contributes in this case. The system is then mapped back to the original co-ordinates to give the pressure at any point in the original system. This can be done using the co-ordinate transforms

$$\hat{x}_2 = \left(\frac{1}{2}\left(\left(\hat{y}_1 - 1\right)^2 - \hat{x}_1^2 - 1 + \left(\left(\left(\hat{y}_1 - 1\right)^2 - \hat{x}_1^2 - 1\right)^2 + 4\hat{x}_1^2\left(\hat{y}_1 - 1\right)^2\right)^{\frac{1}{2}}\right)\right)^{\frac{1}{2}} \tag{2.28}$$

and

$$\hat{y}_2 = \frac{2\hat{x}_1 - 2\hat{x}_1\hat{y}_1}{\left(2\left(\left(\hat{y}_1 - 1\right)^2 - \hat{x}_1^2 - 1 + \left(\left(\left(\hat{y}_1 - 1\right)^2 - \hat{x}_1^2 - 1\right)^2 + 4\hat{x}_1^2\left(\hat{y}_1 - 1\right)^2\right)^{\frac{1}{2}}\right)\right)^{\frac{1}{2}}}. \tag{2.29}$$

When (2.27) is computed it gives the pressure profile in Fig. 2.4 where each line is a line of constant pressure. This in turn can be used to derive the small time asymptotic solution to the pressure gradient of the system, represented by the size and direction of the arrows in Fig. 2.4. This contour plot was created by computing the results of (2.27) for individual points in a 100×100 grid over the domain -1≤ $\hat{x}_1$ ≤1 and -1≤ $\hat{y}_1$ ≤1.

The contour plot shows that throughout the porous medium bitumen is consistently flowing towards the crack with flow being fastest near the tip of the crack. This would imply that bitumen will flow into the crack with the base of the crack filling the fastest.

The initially unintuitive aspect of the flow is that the bitumen under the lowest point of the crack is flowing upwards, against the direction of gravity. This can be explained by the fact that the bitumen at higher levels is weighing down on the bitumen at lower levels, increasing the pressure more the further below the surface you observe. These higher pressure levels act in opposition to gravity causing the bitumen under the crack to flow upwards towards the crack with the bitumen to the top and sides of the porous medium flowing in to take its place. As such this pushes the bitumen underneath the crack up, overcoming the opposing force due to gravity.

2.2.3 Approximation of the Pressure Near the Tip of the Crack

To get a better idea of how the system behaves near the tip of the crack at time $\hat{t} = 0$, when the effects of surface tension are negligible compared to those of gravity, the pressure, $\hat{p}$, in the immediate vicinity can be approximated to a polynomial. This is done by evaluating (2.27) assuming that the co-ordinates $\hat{x}_2, \hat{y}_2 \ll 1$.

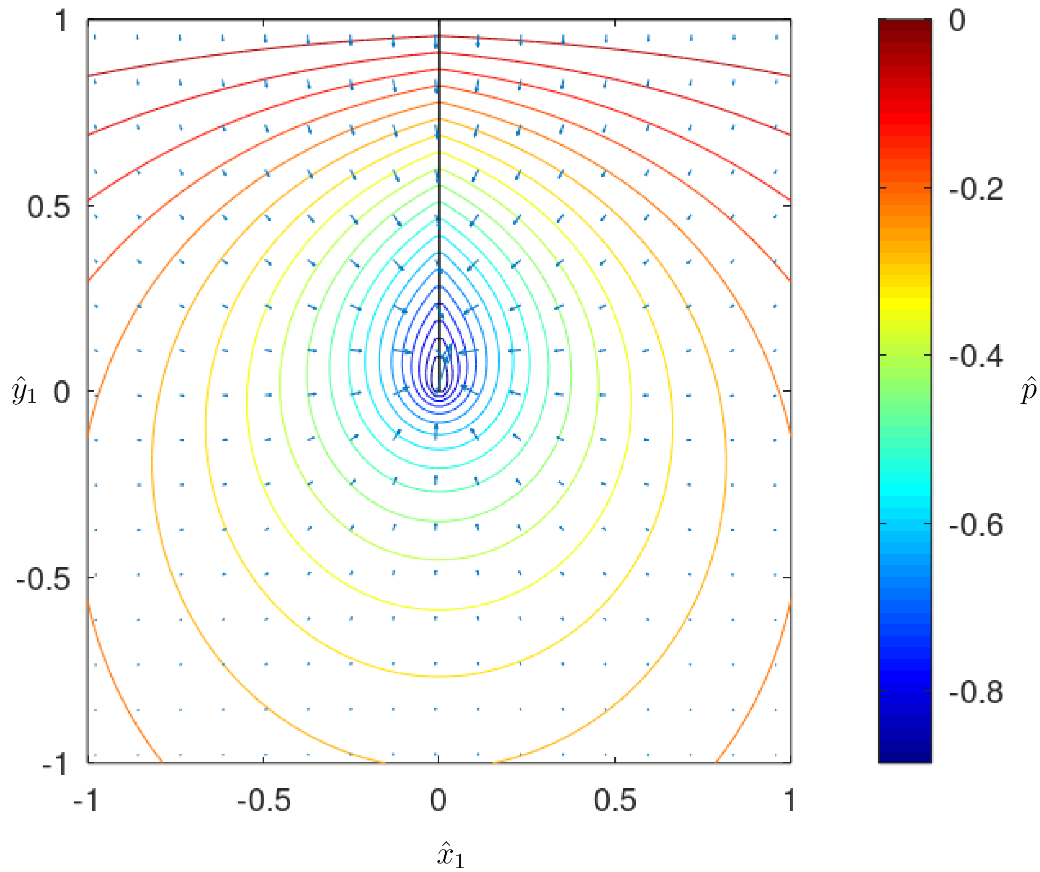

Figure 2.4: A contour plot of $\hat{p}$. Each line in the plot represents a section of constant pressure with blue lines representing low pressure and red lines representing high pressure, as described by the colour bar. The black line is the infinitesimally small crack. The arrows show the initial velocity of the fluid.

By making the substitutions $s_1 = \hat{y}_2 s_2$ and $k = \hat{x}_2/\hat{y}_2$ and splitting the integral into three different sections, the equation can be written

$$\frac{\pi\hat{p}}{k} = -\int_{\hat{y}_2^{-\frac{1}{2}}}^{\hat{y}_2^{-1}} \frac{\left(1-\hat{y}_2^2 s_2^2\right)^{\frac{1}{2}}}{k^2+\left(1-s_2\right)^2} ds_2 - \int_{-\hat{y}_2^{-\frac{1}{2}}}^{\hat{y}_2^{-\frac{1}{2}}} \frac{\left(1-\hat{y}_2^2 \bar{s}_2{}^2\right)^{\frac{1}{2}}}{k^2+\left(1-s_2\right)^2} ds_2 - \int_{-\hat{y}_2^{-1}}^{-\hat{y}_2^{-\frac{1}{2}}} \frac{\left(1-\hat{y}_2^2 s_2^2\right)^{\frac{1}{2}}}{k^2+\left(1-s_2\right)^2} ds_2. \tag{2.30}$$

This splitting of the integral allows the integrals to be calculated separately and then recombined later in the process. The first of these integrals

$$I_1 = \int_{\hat{y}_2^{-\frac{1}{2}}}^{\hat{y}_2^{-1}} \frac{\left(1-\hat{y}_2^2 s_2^2\right)^{\frac{1}{2}}}{k^2+\left(1-s_2\right)^2} ds_2 \tag{2.31}$$

can be approximated by setting $s_2 = \hat{y}_2^{-\frac{1}{2}} s_3$ to give

$$I_1 = \hat{y}_2^{\frac{1}{2}} \int_1^{\hat{y}_2^{-\frac{1}{2}}} \frac{(1-\hat{y}_2 s_3^2)^{\frac{1}{2}}}{s_3^2} \left(1 + \frac{(1+k^2)\,\hat{y}_2 - 2\hat{y}_2^{\frac{1}{2}} s_3}{s_3^2}\right)^{-1} ds_3. \tag{2.32}$$

By using $\hat{x}_2 \ll 1$ and $\hat{y}_2 \ll 1$ this can be approximated to

$$\begin{aligned} I_1 = \hat{y}_2^{\frac{1}{2}} \int_1^{\hat{y}_2^{-\frac{1}{2}}} \frac{(1-\hat{y}_2 s_3^2)^{\frac{1}{2}}}{s_3^2} \Bigg(1 - \left(\frac{(1+k^2)\,\hat{y}_2 - 2\hat{y}_2^{\frac{1}{2}} s_3}{s_3^2}\right) + \left(\frac{(1+k^2)\,\hat{y}_2 - 2\hat{y}_2^{\frac{1}{2}} s_3}{s_3^2}\right)^2 \\ - \left(\frac{(1+k^2)\,\hat{y}_2 - 2\hat{y}_2^{\frac{1}{2}} s_3}{s_3^2}\right)^3 + \left(\frac{(1+k^2)\,\hat{y}_2 - 2\hat{y}_2^{\frac{1}{2}} s_3}{s_3^2}\right)^4 + O\left(\hat{y}_2\right)^{\frac{5}{2}}\Bigg) ds_3 \end{aligned} \tag{2.33}$$

through the use of binomial expansion. In this step it is also assumed that $\hat{x}_2$ and $\hat{y}_2$ are of roughly the same magnitude, specifically that k or $\hat{x}_2/\hat{y}_2 \gg 1$ does not hold. When the same process is done with the third integral

$$I_3 = \int_{-\hat{y}_2^{-1}}^{-\hat{y}_2^{-\frac{1}{2}}} \frac{(1-\hat{y}_2^2 s_2^2)^{\frac{1}{2}}}{k^2 + (1-s_2)^2} ds_2 \tag{2.34}$$

and both integrals are evaluated it can be shown that

$$\begin{aligned} I_1 + I_3 = 2\left(\hat{y}_2^{\frac{1}{2}} + \left(1 - \frac{1}{3}k^2\right)\hat{y}_2^{\frac{3}{2}} + \left(\frac{1}{5}k^2 - \frac{5}{3}k^2\right)\hat{y}_2^{\frac{5}{2}}\right)(1-\hat{y}_2)^{\frac{1}{2}} \\ -\pi\hat{y}_2 + 2\hat{y}_2 \arcsin\left(\hat{y}_2^{\frac{1}{2}}\right) + O\left(\hat{y}_2^3\right). \end{aligned} \tag{2.35}$$

Upon Taylor expanding the $\arcsin\left(\hat{y}_2^{\frac{1}{2}}\right)$ term about $\hat{y}_2 = 0$ this simplifies to

$$I_1 + I_3 = 2\hat{y}_2^{\frac{1}{2}} - \pi\hat{y}_2 + \left(3 - \frac{2}{3}k^2\right)\hat{y}_2^{\frac{3}{2}} + \left(-\frac{11}{12} - 3k^2 + \frac{2}{5}k^4\right)\hat{y}_2^{\frac{5}{2}} + O\left(\hat{y}_2^3\right). \tag{2.36}$$

The second integral is

$$I_2 = \int_{-\hat{y}_2^{-\frac{1}{2}}}^{\hat{y}_2^{-\frac{1}{2}}} \frac{(1-\hat{y}_2^2 s_2^2)^{\frac{1}{2}}}{k^2 + (1-s_2)^2} ds_2. \tag{2.37}$$

By substituting s_2 for $1 - k\tan s_4$ this can be rewritten as

$$I_2 = -\frac{1}{k} \int_{-\arctan\frac{1-\hat{y}_2^{-\frac{1}{2}}}{k}}^{\arctan\frac{1-\hat{y}_2^{-\frac{1}{2}}}{k}} \left(1 - \frac{1}{2}\hat{y}_2^2\,(1-k\tan s_4)^2 - \frac{1}{8}\hat{y}_2^4\,(1-k\tan s_4)^4 + O\left(\hat{y}_2^6\right)\right) ds_4. \tag{2.38}$$

After solving the integral and then Taylor expanding about $\hat{y}_2 = 0$ this gives

$$I_2 = \frac{\pi}{k} - 2\hat{y}_2^{\frac{1}{2}} + \left(-3 + \frac{2}{3}k^2\right)\hat{y}_2^{\frac{3}{2}} + \left(\frac{11}{12} + 3k^2 - \frac{2}{5}k^4\right)\hat{y}_2^{\frac{5}{2}} + \left(-\frac{1}{k} + k\right)\frac{\pi}{2}\hat{y}_2^2 + O\left(\hat{y}_2^3\right). \tag{2.39}$$

Now that the three integrals have been solved individually they can be added together and simplified to give the result

$$\hat{p} = -1 + k\hat{y}_2 + \left(1 - k^2\right)\frac{\hat{y}_2^2}{2} + O\left(\hat{y}_2^3\right). \tag{2.40}$$

Next reversing the earlier substitution $k = \hat{x}_2/\hat{y}_2$ allows this to be written in terms of $\hat{x}_2$ and $\hat{y}_2$ as

$$\hat{p} = -1 + \hat{x}_2 + \frac{\hat{y}_2^2}{2} - \frac{\hat{x}_2^2}{2} + O\left(\hat{y}_2^3\right) + O\left(\hat{x}_2^3\right). \tag{2.41}$$

This now needs to be transformed into the original co-ordinate system prior to when conformal mapping took place. This can be done using $\hat{z}_2 = \hat{x}_2 + i\hat{y}_2$ to give

$$\hat{p} = \mathrm{Re}\left(-1 + \hat{z}_2 - \frac{1}{2}\hat{z}_2^2\right) + O\left(\left|\hat{z}_2^3\right|\right). \tag{2.42}$$

The original co-ordinate transform (2.24) used in conformal mapping can then be used to change the co-ordinates to their original system, given by $\hat{z}_1 = \hat{x}_1 + i\hat{y}_1$. This gives

$$\hat{p} = \mathrm{Re}\left(-1 + \sqrt{2i\hat{z}_1 - \hat{z}_1^2} - i\hat{z}_1 + \frac{1}{2}\hat{z}_1^2\right) + O\left(\left|\hat{z}_1^3\right|\right). \tag{2.43}$$

By re-arranging this into the form

$$\hat{p} = -1 + \hat{y}_1 + \frac{1}{2}\left(\hat{x}_1^2 - \hat{y}_1^2\right) + \mathrm{Re}\left(\sqrt{1 + \frac{1}{2}i\hat{z}_1}\sqrt{2i\hat{z}_1}\right) + O\left(\left|\hat{z}_1^3\right|\right) \tag{2.44}$$

the equation can now be approximated by binomial expansion to give

$$\hat{p} = -1 + \hat{y}_1 + \frac{1}{2}\left(\hat{x}_1^2 - \hat{y}_1^2\right) + \mathrm{Re}\left(\left(1 + \frac{1}{4}i\hat{z}_1 + \frac{1}{32}\hat{z}_1^2\right)\sqrt{2i\hat{z}_1}\right) + O\left(\left|\hat{z}_1^3\right|\right). \tag{2.45}$$

Rather than express the real part of this equation in terms of $\hat{x}_1$ and $\hat{y}_1$ it is simpler to convert the equation to polar co-ordinates where $r_1 = \sqrt{\hat{x}_1^2 + \hat{y}_1^2}$ and $\theta_1 = \tan^{-1}\frac{\hat{y}_1}{\hat{x}_1}$. When expressed in polar co-ordinates this equation becomes

$$\begin{aligned}\hat{p} = -1 + r_1^{\frac{1}{2}}\left(\cos\left(\frac{1}{2}\theta_1\right) - \sin\left(\frac{1}{2}\theta_1\right)\right) + r_1\sin\theta_1 - \frac{1}{4}r_1^{\frac{3}{2}}\left(\cos\left(\frac{3}{2}\theta_1\right) + \sin\left(\frac{3}{2}\theta_1\right)\right)\\ + r_1^2\left(\frac{1}{2} - \sin^2\theta_1\right) + \frac{1}{32}r_1^{\frac{5}{2}}\left(\cos\left(\frac{5}{2}\theta_1\right) - \sin\left(\frac{5}{2}\theta_1\right)\right) + O\left(r_1^3\right).\end{aligned} \tag{2.46}$$

This can then be used to find the pressure gradient which by using the association (2.12) can be used to compute the small time asymptotic velocity of the fluid

$$-\nabla \hat{p} = \left[\frac{r_1^{-\frac{1}{2}}}{2} \left(\sin\left(\frac{1}{2}\theta_1\right) - \cos\left(\frac{1}{2}\theta_1\right) \right) - \sin\theta_1 + \frac{3}{8} r_1^{\frac{1}{2}} \left(\sin\left(\frac{3}{2}\theta_1\right) + \cos\left(\frac{3}{2}\theta_1\right) \right) \right.$$
$$\left. + r_1 \left(-1 + 2\sin^2\theta_1\right) + \frac{5}{64} r_1^{\frac{3}{2}} \left(\sin\left(\frac{5}{2}\theta_1\right) - \cos\left(\frac{5}{2}\theta_1\right) \right) \right] \hat{\mathbf{r}}$$
$$+ \left[\frac{r_1^{\frac{1}{2}}}{2} \left(\sin\left(\frac{1}{2}\theta_1\right) + \cos\left(\frac{1}{2}\theta_1\right) \right) - r_1 \cos\theta_1 + \frac{3}{8} r_1^{\frac{3}{2}} \left(-\sin\left(\frac{3}{2}\theta_1\right) + \cos\left(\frac{3}{2}\theta_1\right) \right) \right] \hat{\mathbf{n}}$$
$$+ O\left(r_1^2\right). \tag{2.47}$$

The resulting pressure contour plot for these approximations is given in Fig. 2.5 below. This graph was created by using (2.46) to calculate the pressure at each point in a 100×100 grid over the domain -0.1≤ $\hat{x}_1$ ≤0.1 and -0.1≤ $\hat{y}_1$ ≤0.1.

In this graph the contours represent lines of constant pressure, while the arrows represent the initial velocity of the bitumen, with larger arrows representing faster movement. The black line gives the location of the tip of the crack.

From this graph it is apparent that the highest pressure gradient in the system occurs immediately under the tip of the crack, with the pressure gradient decreasing with the distance away from the tip. This in turn leads to an increased initial velocity of the fluid nearer to the tip of the crack. Here the movement of the fluid is towards the crack throughout the domain which complies with the expectation that fluid will flow into the crack.

As discussed in the previous section there is a movement of fluid upwards against the flow of gravity in the lower section of the domain. This can be explained by the higher pressure at lower parts of the system acting against gravity to push the fluid upwards towards the crack.

The results of this approximation can be compared directly to the results from the previous section. Fig. 2.6 was created by directly computing (2.12) over individual points in a 100×100 grid over the same domain used in Fig. 2.5. These two graphs show a clear agreement which implies that in regions close enough to the tip of the crack the approximation is valid when the effects of gravity are dominant over those of surface tension.

2.2.4 Conformal Mapping of an Idealised Crack

Conformal mapping can also be used to find the pressure of a crack of angle 2α for time $\hat{t} \ll 1$. The system is shown in Fig. 2.7. This can be done by considering the Schwarz-Christoffel mapping from a lower half plane to a crack of angle 2α.

The function which transforms a lower half plane defined by $\hat{z}_2 = \hat{x}_2 + i\hat{y}_2$ into the form of a crack of angle 2α described by $\hat{z}_1 = \hat{x}_1 + i\hat{y}_1$ is given by [Spiegel, 1972]

$$f\left(\hat{z}_2\right) = B + A \int \left(\hat{z}_2 - \hat{x}_a\right)^{-\frac{\beta_a}{\pi}} \left(\hat{z}_2 - \hat{x}_b\right)^{-\frac{\beta_b}{\pi}} \left(\hat{z}_2 - \hat{x}_c\right)^{-\frac{\beta_c}{\pi}} d\hat{z}_2. \tag{2.48}$$

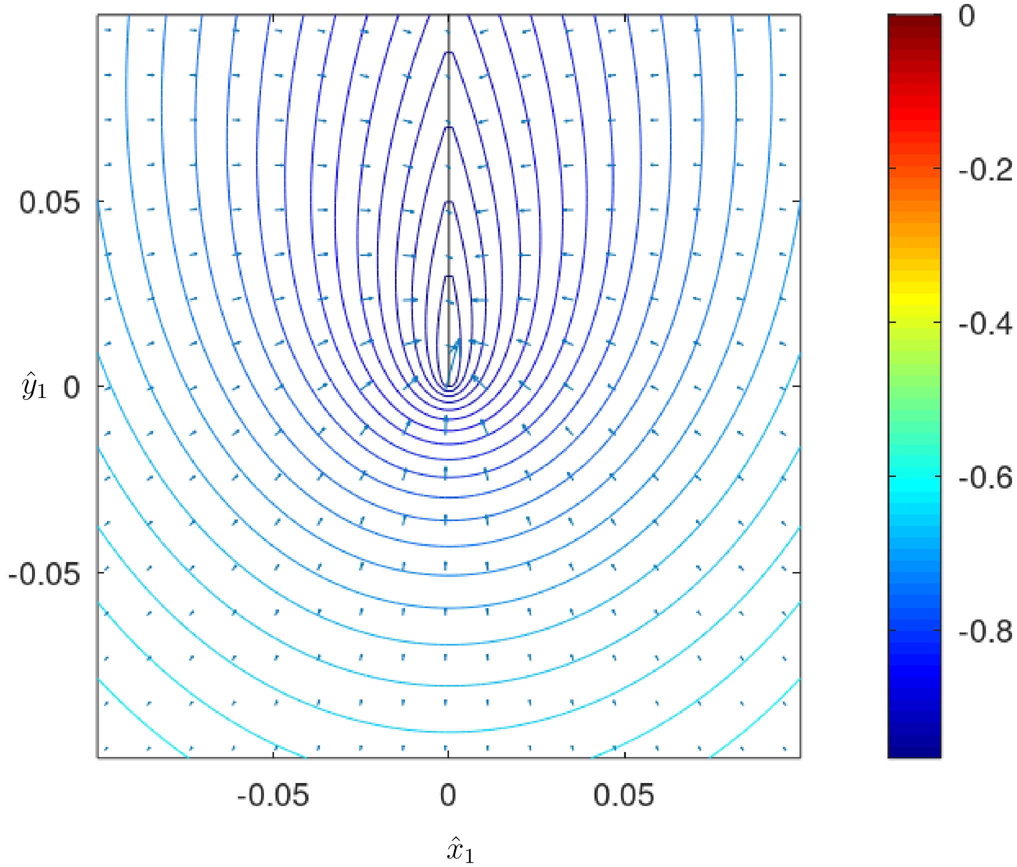

Figure 2.5: A contour plot of the approximate value of $\hat{p}$ near the tip of the crack under the approximations listed in this section. Each line in the plot represents a section of constant pressure. Here the colour bar gives the value of $\hat{p}$ associated with contours of that colour. The black line is the infinitesimally thin crack. The arrows show the initial velocity of the fluid.

Here A and B are constants, β_a, β_b and β_c are the external angles of the crack and $\hat{x}_a$, $\hat{x}_b$ and $\hat{x}_c$ are positions of arbitrary points on the surface of the lower half plane. A and B are constants which determine the shape and position of the surface in the new co-ordinate system.

Taking $\hat{x}_a$, $\hat{x}_b$ and $\hat{x}_c$ to be 1, 0 and -1 respectively this can be simplified to

$$f\left(\hat{z}_2\right) = B + A\int\left(\frac{\hat{z}_2^2}{\hat{z}_2^2 - 1}\right)^{\frac{1}{2}-\frac{\alpha}{\pi}} d\hat{z}_2. \tag{2.49}$$

For a known value of α a variant of Poisson's formula for a half plane [King et al., 2003]

$$\hat{p}(\hat{x}_2, \hat{y}_2) = -\frac{\hat{y}_2}{\pi}\int_{-\infty}^{\infty}\frac{f_{\hat{p}}\left(s_1\right)}{\hat{y}_2^2 + \left(\hat{x}_2 - s_1\right)^2} ds_1 \tag{2.50}$$

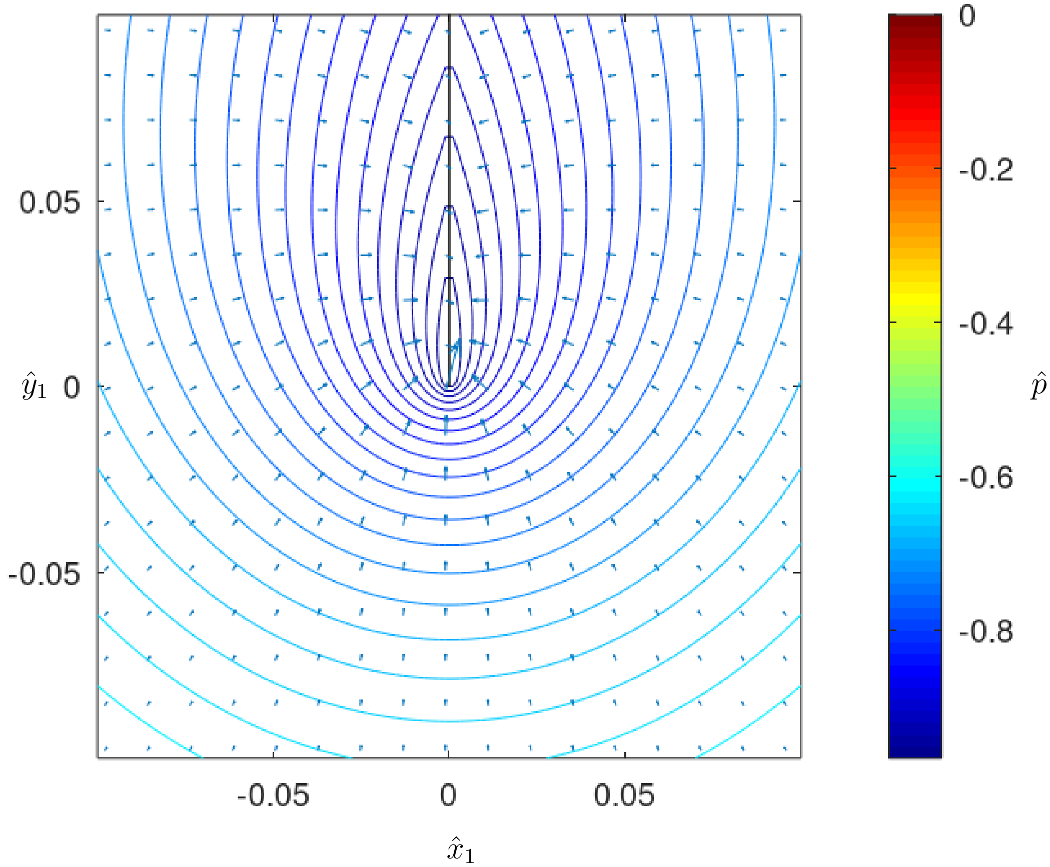

Figure 2.6: A contour plot of the values of $\hat{p}$. Each line in the plot represents a section of constant pressure. Here the colour bar gives the value of $\hat{p}$ associated with contours of that colour. The black line is the infinitesimally thin crack. The arrows show the initial velocity of the fluid.

can be computed to give the pressure of the entire system. Here $f_{\hat{p}}(s_1)$ is the pressure on the crack in the final co-ordinate system with s_1 acting as a dummy variable in place of $\hat{x}_2$. The values of $\hat{x}_2$ and $\hat{y}_2$ can be found by computing the real and imaginary parts of $f^{-1}(\hat{x}_1 + i\hat{y}_1)$ respectively at each point being examined. This in turn can be used to derive the pressure gradient and initial flow of the bitumen at time $\hat{t} = 0$. The form of this equation differs slightly from (2.26) as here the lower half plane is being integrated over as opposed to the right half plane.

The form of the solution to (2.49) varies greatly with the value of α. As such this is as far as we can take the general case. As an example of a specific case, when $\alpha = \pi/10$ (2.49) reduces to

$$f(\hat{z}_2) = B + A \int \left(\frac{\hat{z}_2^2}{\hat{z}_2^2 - 1} \right)^{\frac{2}{5}} d\hat{z}_2. \tag{2.51}$$

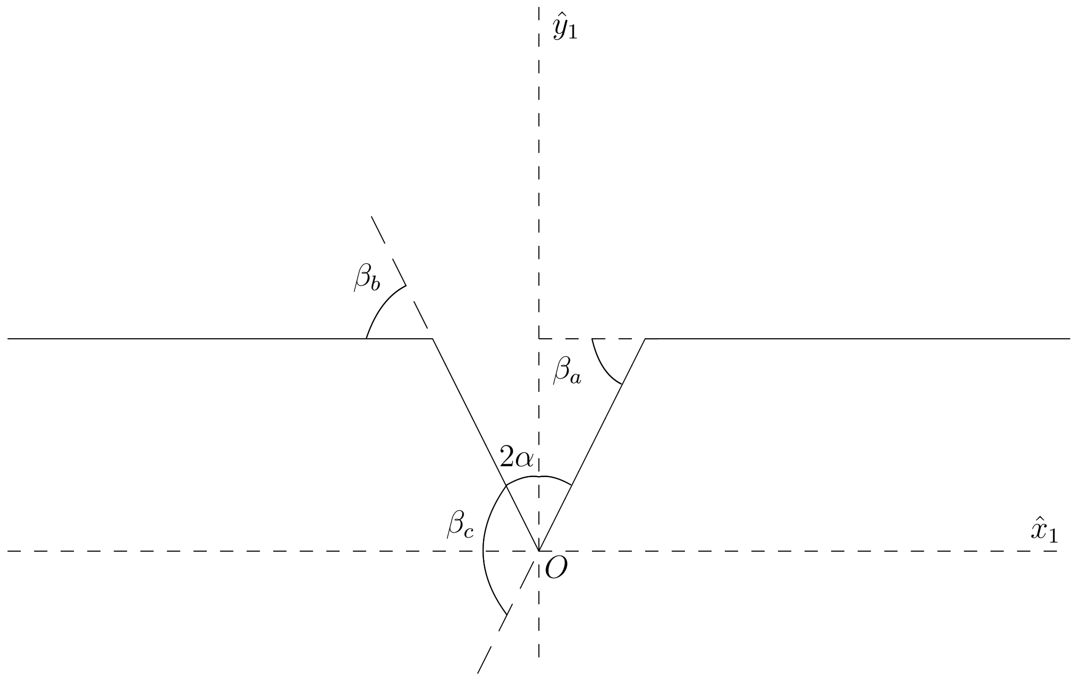

Figure 2.7: A crack of angle 2α and external angles of β_1, β_2 and β_3.

Solving this integral can be shown to yield the solution

$$f(\hat{z}_2) = B + \frac{5A}{9}\hat{z}_2^{\frac{7}{5}}(-\hat{z}_2)^{\frac{2}{5}}\,{}_2F_1\left(\frac{2}{5}, \frac{9}{10}; \frac{19}{10}; \hat{z}_2^2\right), \tag{2.52}$$

where ${}_2F_1(a, b; c; \hat{z}_2)$ is the hypergeometric function given by [Nørlund, 1955]

$${}_2F_1(a, b; c; \hat{z}_2) = \sum_{n=0}^{\infty} \frac{(a)_n (b)_n}{(c)_n} \frac{\hat{z}_2^n}{n!}. \tag{2.53}$$

Here a, b and c are arbitrary constants while $(a)_n$ is the rising Pochhammer symbol which can be expressed as [Sarikaya et al., 2020]

$$(a)_n = \begin{cases} 1, & \text{if } n = 0 \\ \prod_{k=1}^{n}(a + k - 1), & \text{if } n > 0. \end{cases} \tag{2.54}$$

To calculate A and B we can look at the location of two points before and after being subject to the mapping. To do this we can substitute $\hat{z}_2$ for 1 and 0 and evaluate their positions in the new co-ordinate system. For the tip of the crack to be mapped to the origin

$$f(0) = 0 \tag{2.55}$$

must be true and for the height of the crack to be one means that $f\left(1\right)$ must map to the corner of the crack so

$$f\left(1\right)=\tan\left(\frac{\pi}{10}\right)+i \tag{2.56}$$

must hold.

When $\hat{z}_2=0$

$$f\left(0\right)=B, \tag{2.57}$$

while when $\hat{z}_2=1$

$$f\left(1\right)=B+A\frac{10\Gamma\left(\frac{3}{5}\right)\Gamma\left(\frac{19}{10}\right)}{9\sqrt{\pi}}\left(\cos\left(\frac{2\pi}{5}\right)+i\sin\left(\frac{2\pi}{5}\right)\right). \tag{2.58}$$

Here for a constant a, $\Gamma\left(a\right)$ is the Euler gamma function defined by [Sarikaya et al., 2020]

$$\Gamma\left(a\right)=\int_0^\infty s^{a-1}e^{-s}ds, \tag{2.59}$$

where s is a dummy variable to be integrated over. Using the result in (2.57) combined with (2.55) we see that

$$B=0 \tag{2.60}$$

and taking that result with (2.58) and (2.56) yields

$$A=\frac{9\sqrt{\pi}}{10\sin\left(\frac{2\pi}{5}\right)\Gamma\left(\frac{3}{5}\right)\Gamma\left(\frac{19}{10}\right)}. \tag{2.61}$$

Substituting the values of A and B into (2.52) gives the result

$$f\left(\hat{z}_2\right)=\frac{\sqrt{\pi}}{2\sin\left(\frac{2\pi}{5}\right)\Gamma\left(\frac{3}{5}\right)\Gamma\left(\frac{19}{10}\right)}\hat{z}_2^{\frac{7}{5}}\left(-\hat{z}_2\right)^{\frac{2}{5}}{}_2F_1\left(\frac{2}{5},\frac{9}{10};\frac{19}{10};\hat{z}_2^2\right) \tag{2.62}$$

when $\alpha=\frac{\pi}{10}$.

This now provides enough information to compute the pressure at any point in the domain of the bitumen. A contour plot of the pressure can be seen in Fig. 2.8. To reduce the computational complexity, rather than computing the values of $f\left(\hat{x}_1+i\hat{y}_1\right)$ for an array of pre-defined points in the $\hat{z}_1$ plane as has been done in previous sections a 100×100 array of points in the $\hat{z}_2$ plane was selected over a domain of $-2\leq\hat{x}_2\leq 2$ and $-2\leq\hat{y}_2\leq 0$. The pressure on each point was calculated using (2.50) then the associated values of $\hat{x}_1$ and $\hat{y}_1$ were found using the real and imaginary components of (2.62) respectively. The value of $f_{\hat{p}}\left(s_1\right)$ in (2.50) was taken to be $f\left(\hat{y}_1\right)-1$ with values of $\hat{x}_2$ substituted for the dummy variable s_1 to integrate over.

This pressure field shares some similarities with the ones produced for the case of an infinitesimally thin crack but also some interesting differences. As would be expected the pressure shows the same behaviour as previous cases further away from the crack with larger gaps between contours signalling a smaller pressure gradient further from the origin and with $\hat{p}$ tending to 0 as the distance from the origin grows. One of the main differences between this scenario and the infinitesimally thin crack is the behaviour of the pressure near to the crack. Here we see very tight contours in the immediate vicinity of the crack which signals a larger pressure gradient and so more fluid flow in this vicinity.

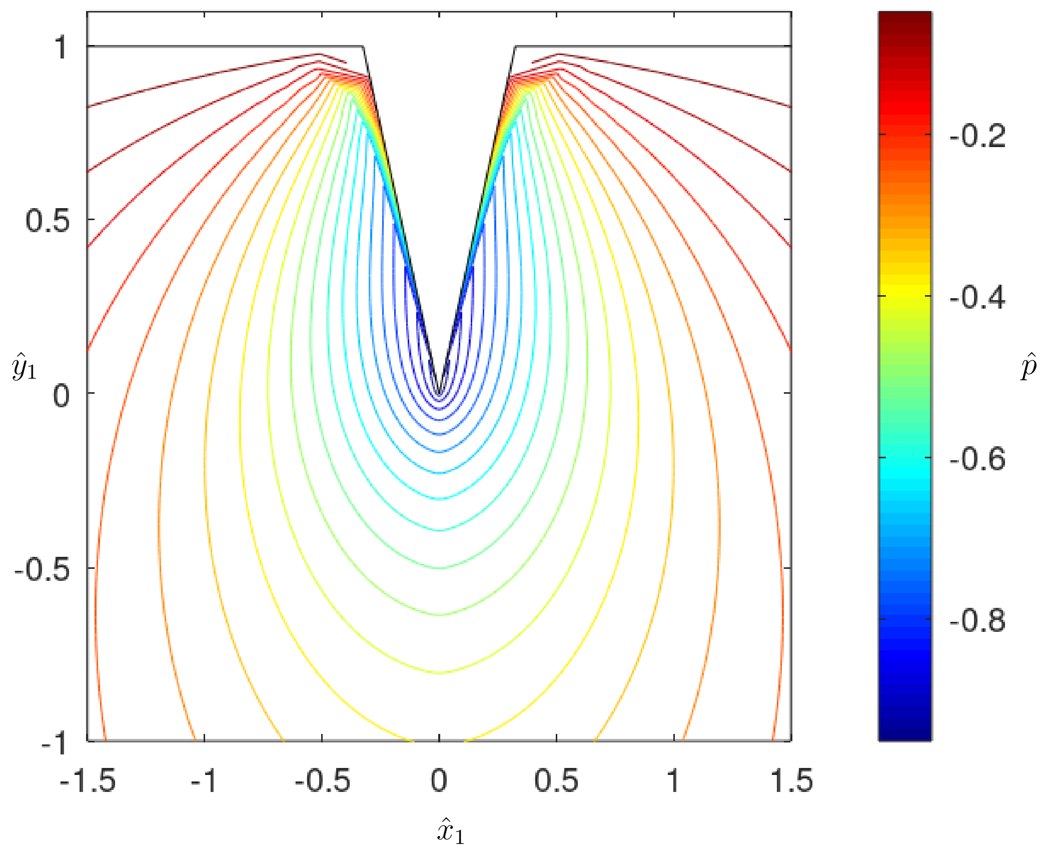

Figure 2.8: A contour plot of the approximate value of $\hat{p}$ for an idealised crack of angle $\alpha = \frac{\pi}{10}$. Each line in the plot represents a section of constant pressure. Here the colour bar gives the value of $\hat{p}$ associated with contours of that colour. The black line represents the initial surface of the crack.

2.2.5 Approximation of Pressure for a Generic Crack

Considering a generic crack at time $\hat{t} \ll 0$ with sides defined by $\hat{x} = \epsilon X_+(\hat{y})$ and $\hat{x} = \epsilon X_-(\hat{y})$ where ϵ is a dummy variable satisfying $\epsilon \ll 1$ and $\hat{x}$ and $\hat{y}$ are the Cartesian co-ordinates. Let the pressure be expressed by

$$\hat{p} = \hat{p}_0\left(\hat{x}, \hat{y}\right) + \epsilon \hat{p}_1\left(\hat{x}, \hat{y}\right) + O\left(\epsilon^2\right), \tag{2.63}$$

where $\hat{p}_0\left(\hat{x}, \hat{y}\right)$ is the leading order approximation to $\hat{p}$ and is given by (2.27). $\hat{p}_1\left(\hat{x}, \hat{y}\right)$ is the next largest order term in the perturbation series and $O\left(\epsilon^2\right)$ represents terms of order ϵ^2 or smaller. Next let

$$\hat{p} = \hat{p}_0\left(\hat{x}, \hat{y}\right) + \hat{p}_L\left(\hat{x}, \hat{y}\right), \tag{2.64}$$

where $\hat{p}_L\left(\hat{x}, \hat{y}\right)$ is the sum of the perturbation series with the leading order approximation excluded.

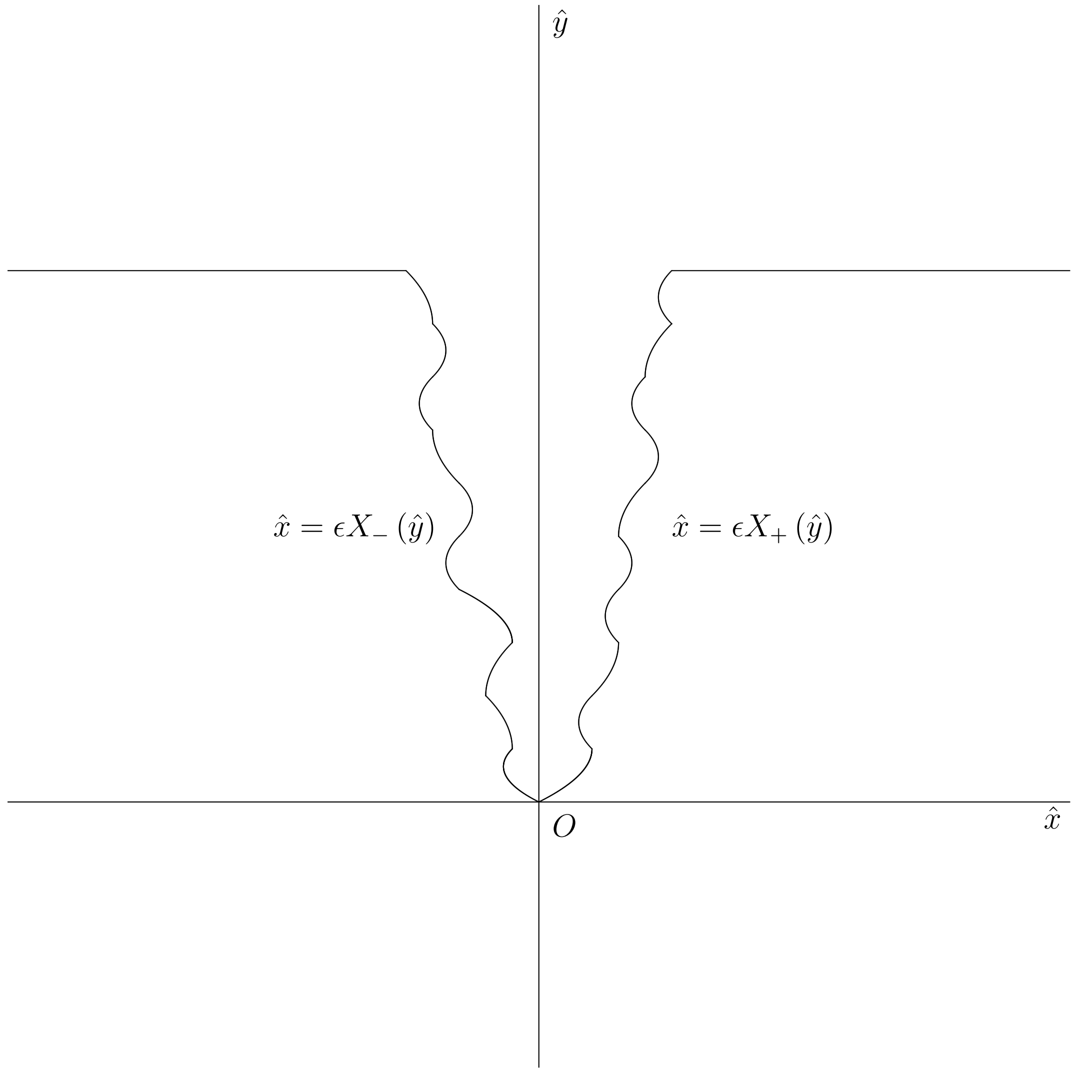

Figure 2.9: A generic non-symmetric crack in a sheet of bitumen where the width of the crack is much smaller than its length.

Hence on the crack

$$\hat{p}_L\left(\epsilon X_{+}\left(\hat{y}\right),\hat{y}\right) = \hat{y} - 1 - \frac{2\hat{\kappa}\left(\epsilon X_{+}\left(\hat{y}\right),\hat{y}\right)}{Bo} - \hat{p}_0\left(\epsilon X_{+}\left(\hat{y}\right),\hat{y}\right), \tag{2.65}$$

where $\hat{\kappa}\left(\epsilon X_{+}\left(\hat{y}\right),\hat{y}\right)$ is the curvature of a point on the crack and Bo is the Bond number. A visual representation of this can be seen in Fig. 2.9. However

$$\hat{p}_0\left(\epsilon X_{+}\left(\hat{y}\right),\hat{y}\right) = \hat{p}_0\left(0,\hat{y}\right) + \epsilon X_{+}\left(\hat{y}\right)\frac{\partial \hat{p}_0}{\partial \hat{x}}\left(0,\hat{y}\right) + O\left(\epsilon^2\right) \tag{2.66}$$

and

$$\hat{\kappa}\left(\epsilon X_{+}\left(\hat{y}\right),\hat{y}\right) = \hat{\kappa}\left(0,\hat{y}\right) + \epsilon X_{+}\left(\hat{y}\right)\frac{\partial \hat{\hat{\kappa}}}{\partial \hat{x}}\left(0,\hat{y}\right) + O\left(\epsilon^2\right), \tag{2.67}$$

the first term of which is equal to 0 along a flat crack. Hence

$$\hat{p}_L = -\frac{2\epsilon}{Bo}X_+(\hat{y})\frac{\partial\hat{\kappa}}{\partial\hat{x}}(0,\hat{y}) - \epsilon X_+(\hat{y})\frac{\partial\hat{p}_0}{\partial\hat{x}}(0,\hat{y}) + O\left(\epsilon^2\right). \tag{2.68}$$

This means that at $O(\epsilon)$ the system simplifies to the form shown in Fig. 2.10. and that the final pressure in the system is given by

$$\hat{p} = \hat{p}_0(\hat{x},\hat{y}) - \frac{2\epsilon}{Bo}X_+(\hat{y})\frac{\partial\hat{\kappa}}{\partial\hat{x}}(0,\hat{y}) - \epsilon X_+(\hat{y})\frac{\partial\hat{p}_0}{\partial\hat{x}}(0,\hat{y}) + O\left(\epsilon^2\right). \tag{2.69}$$

This means that an approximation to the pressure in the system can entirely be derived from the the pressure profile of a simple infinitesimally small crack adjusted for surface tension effects. Once this has been done the pressure can then be used for a crack of any given dimension to compute the small time asymptotic solution to the initial velocity of the interface.

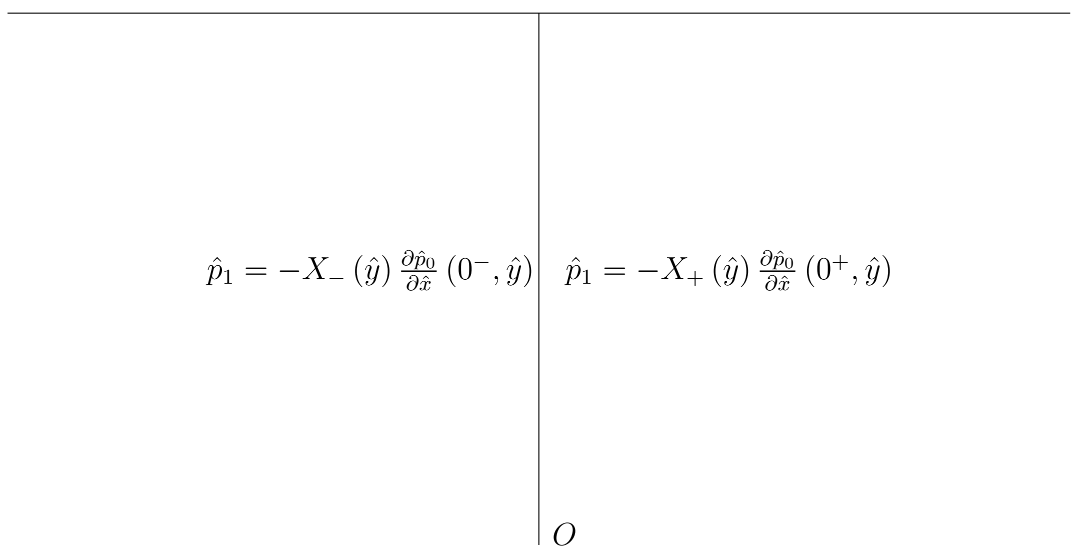

Figure 2.10: The $O(\epsilon)$ contribution to a generic crack in bitumen.

2.2.6 Numerical Solution

Boundary integral methods can be used to compute the pressure gradient at the surface of the crack numerically. This in turn can be used to predict the movement of the surface of the bitumen as it flows into a crack.

To begin we take Green's second identity, for ϕ_1 and ϕ_2, any two twice differentiable fields [Fernández-Guasti et al., 2012]

$$\nabla\cdot(\phi_1\nabla\phi_2 - \phi_2\nabla\phi_1) = \phi_1\nabla^2\phi_2 - \phi_2\nabla^2\phi_1. \tag{2.70}$$

Integrating this relationship over an area A_c assumed to be connected and bounded by a closed contour or collection of closed contours, C, gives

$$\int\int_{A_c}\nabla\cdot(\phi_1\nabla\phi_2 - \phi_2\nabla\phi_1)\,dA_c = \int\int_{A_c}\phi_1\nabla^2\phi_2 - \phi_2\nabla^2\phi_1 dA_c. \tag{2.71}$$

Here the assumptions made about A_c will be addressed in more detail on a domain by domain basis in the next section. By the divergence theorem [Stolze, 1978]

$$\int\int_{A_c} \nabla \cdot (\phi_1 \nabla \phi_2 - \phi_2 \nabla \phi_1)\, dA_c = \int_C \hat{\mathbf{n}} \cdot (\phi_1 \nabla \phi_2 - \phi_2 \nabla \phi_1)\, dC. \tag{2.72}$$

Here $\hat{\mathbf{n}}$ is the unit normal vector to the boundary C pointing out of the area A_c. This can be simplified by letting

$$\phi_1 = \hat{p} \tag{2.73}$$

then applying conservation of mass, $\nabla^2 \hat{p} = 0$ to (2.71) and (2.72). This gives the result

$$\int\int_{A_c} \hat{p} \nabla^2 \phi_2 dA_c = \int_C \hat{p}\, \hat{\mathbf{n}} \cdot \nabla \phi_2 - \phi_2 \hat{\mathbf{n}} \cdot \nabla \hat{p}\, dC. \tag{2.74}$$

Here we can simplify the situation by using a Green's function, a function which satisfies the singularity forced Laplace's equation [Pozrikidis, 2002]

$$\nabla^2 G(\hat{\mathbf{x}}, \hat{\mathbf{x}}_0) - \delta_2 (\hat{\mathbf{x}} - \hat{\mathbf{x}}_0) = 0, \tag{2.75}$$

where $G(\hat{\mathbf{x}}, \hat{\mathbf{x}}_0)$ is the Green's function, $\hat{\mathbf{x}}$ is a varying field point, $\hat{\mathbf{x}}_0$ is a constant singular point and $\delta_2 (\hat{\mathbf{x}} - \hat{\mathbf{x}}_0)$ is the two dimensional Dirac delta function. This can be used to simplify the left hand side of (2.74) by making the substitution

$$\phi_2 = G(\hat{\mathbf{x}}, \hat{\mathbf{x}}_0), \tag{2.76}$$

which results in the equation

$$\hat{p} \int\int_{A_c} \nabla^2 G(\hat{\mathbf{x}}, \hat{\mathbf{x}}_0)\, dA_c = \int_C \hat{p}\, \hat{\mathbf{n}} \cdot \nabla G(\hat{\mathbf{x}}, \hat{\mathbf{x}}_0) - G(\hat{\mathbf{x}}, \hat{\mathbf{x}}_0)\, \hat{\mathbf{n}} \cdot \nabla \hat{p}\, dC. \tag{2.77}$$

This means that by using the definition of the Green's function and the Dirac delta function and looking at the situations where $\hat{\mathbf{x}}_0$ is either inside, outside or on the boundary we have the result

$$\int\int_{A_c} \nabla^2 G(\hat{\mathbf{x}}, \hat{\mathbf{x}}_0)\, dA_c = \begin{cases} 1, & \text{if } \hat{\mathbf{x}}_0 \in A_c \\ 0, & \text{if } \hat{\mathbf{x}}_0 \notin A_c \\ \frac{1}{2}, & \text{if } \hat{\mathbf{x}}_0 \in C. \end{cases} \tag{2.78}$$

Using these results in conjunction with (2.77) we see that when the point $\hat{\mathbf{x}}_0$ is inside A_c but not on the boundary C then the relationship

$$\hat{p} = \int_C \hat{p}\, \hat{\mathbf{n}} \cdot \nabla G(\hat{\mathbf{x}}, \hat{\mathbf{x}}_0) - G(\hat{\mathbf{x}}, \hat{\mathbf{x}}_0)\, \hat{\mathbf{n}} \cdot \nabla \hat{p}\, dC \tag{2.79}$$

holds, if $\hat{\mathbf{x}}_0$ is outside of the A_c then we get

$$0 = \int_C \hat{p}\, \hat{\mathbf{n}} \cdot \nabla G(\hat{\mathbf{x}}, \hat{\mathbf{x}}_0) - G(\hat{\mathbf{x}}, \hat{\mathbf{x}}_0)\, \hat{\mathbf{n}} \cdot \nabla \hat{p}\, dC \tag{2.80}$$

and finally when $\hat{\mathbf{x}}_0$ is on the boundary C we have the result

$$\hat{p} = 2 \int_C \hat{p}\, \hat{\mathbf{n}} \cdot \nabla\, G\left(\hat{\mathbf{x}}, \hat{\mathbf{x}}_0\right) - G\left(\hat{\mathbf{x}}, \hat{\mathbf{x}}_0\right) \hat{\mathbf{n}} \cdot \nabla \hat{p}\, dC. \tag{2.81}$$

This last case when $\hat{\mathbf{x}}_0$ is on the boundary C is most important to us as it is the assessment of points on the interface of the crack which allow for the use of boundary integral methods.

Upon discretisation of the integral equation (2.81) into a summation over N straight lines or elements each with a centre given by $\hat{\mathbf{x}}_0$ this gives the result

$$\hat{p}\left(\hat{\mathbf{x}}_0\right) = -2 \sum_{i=1}^{N} \alpha_i \left(\frac{\partial \hat{p}}{\partial n}\right)_i + 2 \sum_{i=1}^{N} \beta_i \hat{p}_i. \tag{2.82}$$

Here the influence coefficients α_1 and β_i are given by

$$\alpha_i = \int_{S_i} G\left(\hat{\mathbf{x}}, \hat{\mathbf{x}}_0\right) dl \tag{2.83}$$

and

$$\beta_i = \int_{S_i} \hat{\mathbf{n}} \cdot \nabla G\left(\hat{\mathbf{x}}, \hat{\mathbf{x}}_0\right) dl. \tag{2.84}$$

Here S_i represents the element being integrated over, parametrised by $l\left(\hat{\mathbf{x}}\right)$.

At this point the values of the influence coefficients need to be assessed differently depending on whether or not the evaluation point $\hat{\mathbf{x}}_0$ occurs inside or outside of the ith boundary element.

For the case when the evaluation point occurs outside of the boundary element in question the influence coefficients are non-singular and can be approximated accurately using Gauss-Legendre quadrature [Pozrikidis, 2002]. This gives the resulting equations

$$\alpha_i \approx \frac{l}{2} \sum_{k=1}^{N_Q} G\left(\hat{\mathbf{x}}\left(\xi_k\right), \hat{\mathbf{x}}_0\left(\xi_k\right)\right) w_k \tag{2.85}$$

and

$$\beta_i \approx \frac{l}{2} \sum_{k=1}^{N_Q} \hat{\mathbf{n}} \cdot \nabla G\left(\hat{\mathbf{x}}\left(\xi_k\right), \hat{\mathbf{x}}_0\left(\xi_k\right)\right) w_k. \tag{2.86}$$

This method of approximating an integral works by taking the sum of N_Q points parametrised by ξ_k all weighted by a factor of w_k.

The case when $\hat{\mathbf{x}}_0$ is present in the ith boundary element is more complicated. In this scenario as $\hat{\mathbf{x}}$ approaches $\hat{\mathbf{x}}_0$ both (2.83) and (2.84) exhibit singularities. These singularities can be avoided by subtracting the free-space kernels from the integrals to remove the singularity then calculating their value separately. For α_i this gives

$$\alpha_i = \int_{S_i} \left(G\left(\hat{\mathbf{x}}, \hat{\mathbf{x}}_0\right) + \frac{1}{2\pi} \ln\left|\hat{\mathbf{x}} - \hat{\mathbf{x}}_0\right|\right) dl + \alpha_i^{FS}, \tag{2.87}$$

while for β_i this results in

$$\beta_i = \int_{S_i} \left(\hat{\mathbf{n}} \cdot \nabla G\left(\hat{\mathbf{x}}, \hat{\mathbf{x}}_0\right) + \frac{1}{2\pi} \frac{\hat{\mathbf{n}} \cdot \left(\hat{\mathbf{x}} - \hat{\mathbf{x}}_0\right)}{\left|\hat{\mathbf{x}} - \hat{\mathbf{x}}_0\right|^2} \right) dl + \beta_i^{FS}. \tag{2.88}$$

Here the free-space forms of the influence coefficients are given by

$$\alpha_i^{FS} = \int_{S_i} -\frac{1}{2\pi} \ln\left|\hat{\mathbf{x}} - \hat{\mathbf{x}}_0\right| dl \tag{2.89}$$

and

$$\beta_i^{FS} = \int_{S_i} -\frac{1}{2\pi} \frac{\hat{\mathbf{n}} \cdot \left(\hat{\mathbf{x}} - \hat{\mathbf{x}}_0\right)}{\left|\hat{\mathbf{x}} - \hat{\mathbf{x}}_0\right|^2} dl. \tag{2.90}$$

These free-space kernals were chosen by considering the free space Green's function given by [Gaul et al., 2003, Pozrikidis, 2002]

$$G\left(\hat{\mathbf{x}}, \hat{\mathbf{x}}_0\right) = -\frac{1}{2\pi} \ln\left|\hat{\mathbf{x}} - \hat{\mathbf{x}}_0\right| \tag{2.91}$$

which equates to the singular component of any chosen Green's function [Pozrikidis, 2002]. The subtraction of this function was chosen to remove the singularity from α_i and the subtraction of the dot product of $\hat{\mathbf{n}}$ with the grad of the free-space Greens function was used to remove the singularity from β_i. Now that this has been done the first integrals on the right hand side of (2.87) and (2.88) are non-singular and may be solved using Gauss-Legendre quadrature in the same way as when analysing the non-singular elements.

Now it remains to solve the value of the free space forms of the influence coefficients. α_i^{FS} is weakly singular and so can be integrated directly [Gaul et al., 2003]. Here it helps to use the substitution $\left|\hat{\mathbf{x}} - \hat{\mathbf{x}}_0\right| = |l - l_0|$ where $\hat{\mathbf{x}}_0$ lies at l_0. This gives

$$\alpha_i^{FS} = \int_{l_i}^{l_{i+1}} -\frac{1}{2\pi} \ln|l - l_0| \, dl, \tag{2.92}$$

resulting in

$$\alpha_i^{FS} = -\frac{1}{2\pi} \left[|l_i - l_0| \left(\ln|l_i - l_0| - 1 \right) + |l_{i+1} - l_0| \left(\ln|l_{i+1} - l_0| - 1 \right) \right], \tag{2.93}$$

where l_i and l_{i+1} are the end points of the segments.

For β_i^{FS} as $\hat{\mathbf{x}}$ approaches $\hat{\mathbf{x}}_0$, the normal to the surface $\hat{\mathbf{n}}$ becomes orthogonal to the tangent vector $(\hat{\mathbf{x}} - \hat{\mathbf{x}}_0)$ and as such the numerator vanishes leading to the result

$$\beta_i^{FS} = 0. \tag{2.94}$$

Since the singularities in the integrals have been resolved we can proceed to set up a linear system of equations. Rewriting (2.82) as a series of equations with varying $\hat{\mathbf{x}}_0$ gives

$$\frac{1}{2}\hat{p}_j = -A_{ji}\hat{p}_i' + B_{ji}\hat{p}_i, \tag{2.95}$$

where A_{ji} and B_{ji} correspond to $\sum_{i=1}^{N} \alpha_i (\hat{\mathbf{x}}_0)$ and $\sum_{i=1}^{N} \beta_i (\hat{\mathbf{x}}_0)$ respectively. This can be manipulated to give

$$A_{ji}\hat{p}_i' = \left(B_{ji} - \frac{1}{2}\delta_{ji} \right) \hat{p}_i \tag{2.96}$$

which can then be written in matrix form

$$\mathbf{A}\hat{\mathbf{p}}' = \left(\mathbf{B} - \frac{1}{2}\mathbf{I} \right) \hat{\mathbf{p}}. \tag{2.97}$$

Here $\mathbf{I}$ is the identity matrix while $\mathbf{A}$ and $\mathbf{B}$ are the matrix representations of A_{ji} and A_{ji} respectively while $\hat{\mathbf{p}}$ is the vector form of $\hat{p}_i$ This sets up a system of linear equations which when computed allow $\hat{\mathbf{p}}'$ to be found. $\hat{\mathbf{p}}'$ can then be used in conjunction with (2.13) to compute the movement of the interface at each point along it. This movement of the interface can then be directly compared to the movement seen in experiments carried out later in the chapter.

2.2.7 Alternative Domains for the Numerical Solution

Now that the numerical solution has been examined the next stage is to formalise the domains in which it will be computed. For this step the Green's function for each domain must be found.

The solution to the free space Green's function was already touched upon in the last section and can be written as [Gaul et al., 2003, Pozrikidis, 2002]

$$G = -\frac{1}{2\pi} \ln |\hat{\mathbf{x}} - \hat{\mathbf{x}}_0| , \tag{2.98}$$

where G is the Green's function, $\hat{\mathbf{x}} (\hat{x}, \hat{y})$ is the varying field point and $\hat{\mathbf{x}}_0 (\hat{x}_0, \hat{y}_0)$ is the constant singular point. This Green's function will be used when considering a crack with semi-infinite domain extending infinitely in the $\pm\hat{x}$ and $-\hat{y}$ directions.

To ensure that the semi-infinite domain meets the assumptions set out in the derivation of the numerical method it is defined here as being bounded by the free surface of the bitumen, including the crack over all of which $\hat{p}$ is defined. In addition the domain is considered bounded by the lines $\hat{x} = \pm b$ for the limit as b approaches ∞ and the line $\hat{y} = a$ for the limit as a approaches $-\infty$. On these three lines the velocity of the fluid is considered to be zero. Here on the lines where the velocity is equal to zero the pressure gradient is also equal to zero. This means that the final matrix calculation in (2.97) reduces to integrating over just the free surface.

Using a semi-infinite domain is a good approximation to real world problems but for comparison to the experiments performed in this research a measurable finite domain is more desirable. This can be achieved by changing the Green's function in the boundary integral method.

The easiest way to model a domain of finite width is to model a periodically repeating infinite domain where the velocity of the fluid is zero on the periodically repeating edges of the domain. Due to this boundary condition the system will act in the same way as a finite width walled system. For the moment we will still consider a domain of infinite depth for simplicity but a domain of finite depth will be studied later in the research.

A Green's function of

$$G = \frac{1}{\pi} \ln \left(2 \left| \sin \frac{1}{b\pi} \left(\hat{x} - \hat{x}_0 + i \left(\hat{y} - \hat{y}_0 \right) \right) \right| \right) \tag{2.99}$$

can be used to represent a source at $(\hat{x}_0, \hat{y}_0)$ for a domain which is periodic in the $\hat{x}$ direction with period b [Linton, 1999, Moroz, 2006]. Here $\hat{x}$ and $\hat{y}$ are the coordinates of the varying field point, G is the Green's function appropriate to the domain and b is the width of the periodically repeating part of the domain.

To avoid the use of complex numbers this can then be simplified to

$$G = \frac{1}{4\pi} \ln \left(2 \left(\cosh \left(\frac{2\pi \left(\hat{y} - \hat{y}_0 \right)}{b} \right) - \cos \left(\frac{2\pi \left(\hat{x} - \hat{x}_0 \right)}{b} \right) \right) \right) + \frac{\left(\hat{y} - \hat{y}_0 \right)}{4b}, \tag{2.100}$$

where the final term is an addition chosen to ensure that $\partial G / \partial \hat{y}$ tends to 0 as $\hat{y}$ tends to $-\infty$.

To formally define the boundaries of the domain they are considered to be the free surface of the bitumen where $\hat{p}$ is defined as stated in the modelling section and the lines $\hat{x} = \pm b$ and the line $\hat{y} = a$ for the limit as a approaches $-\infty$. For each of these lines the velocity of the fluid is equal to 0 on the line. As with the previous domain, the condition that the velocity is equal to zero and by association the pressure gradient in some parts of the boundary causes (2.97) to collapse to an integral over the boundary.

Using the process described using (2.82)-(2.97) this Green's function was computed to create a model describing the movement of the crack over time.

Next we have to introduce a finite depth to the system to accurately model the experiments where the cracks are large relative to the size of the sample. This can be achieved by applying the method of images [Li, 1998] to (2.100) which results in the following as a new Green's function

$$G = \frac{1}{4\pi} \ln \left(\frac{\left(\cosh \left(\frac{2\pi(\hat{y} - \hat{y}_0)}{b} \right) - \cos \left(\frac{2\pi(\hat{x} - \hat{x}_0)}{b} \right) \right)}{\left(\cosh \left(\frac{2\pi(\hat{y} + \hat{y}_0 - 2a)}{b} \right) - \cos \left(\frac{2\pi(\hat{x} - \hat{x}_0)}{b} \right) \right)} \right) - \frac{\hat{y}_0 - a}{2b} \tag{2.101}$$

where G is the Green's function, b is the width of the periodically repeating part of the domain and a is vertical displacement between the base of the domain and the origin. Again $\hat{x}$ and $\hat{y}$ are the coordinates of the varying point of the surface while $\hat{x}_0$ and $\hat{y}_0$ the coordinates of the constant singular source.

For this Green's function the closed domain is bounded by the surface of the crack where $\hat{p}$ is known, and the lines $\hat{x} = \pm b$ and $\hat{y} = a$ on which, the condition that the velocity of the fluid is zero holds. For the sections of the boundary where the velocity is equal to zero the pressure gradient is also zero so the boundary integral equation reduces to one over just the free surface.

Next, the process described using (2.82)-(2.97) was computed to create a model describing the movement of the crack over time.

2.2.8 Time-stepping

Now that the numerical method being used to compute the movement of the surface has been defined we can address the method of time-stepping used to advect the interface. To perform time-stepping while using the boundary integral solution the Crank-Nicholson method [Crank and Nicolson, 1947] was used. This is an implicit time-stepping method which follows the formula

$$\hat{Y}^{n+1} = \hat{Y}^n + \frac{1}{2}\left[f_g\left(\hat{t}^n, \hat{Y}^n\right) + f_g(\hat{t}^{n+1}, \hat{Y}^{n+1})\right]\Delta\hat{t}. \tag{2.102}$$

Here $\hat{Y}^n$ is the position of the surface before the n^{th} time-step takes place, $\hat{t}^n$ is the time before the n^{th} time-step takes place, $\Delta\hat{t}$ is the size of the time-step and $f_g\left(\hat{t}^n, \hat{Y}^n\right)$ is the value of the pressure gradient on the surface. In this method the value of $\hat{Y}^{n+1}$ is derived iteratively.

2.3 Materials and Methodology

Now that a method of tracking the movement of bitumen over time has been established the experiments performed and materials used in the experiments will be discussed. This includes details of the bitumen used in the experiments, the process of the crack flow tests which were used to validate the model and the tests used to determine the properties of the bitumen used to allow a proper comparison with numerical results.

2.3.1 Bitumen

Five different types of bitumen were used throughout the chapter to ensure the comparisons to the model could be replicated over a variety of surface tensions and viscosities. The relevant properties of the types of bitumen used can be found in Table 2.1.

Bitumen type	Surface tension (Nm^{-1})	Dynamic viscosity (MPl)
Sample 1	0.0324	0.103
Sample 2	0.0374	0.784
Sample 3	0.0318	0.328
Sample 4	0.0300	1.103
Sample 5	0.0391	0.892

Table 2.1: A table with the surface tensions and viscosities of each type of bitumen used in the chapter.

2.3.2 Crack Flow Test

To validate the accuracy of the model experiments were performed with cracks of two different sizes allowing a direct comparison of predictions of the model to experimental results.

I poured heated bitumen into a silicone mould which produced a thin sheet of bitumen of dimensions 73×23×1 mm. The sheets of bitumen had triangular gaps in the longest edge to simulate a crack. This allowed the observation of the bitumen flowing into the gap. The gaps were in two sizes with maximum widths of 10 mm and 20 mm. The height of the crack was always 10 mm. Next the mould and bitumen were placed in a freezer at -20°C for a period of at least two hours. This was done to prevent the sample from deforming during the process of removing it from the mould.

The sheets of bitumen were placed between two glass plates to form a Hele-Shaw cell. Here the thickness of the sample ensured that it behaved as if in a porous medium [Nield and Bejan, 2006, Richardson, 1972]. The bottom and sides of the sheet were then sealed with plasticine to prevent the bitumen from leaving the confines of the plates.

Next the samples were placed in an oven which had been pre-heated to 45°C for 30 mins with pictures taken every 30 minutes to record the movement of the bitumen. The flow of the bitumen into the crack was quantified using graph paper stuck to the back of the sample. An example of the experimental set-up can be seen in Fig. 2.11.

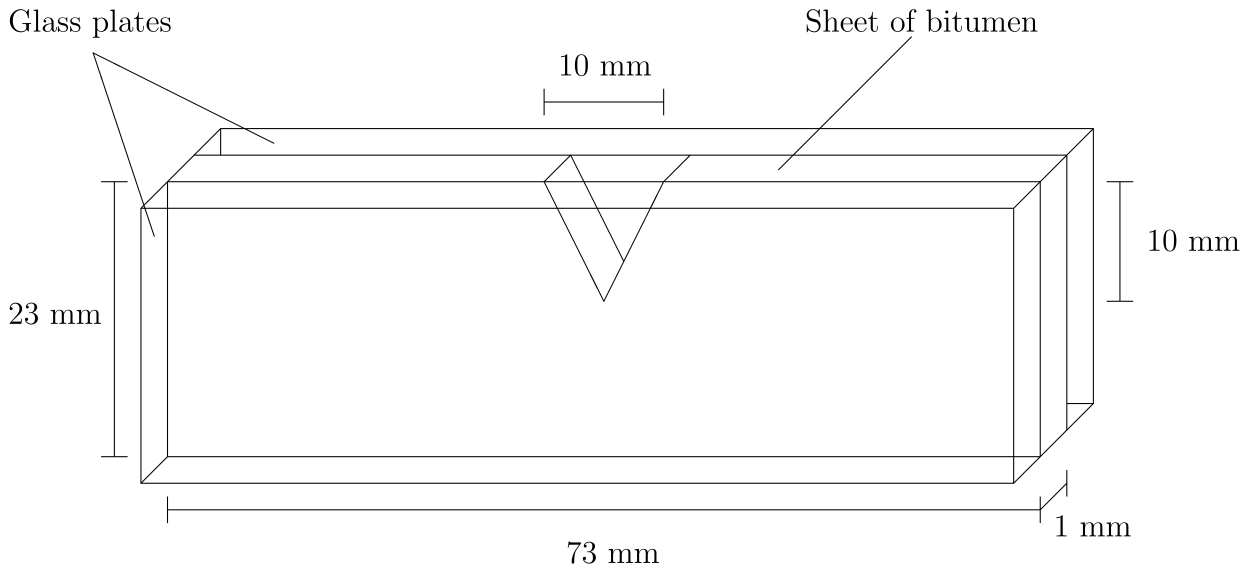

Figure 2.11: The above schema displays the setup of the crack flow test. It comprises of a 73×23×1 mm sheet of bitumen with a triangular section removed sandwiched between two glass plates. After being placed in an oven at 45°C the flow of this sheet of bitumen is monitored over time. This image displays the triangular section taken out of the sheet of bitumen to have a height of 10 mm and a maximum width of 10 mm. Another set of experiments were also run using triangles with a height of 10 mm and maximum width 20 mm.

In addition to this the test was also performed underwater. This allows the movement of the bitumen due to surface tension to be isolated and eliminates the effects of gravity on the sample. In these experiments the bitumen slides were completely submerged in a clear container of water pre-heated to 45°C with photos taken every 30 minutes.

2.3.3 Surface Tension Test

First each type of bitumen was heated at 130°C to allow it to be poured over glass slides. These were then laid to rest for 24 hours while being covered to prevent dust from contaminating the samples. After the rest period had concluded a goniometer was used to measure the curvature of a series drop of test liquids placed on each sample. The test liquids used here were water, ethylene glycol and diiodomethane. Measurements were taken of six drops of each liquid on each type of bitumen used in the chapter to ensure reliability. The set-up for these experiments is displayed in Fig. 2.12.

Given that the surface energy of the liquids is known this can be used in conjunction with

$$\gamma_{\mathrm{S}} = \gamma_{\mathrm{SL}} + \gamma_{\mathrm{L}} \cos\theta, \tag{2.103}$$

where γ_{S} is the surface energy of the bitumen, γ_{SL} is the solid-liquid interface energy, γ_{L} is the surface energy of the test liquid and θ is the contact angle between the bitumen and the test liquid, to derive the surface energy of the bitumen.

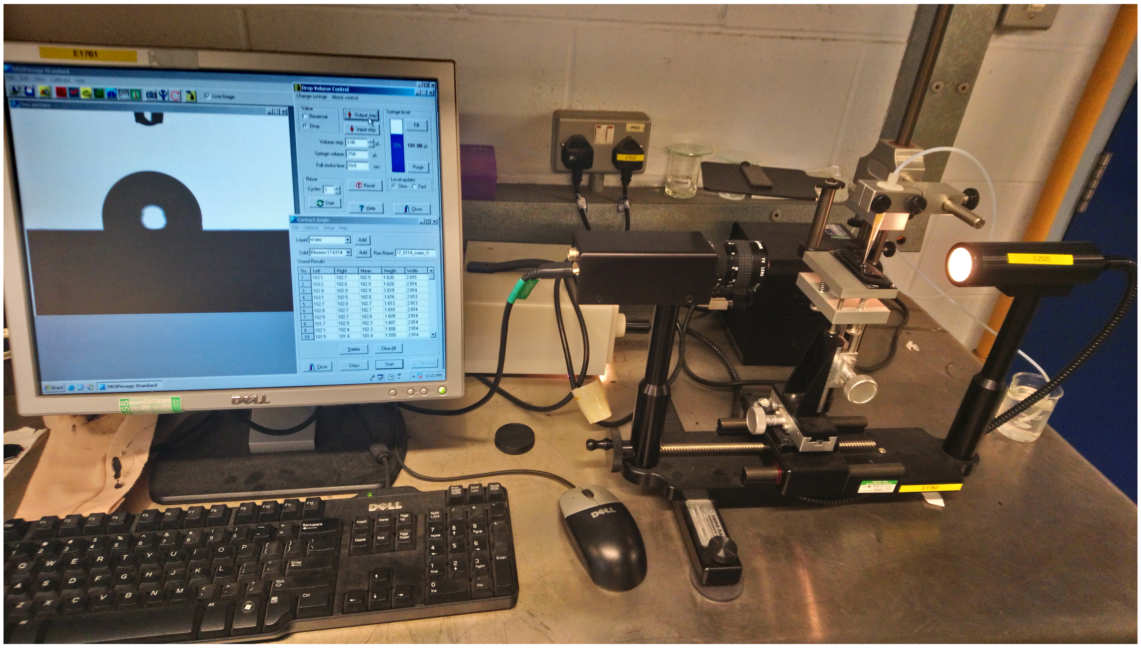

Figure 2.12: The experimental set-up for the surface tension tests. The goniometer on the right shines a light over a drop of liquid on the bitumen sample. This image is captured by a camera attached to the computer which shows the image and can be used to process the results.

2.3.4 Viscosity Tests

A Brookfield viscometer was used to measure the viscosity of the bitumen used throughout this chapter. To measure each sample the heater and spindle of the viscometer were pre-heated for one hour before the test began. After this 9.5 g of bitumen was placed in a tube which in turn was put in the heater for another 30 mins to bring it up to temperature. After the heating period was complete the viscometer was used to measure the viscosity of the sample. Two repeats of each viscosity were taken to ensure the reliability of the results. A picture of the experimental set-up can be found in Fig. 2.13.

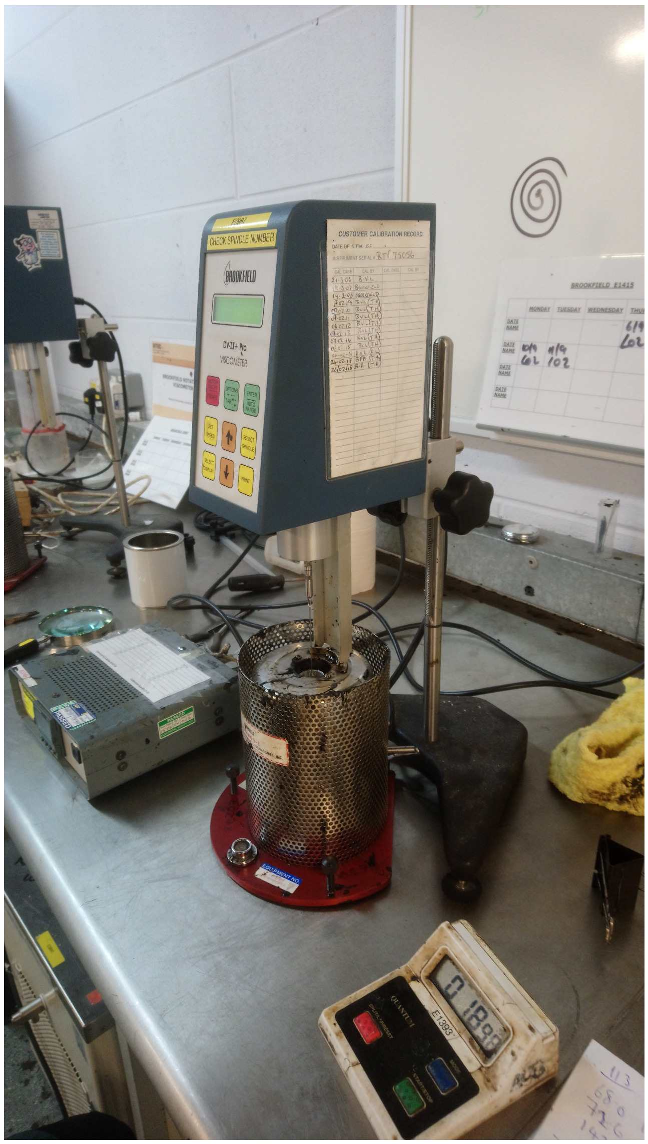

Figure 2.13: The experimental set-up for the viscosity tests. The Brookfield viscometer measures the viscosity of the sample of bitumen placed in the heater below it.

2.4 Results and Discussion

Now that the experimental set-up has been defined, the results of the experiments can be examined. This section will begin with verifying that the numerical solution performs as expected against analytical results and checking it against the small time asymptotic solution. This will be followed by validation against experimental results. Once the experimental comparison has been concluded the results from the numerical method will be used to calibrate a computationally cheap equation for how the height of the tip of the crack varies with time during the self-healing process.

2.4.1 Verification of Numerical Method against Small Time Asymptotic Solution

To examine the results generated using numerical methods they were compared to the small time asymptotic solution found using conformal mapping. This was done using a direct comparison of the value of the pressure gradient on a sample crack when calculated using the two methods.

During this test the numerical system was run without considering the effect of surface tension. This allowed for a better comparison of the two as otherwise the small time asymptotic solution would be invalid at the corners of the system.

Here the value of the small time asymptotic solution is derived using the approximation for a generic crack from subsection 2.2.5. For the comparison the numerical method is derived using a domain of infinite width and depth. The crack which was used to compare the two was a vertical triangular crack with its widest point at the top of the crack and a width of one fifth of its height at its widest point.

To make this comparison the error was defined as

$$\sqrt{\sum \frac{\left((\hat{\mathbf{n}} \cdot \nabla \hat{p})_{\text{Numerical}} - (\hat{\mathbf{n}} \cdot \nabla \hat{p})_{\text{ST}}\right)^2}{N}}, \tag{2.104}$$

where $(\hat{\mathbf{n}} \cdot \nabla \hat{p})_{\text{Numerical}}$ is the differential of the pressure of the system in the direction of the normal to the surface at a point on the surface as calculated by the numerical model. $(\hat{\mathbf{n}} \cdot \nabla \hat{p})_{\text{ST}}$ is the small time asymptotic solution for the differential of the pressure of the system in the direction of the normal to the surface at the same point on the surface. N is the number of points being analysed by the numerical model. This error was calculated for various values of grid spacing, defined as one divided by the non-dimensionalised distance between grid points on the surface of the crack.

As can be seen in Fig. 2.14 as the grid spacing of the system tends to zero the error in the numerical results also tends to zero, which is what would be expected if the numerical solution matches the small time asymptotic solution.

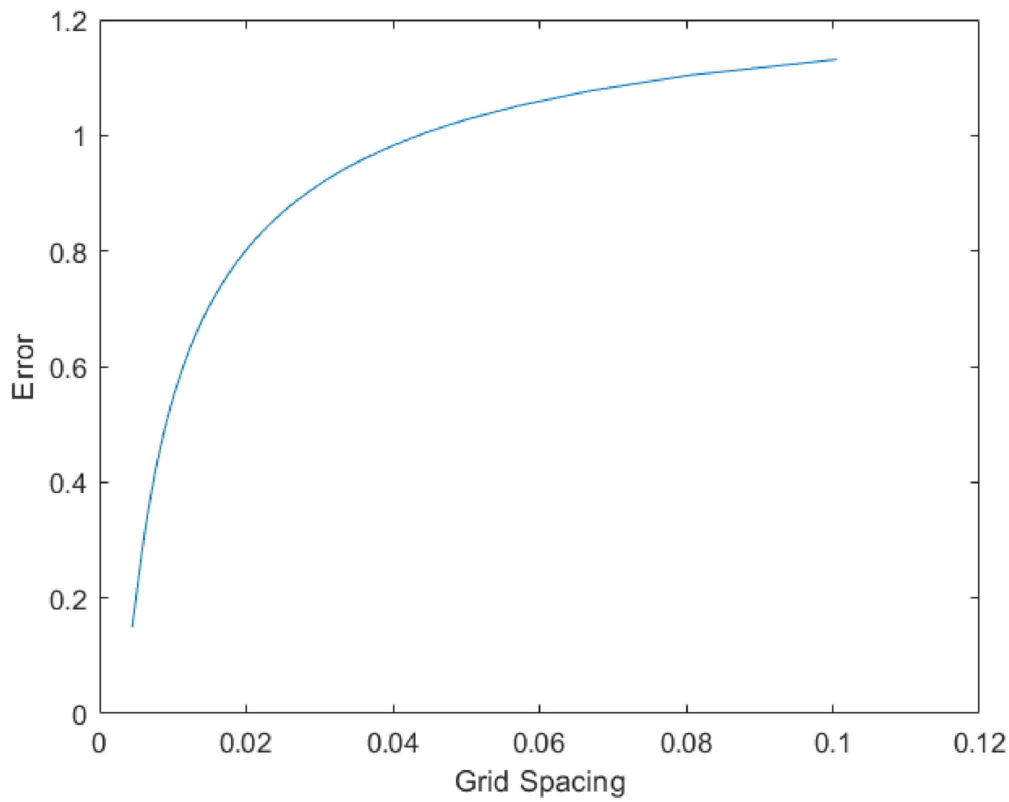

Figure 2.14: A comparison of the error on the numerical solution formed from boundary integral methods to the standard small time asymptotic solution derived from conformal mapping.

2.4.2 Verification of Numerical Solution against Analytical Solutions

Next we verify the accuracy of the numerical solution to Laplace's equation against known analytical solutions to gain a measure of confidence in the mathematics behind the model. Here we compare how the error on the initial value of the pressure gradient on a test surface varies with the grid spacing used in the simulation.

These comparisons will take the boundary integral calculations and compare them to an artificial problem which uses a potential $\hat{p}$ which is chosen to ensure that $\nabla\hat{p} = 0$ at the edges of the domain or tends to 0 or as the co-ordinates $\hat{x}$ and $\hat{y}$ tend to $\pm\infty$ for a domain which expands infinitely in the relevant direction. The chosen potentials do not necessarily obey the boundary conditions on the surface. This can be used to show that in each case as grid spacing tends to zero so does the error on the model.

Firstly the boundary integral method for modelling the self-healing process in a semi-infinite domain was assessed for accuracy against a known analytical solution. The surface used here was

$$\hat{y} = 1 - \exp\left(-\hat{x}^2\right) \tag{2.105}$$

and the potential of the system was defined to be

$$\hat{p} = \frac{\hat{x}^2 - (\hat{y}-1)^2}{\left(\hat{x}^2 + (\hat{y}-1)^2\right)^2}. \tag{2.106}$$

Here $\hat{x}$ and $\hat{y}$ represent the horizontal and vertical co-ordinates of the system respectively while $\hat{p}$ is the potential of the system. To remain consistent with the domain choice $\nabla\hat{p} \to 0$ as $\hat{x} \to \pm\infty$ and as $\hat{y} \to -\infty$.

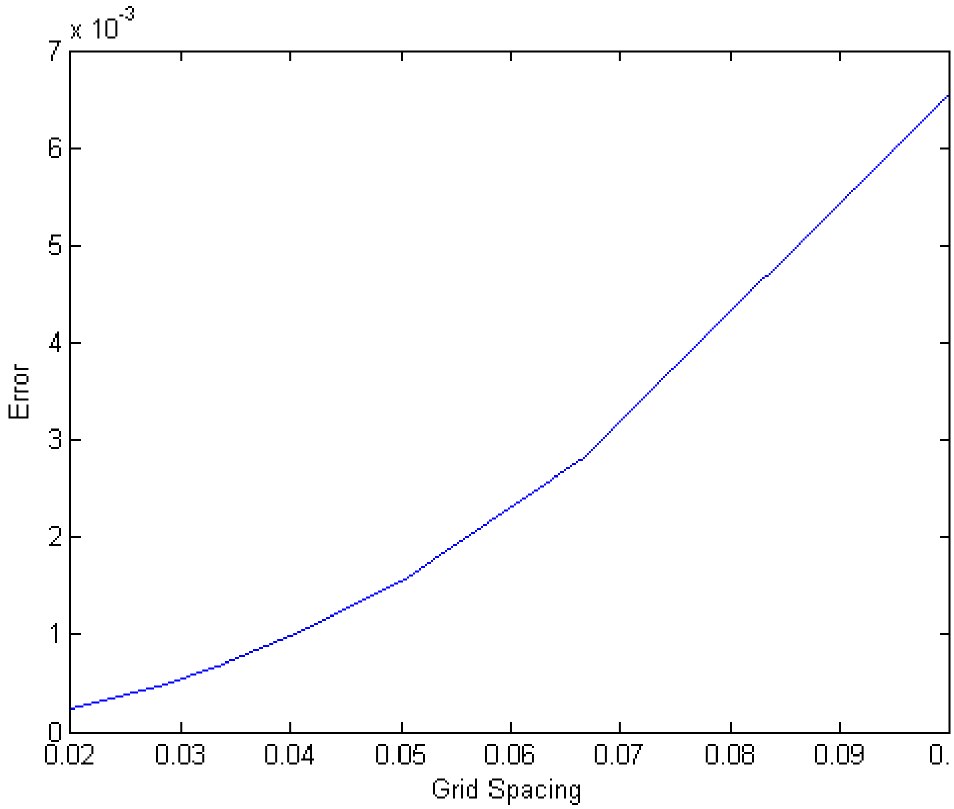

Figure 2.15: This looks at the error when comparing the numerical model with a domain of infinite width and depth with an exact analytical solution. Here the error is plotted against the grid spacing used in the numerical solution.

The average error on the values of $\hat{\mathbf{n}} \cdot \nabla\hat{p}$ at each point evaluated by the numerical solution was compared. This error was calculated using

$$\sqrt{\sum \frac{\left((\hat{\mathbf{n}} \cdot \nabla\hat{p})_{\text{Numerical}} - (\hat{\mathbf{n}} \cdot \nabla\hat{p})_{\text{Analytical}}\right)^2}{N}}. \tag{2.107}$$

Here $(\hat{\mathbf{n}} \cdot \nabla\hat{p})_{\text{Numerical}}$ is the differential of the pressure of the system in the direction of the normal to the surface at a point on the surface generated by the numerical solution.

$(\hat{\mathbf{n}} \cdot \nabla \hat{p})_{\text{Analytical}}$ is the analytical solution for the differential of the pressure of the system in the direction of the normal to the surface at the same point on the surface and N is the number of points being compared across the solutions.

This was performed with various different spacings between each point used to represent the surface and keeping a constant domain size of 40. The results of this can be seen in Fig. 2.15. This clearly shows that as the spacing between the points tends to 0 the error in the calculation of $\hat{\mathbf{n}} \cdot \nabla \hat{p}$ using the numerical solution also tends to 0 which is what would be expected if the model works.

After this the size of the domain taken into account in the numerical solution was varied while the spacing between points remained constant. As can be seen in Fig. 2.16 the error decays inversely proportionally to the domain size squared. Again this helps verify the numerical solution as it is exactly what would be expected according to the theory if the model works.

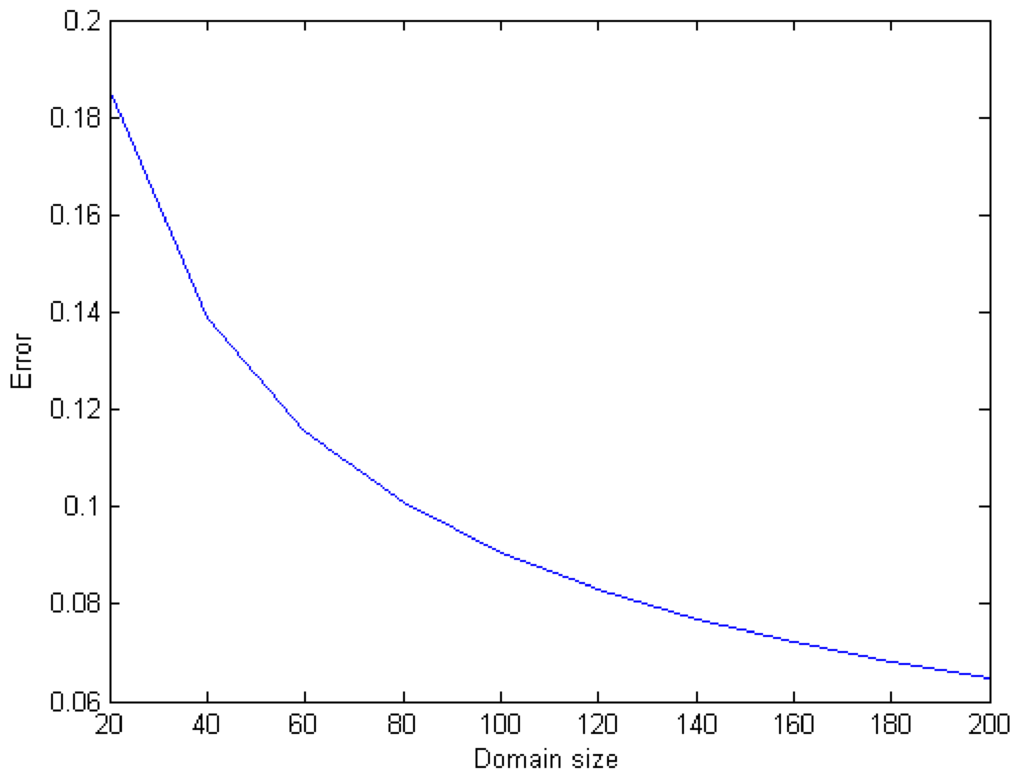

Figure 2.16: This looks at the error when comparing the numerical model with a domain of infinite width and depth with an exact analytical solution. Here the error is plotted against the width of the domain size which was included in the numerical solution.

The next step was to assess the accuracy of the numerical solution with a domain of finite width and infinite depth against a known analytical solution, the results of which can be seen in Fig. 2.17. For this a surface of

$$\hat{y} = 1 - \exp\left(-\hat{x}^2\right) \tag{2.108}$$

and a potential of

$$\hat{p} = -\sin^2\left(\frac{2\pi\hat{x}}{b}\right)\exp\left(\frac{2\pi\hat{y}}{b}\right) \tag{2.109}$$

were used. Here $\hat{x}$ and $\hat{y}$ are the horizontal and vertical co-ordinates of the system respectively, $\hat{p}$ is the potential of the system and b is the width of the periodically repeating domain. This potential satisfies the conditions $\nabla\hat{p} = 0$ at $\hat{x} = \pm b/2$ and $\nabla\hat{p} \to 0$ as $\hat{y} \to 0$.

The value of $\hat{\mathbf{n}} \cdot \nabla\hat{p}$ for the finite width domain and infinite depth were then compared to the exact value produced by the analytical system using (2.107). This is done for varying spacings of points used to model the surface and as would be expected if the model works as the spacing tends to 0 so does the error on the numerical solution.

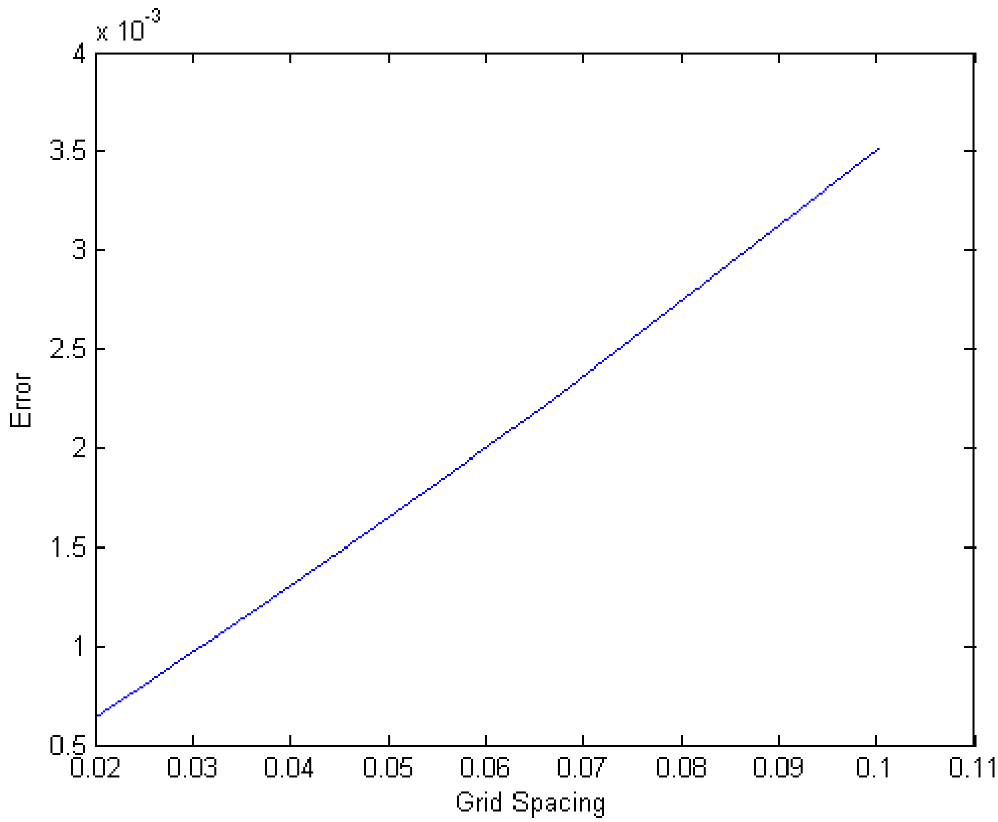

Figure 2.17: This looks at the error when comparing the numerical model with a domain of infinite depth and infinite periodically repeating sections with an exact analytical solution. Here the error is plotted against the grid spacing used in the simulation.

After this the accuracy of the finite width and finite depth domain numerical solution was tested against a known analytical solution, the results of which can be seen in

Fig. 2.18. Here a surface of

$$\hat{y} = 1 - \exp\left(-\hat{x}^2\right) \tag{2.110}$$

and a potential of

$$\hat{p} = -\sin^2\left(\frac{2\pi\hat{x}}{b}\right)\exp\left(\frac{2\pi\hat{y}}{b}\right) + \sin^2\left(\frac{2\pi\hat{x}}{b}\right)\exp\left(\frac{2\pi\left(-\hat{y}+2a\right)}{b}\right) \tag{2.111}$$

were used. In this case $\hat{x}$ and $\hat{y}$ are the horizontal and vertical co-ordinates of the system respectively, $\hat{p}$ is the potential of the system, b is the width of the periodically repeating part of domain and a is its depth. The potential here was chosen so that $\nabla\hat{p} = 0$ when $\hat{x} = \pm b/2$ as well as when $\hat{y} = -a$.

The error of the value of $\hat{\mathbf{n}} \cdot \nabla\hat{p}$ produced by the numerical solution is then compared to the exact value produced by the analytical system using (2.107). This is done for varying spacings of points used to model the surface and as would be expected if the model works as the spacing tends to 0 so does the error on the numerical solution.

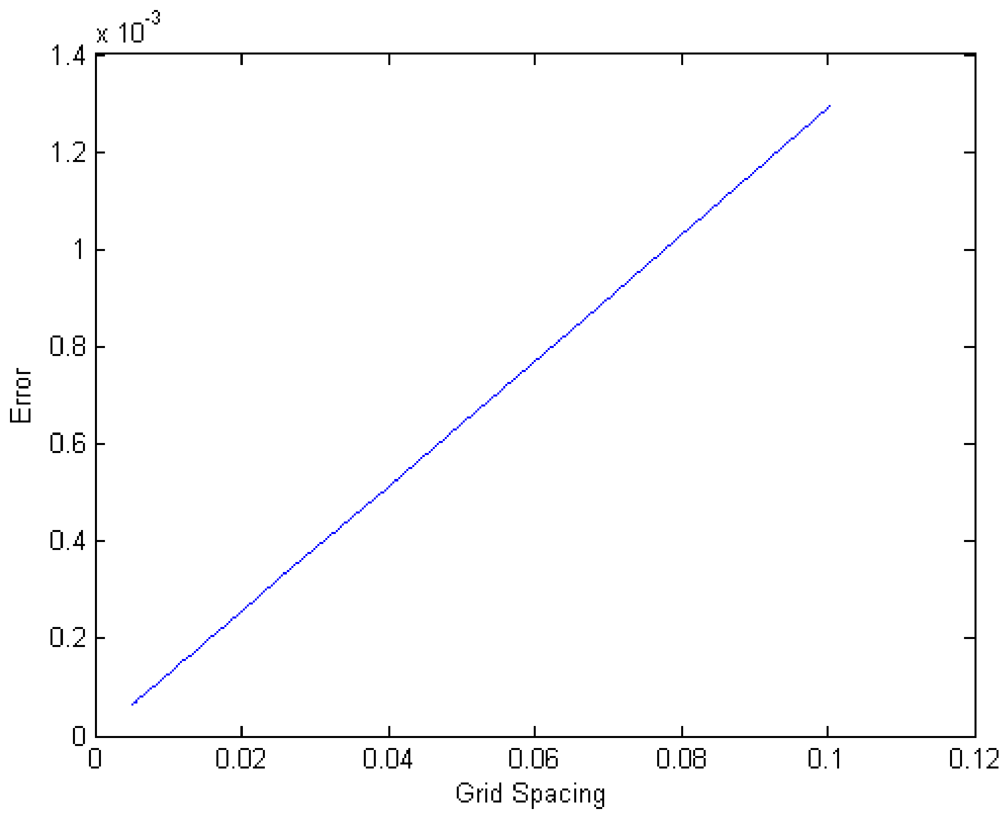

Figure 2.18: This looks at the error when comparing the numerical model with a domain of finite depth and infinite periodically repeating sections with an exact analytical solution. Here the error is plotted against the grid spacing used in the numerical solution.

2.4.3 Verification of Numerical Values of Surface Tension

To verify the model's calculation of the pressure due to surface tension the calculation was compared to the analytical value of the pressure over the surface. To do this the curvature, $\hat{\kappa}$, needs to be defined analytically. This is done using

$$\hat{\kappa} = 1/r = \lim_{\Delta\theta \to 0} \frac{\Delta\theta}{\Delta s} = \frac{d\theta}{ds}. \tag{2.112}$$

Here r is the radius of the curvature, $\Delta\theta$ is the difference in angle of the tangents to the surface at two points on the surface, Δs is the arc length between the same two points on the surface. From here you can use the fact that

$$\frac{d\theta}{ds} = \frac{d\theta}{d\hat{x}}\frac{d\hat{x}}{ds} \tag{2.113}$$

and that by definition

$$\tan\theta = \frac{d\hat{y}}{d\hat{x}}. \tag{2.114}$$

It follows that

$$\frac{d\theta}{d\hat{x}} = \frac{d}{d\hat{x}}\tan^{-1}\frac{d\hat{y}}{d\hat{x}} = \frac{\frac{d^2\hat{y}}{d\hat{x}^2}}{1 + \left(\frac{d\hat{y}}{d\hat{x}}\right)^2} \tag{2.115}$$

and

$$\frac{d\hat{x}}{ds} = \frac{1}{\left(\frac{ds}{d\hat{x}}\right)} = \frac{1}{\sqrt{1 + \left(\frac{d\hat{y}}{d\hat{x}}\right)^2}}. \tag{2.116}$$

Here $\hat{x}$ and $\hat{y}$ are the horizontal and vertical co-ordinates in space respectively. This results in

$$\hat{\kappa} = \frac{d\theta}{ds} = \frac{\frac{d^2\hat{y}}{d\hat{x}^2}}{\left[1 + \left(\frac{d\hat{y}}{d\hat{x}}\right)^2\right]^{\frac{3}{2}}}. \tag{2.117}$$

Here the sample surface used was $\hat{y} = 1 - \exp(-\hat{x}^2)$. Using (2.117) This results in an analytical curvature of

$$\hat{\kappa} = \frac{2\exp\left(-\hat{x}^2\right) - 4\hat{x}^2\exp\left(-\hat{x}^2\right)}{\left(1 + 4\hat{x}^2\exp\left(-2\hat{x}^2\right)\right)^{\frac{3}{2}}}. \tag{2.118}$$

The error on the pressure was determined using the equation

$$\sqrt{\sum \frac{\left(\hat{p}_{\text{Numerical}} - \hat{p}_{\text{Analytical}}\right)^2}{N}}, \tag{2.119}$$

where $\hat{p}_{\text{Numerical}}$ is the pressure on the boundary due to surface tension determined by the model, $\hat{p}_{\text{Analytical}}$ is the pressure on the boundary due to surface tension analytically and N is the number of points being analysed by the numerical model.

The results of how the error here changes with grid spacing is shown in Fig. 2.19. As can be clearly seen the error on the pressure tends to zero as grid spacing on the numerical model tends to zero. This is as would be expected for a working model.

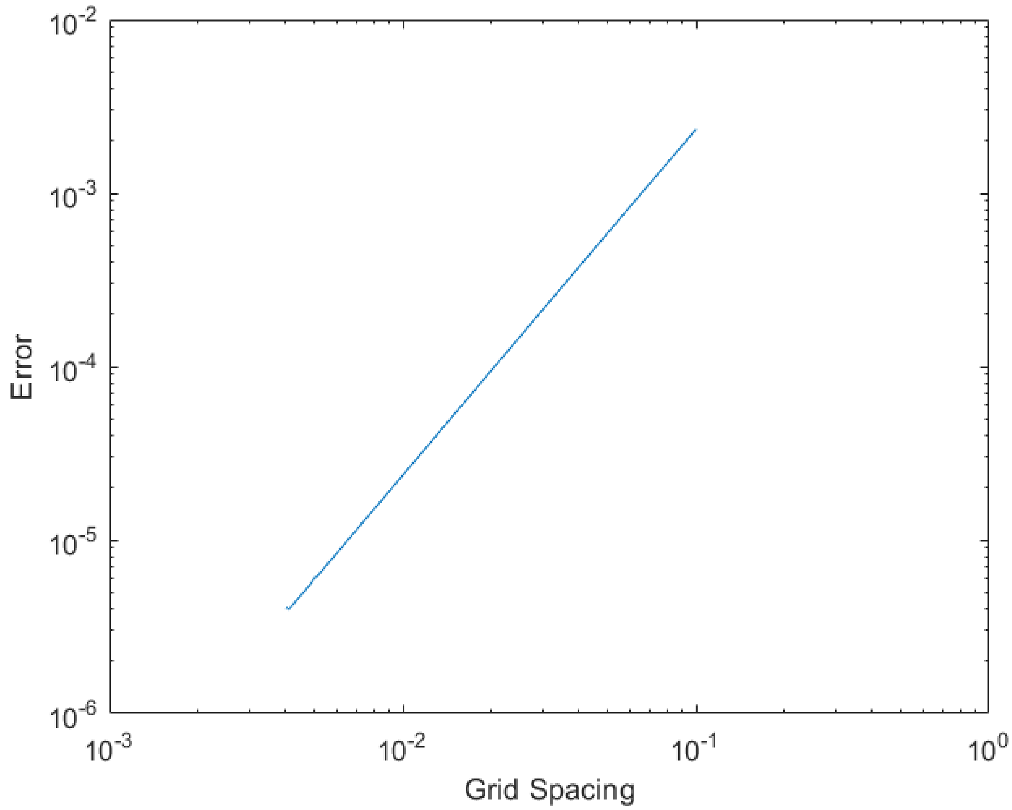

Figure 2.19: This looks at the error on the calculation of surface tension when comparing the numerical model. Here the error is plotted against the grid spacing used in the simulation.

2.4.4 Modelling The Movement of Cracks

Now that the numerical solution has been verified against analytical results and the small time asymptotic solution it is beneficial to look at how different classes of crack heal. In this section a triangular crack with an opening at the top of the system will be evaluated as well as a thin vertical crack with an opening at the top of the system. In addition the simulation will be used to isolate the effects of surface tension and look at how that can drive healing.

Throughout this section a representative Bond number was needed to compute the solutions. This was chosen by assuming a bitumen density of 1030 kgm^{-3}, a crack height of 0.01 m, an acceleration due to gravity of 9.81 ms^{-2} and a surface tension of 0.03 Nm^{-1}. Using these with (2.16) gives a Bond number of 33.681.

The first class of crack to be analysed by the simulation was the triangular crack. This, while it doesn't resemble the style of crack naturally seen in asphalt is the easiest to compare to experiment to validate the model. Here a crack with width at it's widest point equal to its height was modelled. The results of this modelling can be seen in Fig. 2.20.

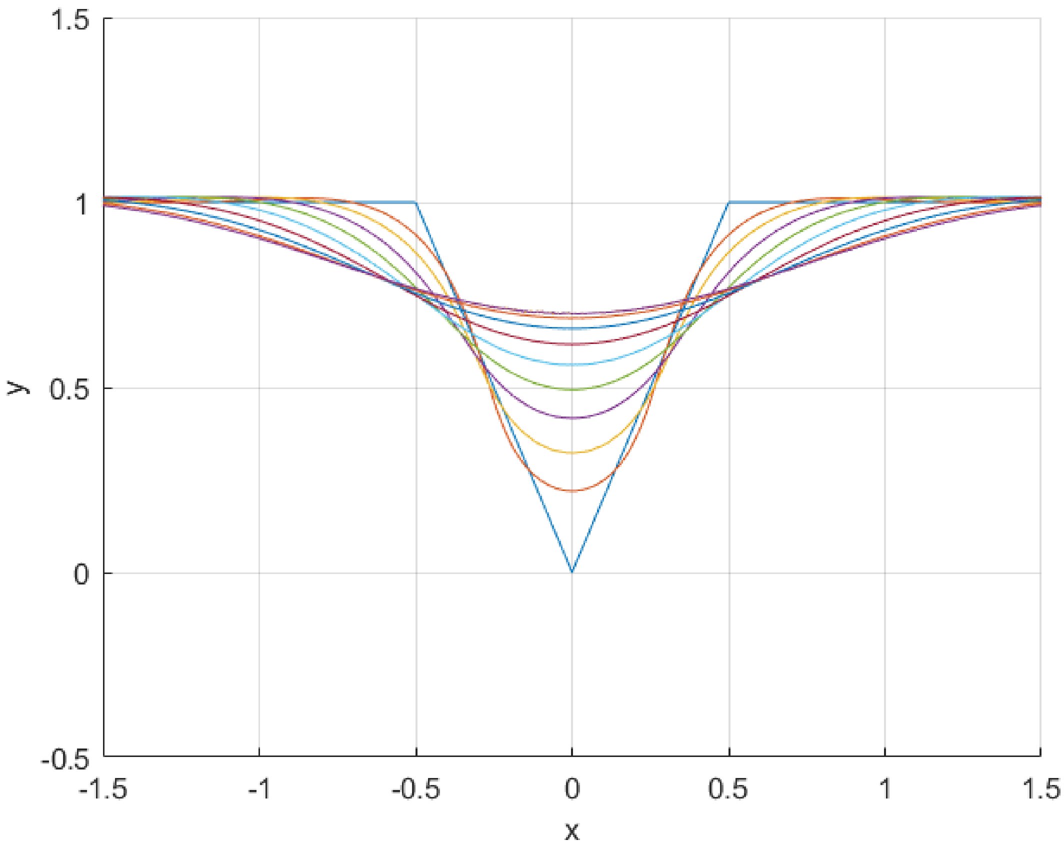

Figure 2.20: This shows the evolution of a triangular crack with time. The dark blue line shows the initial profile of the crack while the other lines show the progression of the healing with time. Here the bond number is taken to be 33.681.

To produce this graph (2.98) was the chosen Green's function with the surface of the crack extending from $\hat{x} = -10$ to $\hat{x} = 10$. Here 1001 equally spaced points were used to represent the surface. A Bond number of $B_o = 33.681$ used. Time-steps of $\hat{t} = 0.001$ were used to move the surface with the lines on the graph corresponding to the evolution of the surface every 100 time-steps. In this case both gravity and surface tension were included in the relevant equations.

From the results of the numerical method, for a triangular crack under the effects of gravity and surface tension it can be seen that the initial movement of the crack is seen at the tip of the crack and at the corners. This initial movement acts to round out any sharp corners to the crack with the most movement being at the tip of the crack. This is logical given the high curvature contributing to driving the initial healing at these points. Once the corners have been smoothed the progress of the tip of the crack slows dramatically, with the second set of time steps only showing half the movement of the tip as was seen in the first step.

As the healing of the crack proceeds the movement of the tip of the crack gets progressively slower as time goes on, this is due to a reduced pressure difference across the crack due to gravity since the surface of the crack is more level and reduced average curvature of the surface. While the crack is being filled the height of the surfaces next to the initial crack is being reduced with the distance over which the surface gets impacted increasing as time goes on. This makes sense as bitumen from the points near the crack which are highest is flowing with gravity into the crack.

Next a thin vertical crack was analysed. This bears a closer resemblance to the types of crack naturally seen in asphalt than the previous triangular class of crack. The progression of the flow of bitumen into the crack is shown in Fig. 2.21.

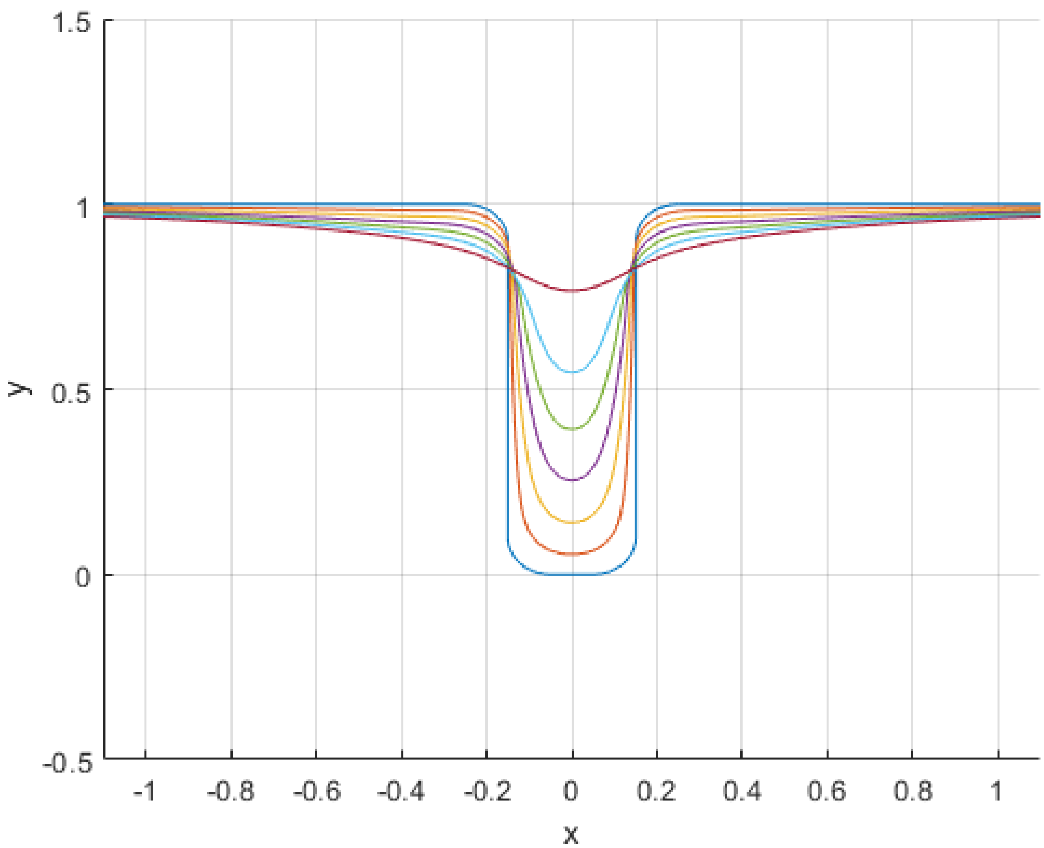

Figure 2.21: This shows the evolution of a thin vertical crack with time. The dark blue line shows the initial profile of the crack while the other lines show the progression of the healing with time. Here the bond number is taken to be 33.681.

To calculate these results (2.98) was selected as the Green's function with the surface of the crack extending from $\hat{x} = -10$ to $\hat{x} = 10$. Here 1001 equally spaced points were used to represent the surface with a Bond number of $B_o = 33.681$ being used. Time-steps of $\hat{t} = 0.001$ were used to advect the interface with the lines on the graph corresponding to the state of the surface every 100 time-steps. Here gravity and surface tension were included in the relevant equations.

One interesting point about this crack which was not observed in the behaviours of other cracks is that the growth of the tip of the crack actually seems to grow faster with time, at least up to the point where the crack has almost healed. This is likely due to a combination of reasons. Here we observe that curved corners present in the initial surface seem to have slowed the sharp initial movement of the crack due to the reduction in the highest point of curvature. In addition we see that as the crack evolves with time its shape changes considerably. While it starts out vertical the sides quickly slope to the point where it soon resembles a slightly smoothed triangular crack. It appears that in this case gravity dominates at first, filling the bottom edges of the crack and steadily increasing the curvature at the tip. As this curvature increases the effect of surface tension increases and combines with the effect of gravity to increase the speed of the healing later in the process.

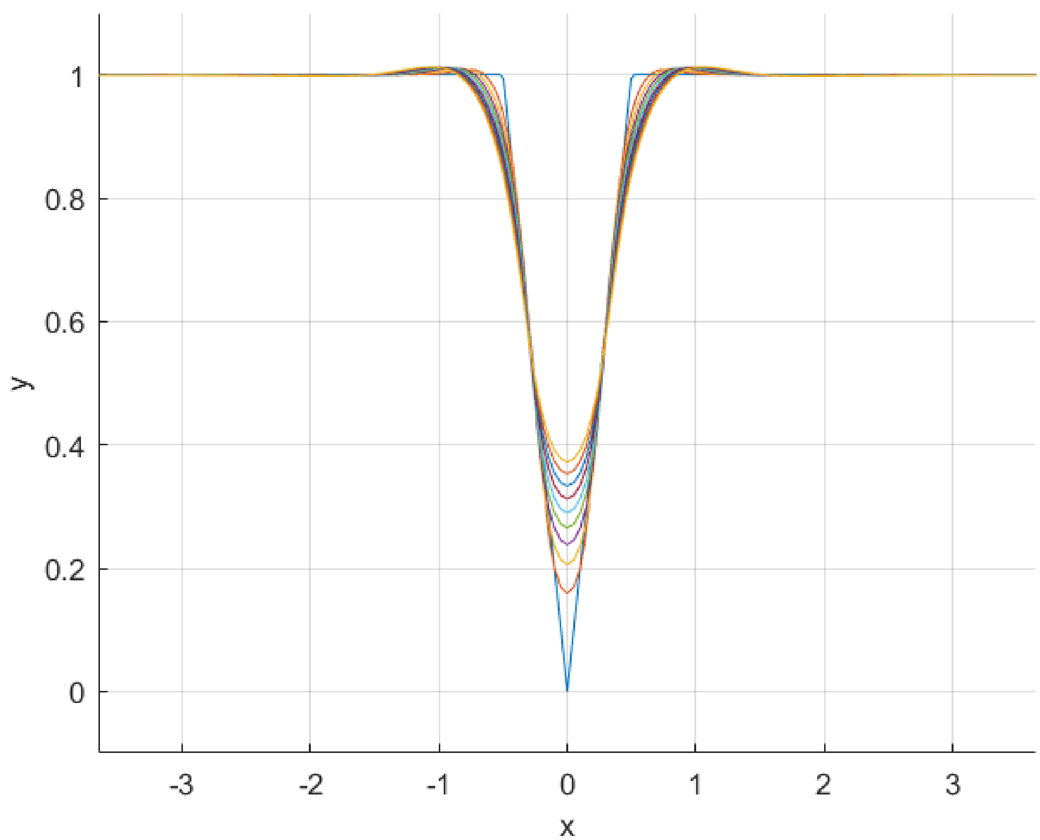

Figure 2.22: This shows the evolution of a triangular crack over time with healing driven solely by surface tension. The dark blue line shows the initial profile of the crack while the other lines show the progression of the healing with time. Here the bond number is taken to be 33.681.

Fig. 2.22 shows the healing profile of a crack with the effect of gravity excluded so that only the surface tension impacts the healing. This allows us to examine the effect of surface tension on crack healing when used in isolation.

For these calculations (2.98) the Green's function used and the surface of the crack ranged between $\hat{x} = -10$ to $\hat{x} = 10$. In this case 1001 equally spaced points were used to represent the surface and a Bond number of $B_o = 33.681$ was used. Time-steps of $\hat{t} = 0.001$ were used to advect the interface with the lines on the graph corresponding to the condition of the surface every 100 time-steps. Here only surface tension was used to drive the surface.

Here it can be seen that the surface tension works to smooth out any corners and reduce the surface area of the crack. This is most visible in the behaviour of the crack near its tip and top corners. The most rapid movement is at the tip of the crack, which fills rapidly. Here the surface tension quickly removes the point then raises the height of the crack, smoothing out the point with highest curvature. At the top corners of the crack ridge like formations are created, with some of the bitumen pushed higher than the initial height of the surface. This is due to the surface tension acting to reduce the curvature in the corners of the system. This displaced bitumen from the tip of the corners has to go somewhere causing the interface to initially expand outwards both to the side of and immediately below the corner, leading to these ridge like formations which reduce the overall surface area of the system.

2.4.5 Behaviours Exhibited in the Crack Healing Experiments

Following on from the results of the computation of the numerical method we now look at examples the behaviours seen in the crack healing experiments carried out as part of this research. These behaviours can then be contrasted with those found from the results of the numerical method.

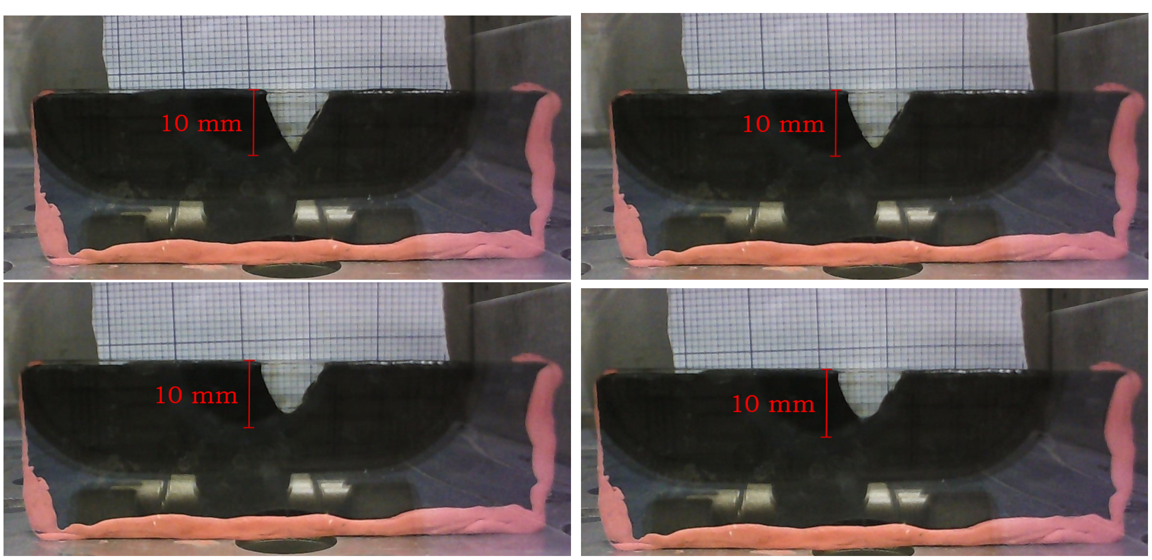

Figure 2.23: The movement of bitumen into a 10 mm tall crack initially 10 mm wide at its highest point. Top left is before heating, top right is after 30 minutes, bottom left is after 60 minutes and bottom right is after 90 minutes.

To give an example of the healing process in the experiments Fig. 2.23 shows four pictures taken at half hour intervals. These images help give an idea of the movement of the bitumen in the Hele-Shaw cell throughout the general course of the experiments and show results which are in line with predictions made by the model.

An example of the full healing profile of one of the cracks from the flow test can be seen in Fig. 2.24. This gives a visual representation of how the cracks healed during the experiments and also shows general agreement with the predicted healing profile from the model.

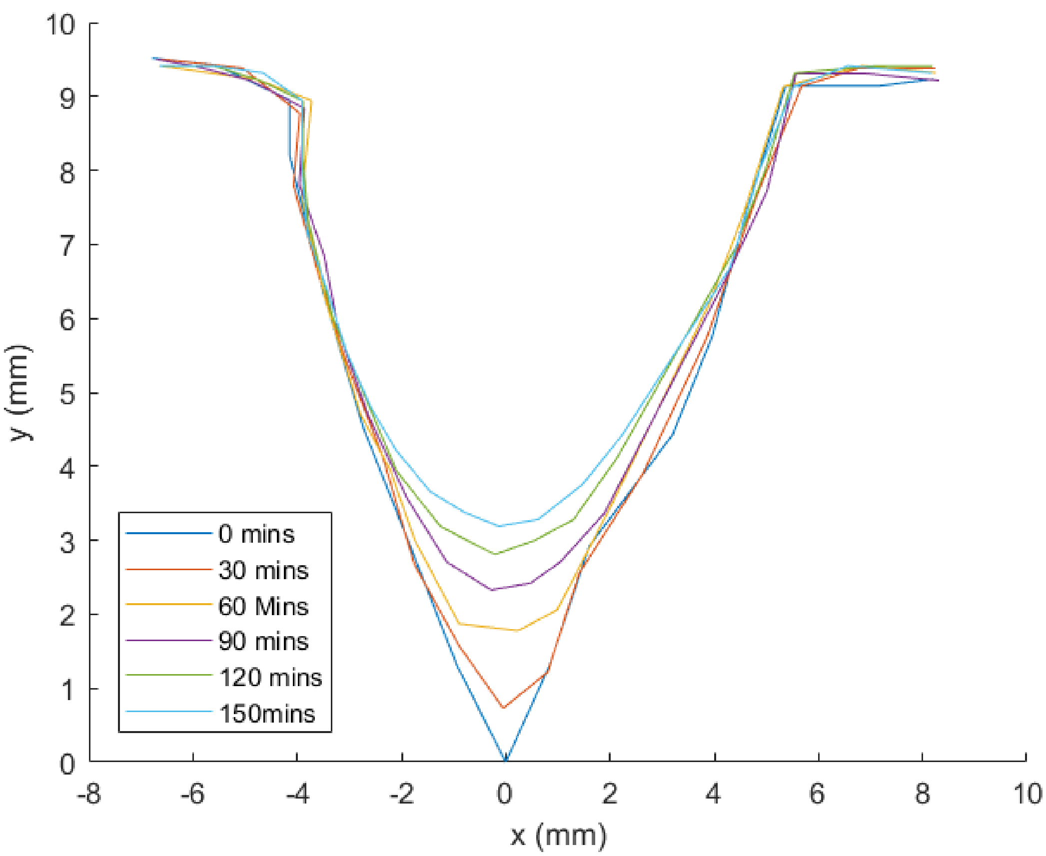

Figure 2.24: This figure shows the healing profile of an example crack from the flow test experiments over time. The coloured lines represent the interface at the times given in the legend.

In these results we see some behaviours which correspond with the results of the numerical method and some which do not. The behaviour seen at the tip of the crack lies broadly in line with the numerical results. Here we see the initial smoothing out of the point of the tip of the crack then with the exception of the first 30 mins of movement a rise of the tip at a decreasing rate. This slower healing than predicted in the first 30 mins of the experiment is likely due to the fact that while the oven had been pre-heated to 40°C the sample started the experiment at room temperature and so while it was at lower temperature the viscosity was higher than the consistent temperature assumed in the numerical results.

In addition to this we see a distinct lack of movement of bitumen at the top corners of the crack this contradicts the behaviour of the numerical results where these corners receded to allow for the flow of bitumen into the crack. This discrepancy is likely due, at least in part, to the assumption that the Hele-Shaw cell would accurately replicate all aspects of a ideal 2 dimensional flow. Throughout this set of the experiments once bitumen was visible at a point on the glass slides it never appeared to recede from that point. This in conjunction with the facts that bitumen does flow into the crack and no extra bitumen is being added to the system leads to the conclusion that while bitumen is flowing away from certain areas a coating of bitumen is left on the glass due to adhesion when it does so. Unfortunately due to the opacity of the bitumen this flow of bitumen close to the centre of the plates isn't possible to measure here.

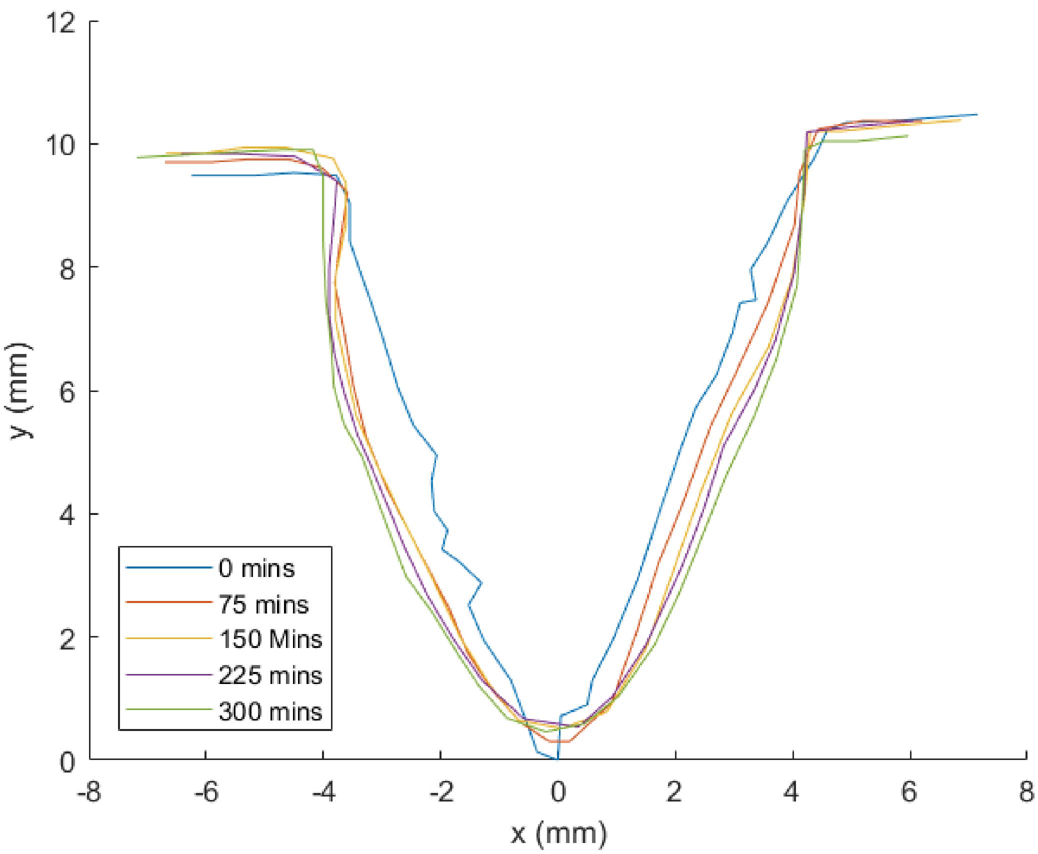

Figure 2.25: This figure shows the healing profile of a submerged crack over time with the lines representing the interface at the times given in the legend.

The effect of submerging a crack in water while it is being healed is to eliminate the impact of gravity on the healing and just see the effect of the surface tension on the interface. An example of the healing profile of one of the experiments performed in this way can be seen in Fig. 2.25. As would expected this differs from the gravity driven healing seen in the main experiments due to the decreased flow of bitumen into the lower section of the crack.

For the surface tension driven healing the immediate result was the heavy smoothing of the crack over the first 75 mins. After this there was comparatively little movement from the crack in the remaining 225 mins that it was monitored. This smoothing of the crack makes intuitive sense given that the driving force here was surface tension which acts to reduce levels of high curvature. Here the experiment only running for 5 hours and displaying a small amount if healing in that time limits useful the comparisons which can be made with the numerical results.

2.4.6 Validation of Healing Rates

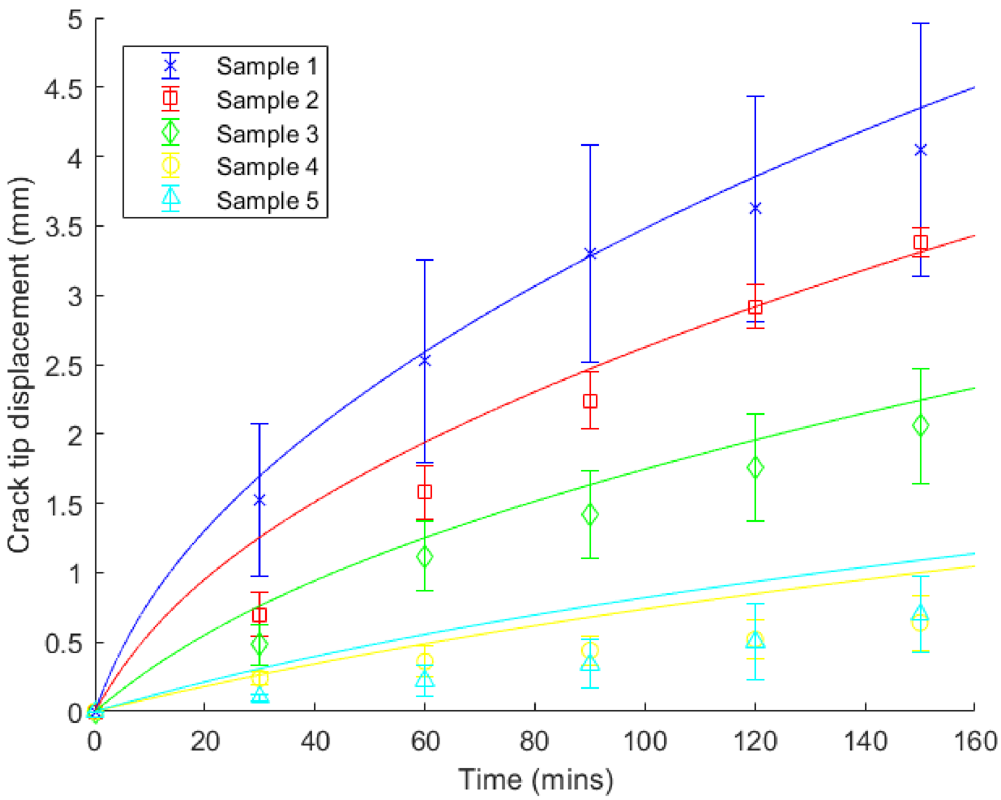

Figure 2.26: This figure shows the how the mean vertical displacement of the tip of the crack changes over time for a 10 mm crack. Each colour shows the average result of five experiments for each class of crack, given by the circles with error bars referring to the standard error. The predictions given by the model for each class of bitumen are given by the lines.

In this section the results of the mean movement of the tip of the crack during the crack healing experiments will be presented and directly compared to the numerical results for the healing of the type of bitumen being used. Here the numerical results were generated using (2.101) as a Green's function bounded at $\hat{x} = \pm 3.65$ and $\hat{y} = -1.3$. 500 points were used to represent the surface and were spread apart with equal distance between them. The surface tension and the dynamic viscosity of the bitumen were taken from Table 2.1 and the density was taken to be 1030 kg/m^3. The calculations progressed in time-steps of $\hat{t} = 0.005$.

Fig. 2.26 shows the average movement of the bitumen over the course of the experiments performed with each type of bitumen plotted against the prediction from the model. Five experiments were implemented for each class of crack for each type of bitumen, the vertical displacement of the tip of the crack was measured every 30 minutes and the average value for each type of was calculated for each time step. Here the width of the crack at its highest point was 10 mm.

As can be seen by Fig. 2.26 the experimental results from the flow test for a 10 mm crack show good consistency with the model, especially for the later times. The lack of consistency between the model and the experimental results at the 30 min mark was likely due to the time taken for the bitumen to heat to the temperature of the oven resulting in a slower than expected initial flow due to the higher viscosity of the bitumen.

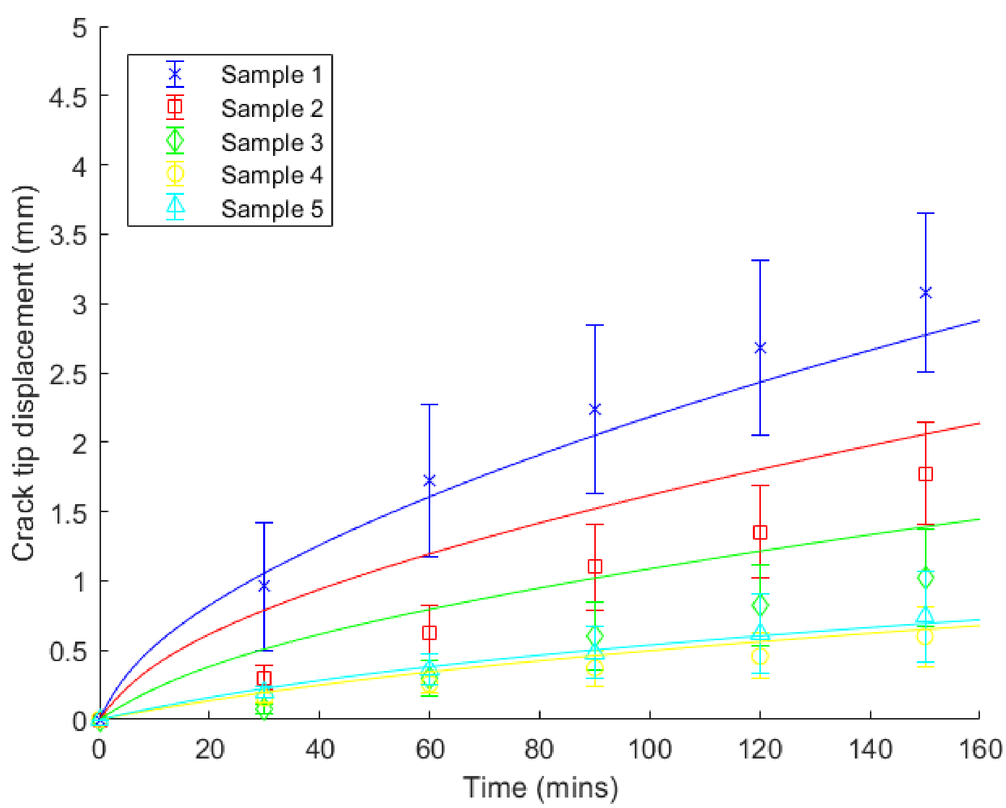

Figure 2.27: This figure shows the how the vertical displacement of the tip of the crack changes over time for the 20 mm crack. Each colour shows the average results of five experiments for each class of bitumen.

The results of the second set of experiments can be seen in Fig. 2.27. These were completed using all five types of bitumen and a crack with maximum width of 20 mm. A total of five experiments were carried out for each of the types of crack and bitumen. During these the vertical displacement of the tip of the crack was measured and the mean value was compared to the predicted value of the model every 30 minutes.

Again for the 20 mm crack the experimental results shows agreement with the model, again with the reliability of results increasing once the bitumen has had time to heat to the temperature of the oven. These results can be seen in Fig. 2.27. This helps to validate the model for when it will be used to model cracks in actual asphalt.

2.4.7 Calibrating an Equation to Predict the Height of a Crack Over Time

The healing rate of asphalt can be directly related to the rate of travel of the tip of the crack in the model. This is due to the fact that the higher the proportion of the crack that has filled with bitumen the harder it will be to break again.

To find an equation to describe the height of a crack over time a variety of cracks were modelled using various surface tensions of bitumen. To begin with the effects of surface tension were looked at in isolation while negating the effects of gravity. This allowed for a complete picture of the impact of surface tension to be assessed before a final equation involving gravity was formed.

Surface Tension (Nm^{-1})	Wide crack		Narrow crack	
	a_{st}	b_{st}	a_{st}	b_{st}
1	1.18	0.492	4.78	0.525
5	4.01	0.493	11.18	0.526
10	5.67	0.494	16.10	0.526
20	7.94	0.493	23.19	0.526
30	9.70	0.493	28.70	0.526
40	11.18	0.493	33.38	0.526
50	12.48	0.493	37.54	0.526
60	13.65	0.493	41.32	0.526
70	14.73	0.493	44.81	0.526
80	15.73	0.493	48.07	0.526
90	16.67	0.493	51.14	0.526
100	17.56	0.493	54.06	0.526

Table 2.2: The values of a_{st} and b_{st} calculated for triangular cracks. The wide crack has maximum width twice as large as its height while the narrow crack has a width the same size of its height. Here the model was run for various surface tensions without taking gravity into effect.

Over the course of months of observing experimental results it was observed that the height of the tip of a crack varies with time with the ratio of the crack being healed consistently increases at an exponentially decreasing rate. Hence an equation to describe the healing of the crack only under surface tension of the form

$$h = 1 - \exp\left(-a_{\mathrm{st}}\left(\hat{t}\right)^{b_{\mathrm{st}}}\right) \tag{2.120}$$

was trialled. Here h is the ratio of the crack which has healed varying between 0 and 1, $h = 1$ when the crack is fully healed and $h = 0$ when the tip of the crack is at it's lowest point. $\hat{t}$ is non-dimensionalised time, a_{st} and b_{st} are values which were determined by an algorithm which minimised the difference between values of h produced directly by the model and those from the equation. To do this the value of h for 10000 time steps of the model was used to generate each result.

The results for two classes of crack were analysed in detail. Firstly a vertical triangular crack was examined with its maximum width of twice its height and secondly another thinner vertical triangular crack was looked at however this one had a maximum width the same size as the height of the crack. The results for both cracks can be found in Table 2.2. As can clearly be seen in the tables the value of b_{st} was independent of surface tension for each type of crack with only very minor variations which can be accounted for by the numerical nature of the model.

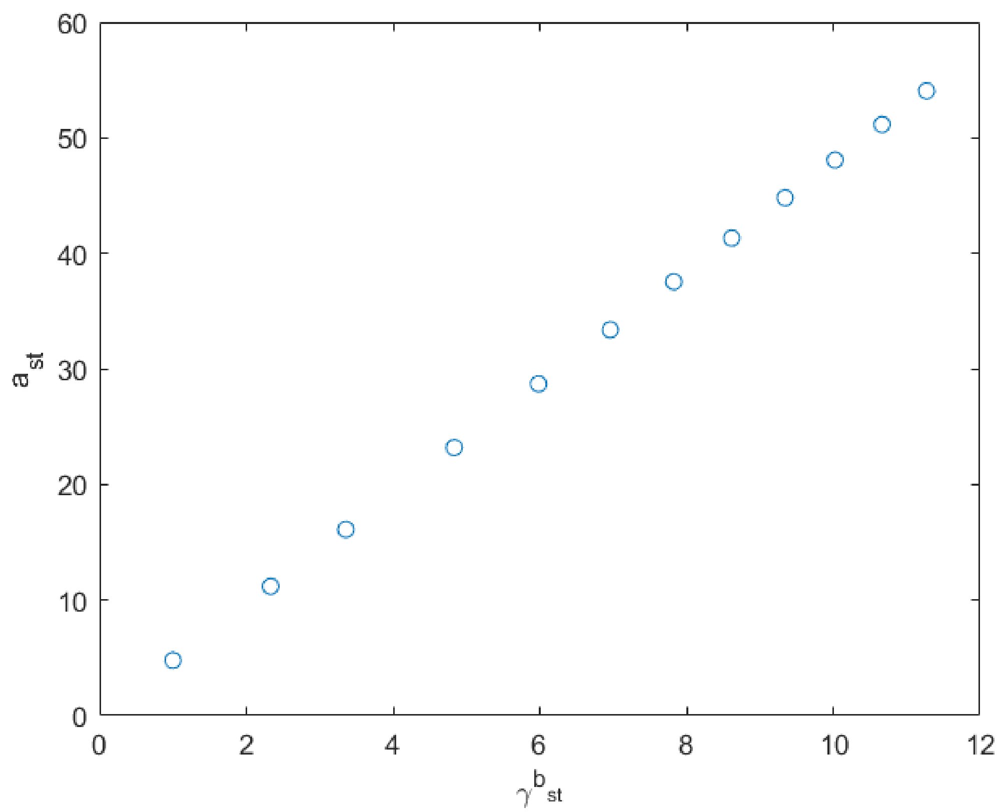

Figure 2.28: The relationship between $\gamma^{b_{\mathrm{st}}}$ and a_{st} for a triangular crack with maximum width twice the size of its height only under the effects of surface tension.

Next the relationship between surface tension and a_{st} was assessed. As can be seen in

Fig. 2.28 and Fig. 2.29 for both classes of crack analysed the value of a_{st} generated varied linearly with $\gamma^{b_{\mathrm{st}}}$. This implies that for surface tension driven healing the relationship between the height of the crack over time and the surface tension, γ, takes the form

$$h = 1 - \exp\left(-\left(a_{\mathrm{st}}\gamma\hat{t}\right)^{b_{\mathrm{st}}}\right), \tag{2.121}$$

where a_{st} and b_{st} are constants determined only by the morphology of the crack.

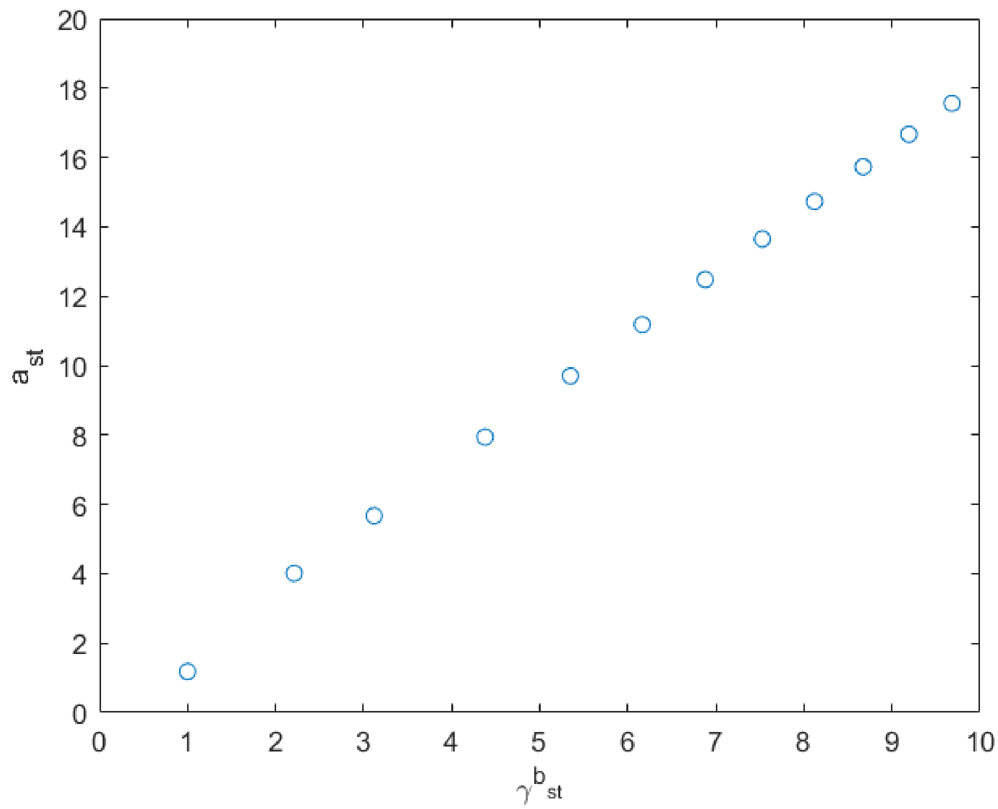

Figure 2.29: The relationship between $\gamma^{b_{\mathrm{st}}}$ and a_{st} for a triangular crack with maximum width the same size as its height only under the effects of surface tension.

Once the connection between surface tension and the healing of the crack was securely established gravity was re-introduced into the model. Again the height of the tip of the crack with time increased at an exponentially decreasing rate so the results from the model were compared to

$$h = 1 - \exp\left(-a\left(\hat{t}\right)^{b}\right), \tag{2.122}$$

were h is the ratio of the crack which was healed and $\hat{t}$ is the non-dimensionalised time. Here a and b are constants which are determined by an algorithm which minimised the difference between the values of h found using the model and those given by the equation. To generate these results 10000 time steps were used to find the appropriate values. The closest values of a and b found for both types of crack are given in Table 2.3.

Surface Tension (Nm^{-1})	Wide crack		Narrow crack	
	a	b	a	b
1	2.38	0.533	5.50	5.40
5	4.32	0.502	11.57	5.29
10	5.89	0.498	16.35	0.527
20	8.11	0.495	23.45	0.527
30	9.88	0.495	28.78	0.526
40	11.30	0.494	33.46	0.526
50	12.61	0.494	37.61	0.526
60	13.79	0.494	41.38	0.526
70	12.61	0.494	44.87	0.526
80	13.79	0.494	48.13	0.526
90	16.71	0.493	51.20	0.526
100	17.72	0.494	54.11	0.526

Table 2.3: The values of a and b calculated for triangular cracks. Here the wide crack has maximum width twice the size of its height while the narrow crack has width the same size of its height. Here the model was run for various surface tensions while taking into account the effect of gravity.

As can be seen by contrasting the results of Tables 2.2 and 2.3 when the effects of gravity are included it has minimal effects on the healing rate when surface tension is high while drastically changing the rate at low surface tensions. Given the precise variation in the generated values of a and b an equation of the form

$$h = 1 - \exp\left(-\left(a_{\mathrm{g}}\hat{t}\right)^{b_{\mathrm{g}}} - \left(a_{\mathrm{st}}\gamma\hat{t}\right)^{b_{\mathrm{st}}}\right) \tag{2.123}$$

would be expected. Here $\hat{t}$ is the non-dimensionalised time and γ is the surface tension. Values of a_{st} and b_{st} are constants related to surface tension driven healing while a_{g} and b_{g} are constants related to gravity driven healing. All of these constants are only dependent on the morphology of the crack in question.

A comparison between the healing ratios over time generated from both (2.121) combined with Table 2.2 and (2.123) combined with Table 2.3 can be found in Fig. 2.30. As can clearly be seen the two versions show good agreement.

Once the non-dimensionalisation of time is reversed these results can be used to produce an equation of the height of the tip of the crack with time for a specified set of experimental parameters. These parameters include crack shape, viscosity of bitumen μ, porosity of the porous medium ϕ, permeability of the porous medium k, the surface tension γ, density of the bitumen ρ and acceleration due to gravity g. The equation takes the form

$$h = 1 - \exp\left(-\left(\frac{a_{\mathrm{g}}\rho g k}{\phi\mu d}t\right)^{b_{\mathrm{g}}} - \left(\frac{a_{\mathrm{st}}\gamma\kappa k}{\phi\mu d^3}t\right)^{b_{\mathrm{st}}}\right). \tag{2.124}$$

Here h is the ratio of the crack which has healed, κ is the curvature of the surface, t is time, d is the height of the crack and a_{g}, a_{st}, b_{g} and b_{st} are constants decided by the

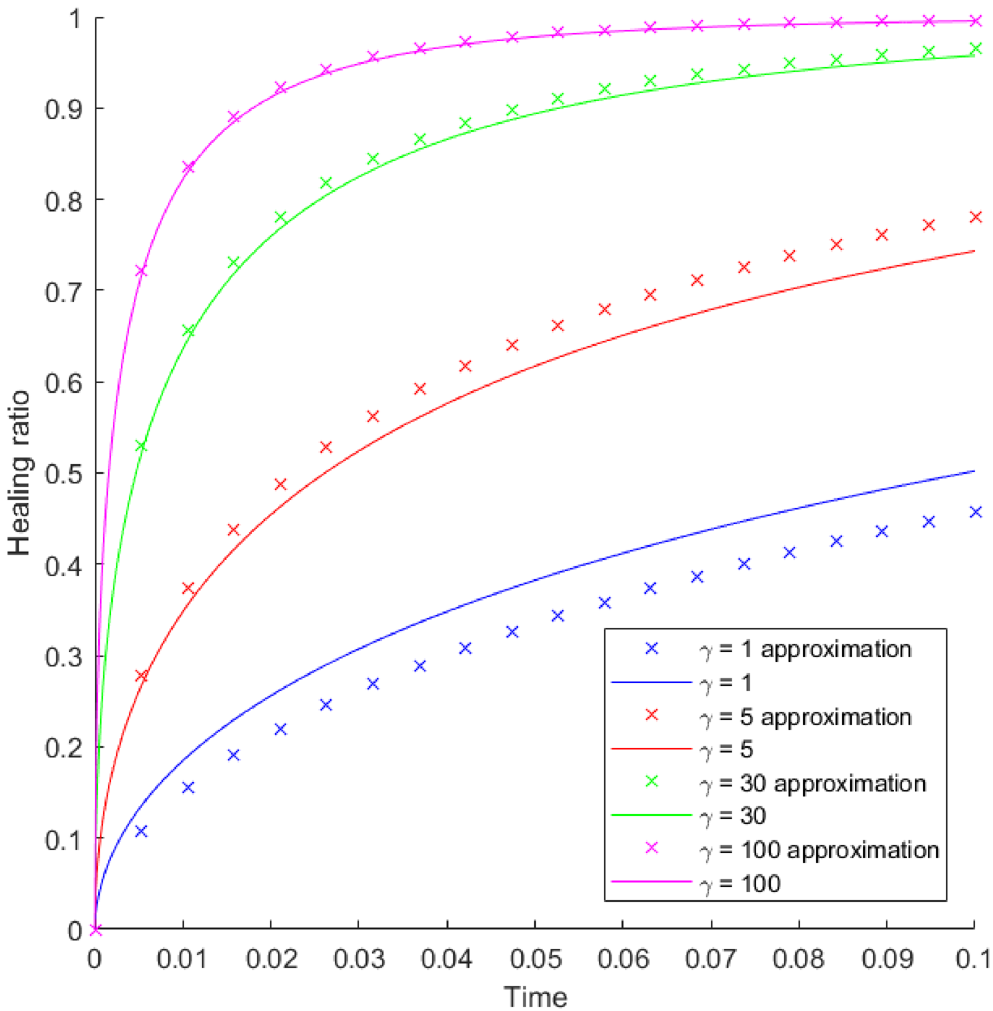

Figure 2.30: A comparison between values of the healing ratio with time for a variety of different surface tensions. Here the lines represent results derived from values of a and b taken from the model results and the crosses show values taken from the results given by (2.123).

morphology of the crack. This equation gives a method of calculating the healing of a crack in asphalt in a form which is computationally cheap to calculate.

As an additional note this equation can also be separated into two distinct parts which isolate the impact of gravity and surface tension on the rate of self-healing. This means that purely gravity driven healing would act in accordance with

$$h = 1 - \exp\left(-\left(\frac{a_{\mathrm{g}}\rho g k}{\phi \mu d} t\right)^{b_{\mathrm{g}}}\right) \tag{2.125}$$

while purely surface tension driven healing would follow the following formula.

$$h = 1 - \exp\left(-\left(\frac{a_{\mathrm{st}}\gamma\kappa k}{\phi\mu d^3}t\right)^{b_{\mathrm{st}}}\right). \tag{2.126}$$

2.5 Summary and Conclusions

This research has discussed the creation of a model to describe the flow of gravity and surface tension driven bitumen. This was used to create an approximate solution to the flow of bitumen into a crack in asphalt. In the model the flow of bitumen was characterised as flow within a porous medium including inside the crack. A small time asymptotic solution was constructed using conformal mapping and a numerical solution using boundary integral methods was used to compute the movement of the fluid interface. In addition laboratory experiments were performed to validate the model experimentally.

Conformal mapping was used to transform a generalised crack into a form which can be modelled using the results from studying an infinitesimally small crack. This allowed the analysis of relatively complicated cracks with a full description of the pressure of the system which in turn was used to compute the small time asymptotic solution to the system.

A numerical solution using boundary integral methods was then computed and verified against analytical solutions for a variety of cases. It was found that in each case as the grid spacing in the simulations tended to zero the error on the pressure gradient also tended to zero.

Next boundary integral methods were used to simulate the movement of the surface of bitumen flowing into different classes of crack. This gave a visual representation of how different types of crack would heal.

In addition a series of experiments which observed the flow of bitumen within a Hele-Shaw cell were performed to validate the model. The experiments gave results consistent with the calculations of the numerical method.

Finally the results of the numerical method were used to calibrate an equation which predicts the gravity and surface tension driven healing level of a crack in asphalt with time. This equation is dependent on the properties of the asphalt, the morphology of the crack and the time healing has been taking place for. This equation can then be taken and used as a computationally cheap method of predicting the healing of a crack in asphalt with time.

Further research in this area could be implemented by the investigation into a variety of factors. Firstly future research in this area could look at extending the model to 3D systems. In addition the field would benefit from looking at the impact of varying the viscosity of the system either temporally or spatially. One final area which could be built upon would be the inclusion of fixed stones in the model to better simulate asphalt.

Chapter 3

Analysis of Three-point Bending Experiments

3.1 Introduction

The previous chapter focused on calculating and validating a numerical solution which could be used to predict the self-healing of a crack over time. Throughout this chapter those results will be used in conjunction with the healing of actual asphalt broken and healed in laboratory experiments to gain further understanding of the self-healing process.

This chapter will begin by relating the equation calibrated at the end of the previous chapter to the healing rate of asphalt. After this the relationship between the proportion of the crack healed and the force required to break a block of asphalt using a three-point bending test will be analysed. This will later allow comparison between predictions from the model and experimental results.

After this three-point bending tests will be performed on asphalt containing a large amount of oil capsules and curve fitting will be used on the results to calibrate a simple equation to predict healing rates. In addition it will give insight into the impact of large quantities of oil capsules on asphalt healing.

These samples of asphalt will also be used to conduct a skid test to ensure that drastically increasing the quantity of oil capsules in asphalt doesn't make asphalt unsafe for common use.

Finally the chapter will analyse the results of self-healing experiments performed in the literature. Here curve fitting will again be used on the results to calibrate a computationally cheap equation to predict healing over time for that class of self healing. Throughout this a variety of classes of asphalt and healing methods will be looked at. The methods to be analysed include induction heating, infra-red heating and preemptively embedding oil capsules in the asphalt during the mixing process to accelerate healing. This will give further insight into the mechanics of the self-healing process when accelerated by different factors.

3.2 Theory

3.2.1 Modelling Assumptions

Throughout this section the previously derived model will be used to make predictions about the self-healing process in cracks in actual asphalt. Due to research performed in [García, 2012] the assumption will be made that gravity is the main driving force in the self healing process. This assumption is also backed by another CT scan in [Gómez-Meijide et al., 2016]. Fig. 3.1 clearly shows that while some initial healing takes place around contact points in the asphalt, over time gravity driven healing plays the dominant role. Given this, according to work done in the previous chapter

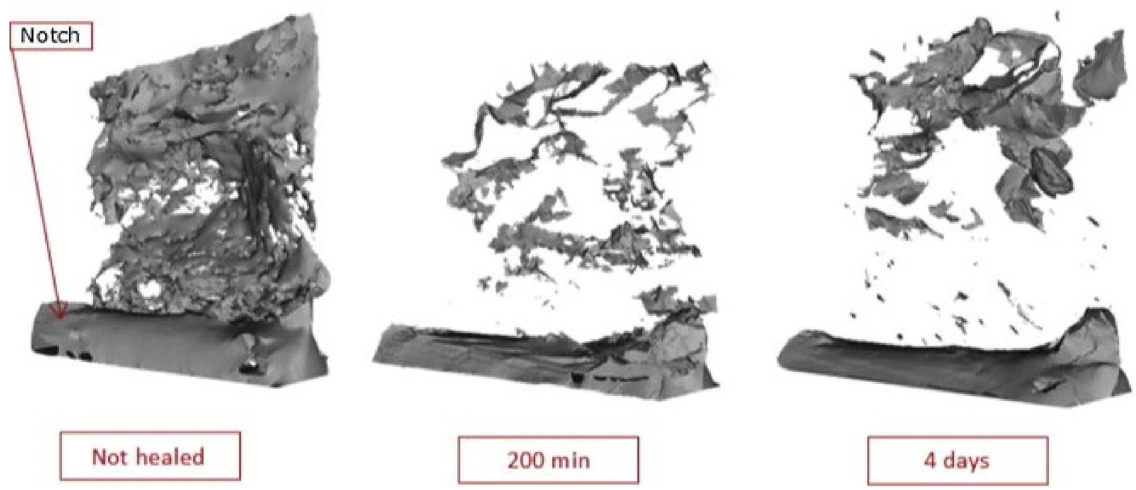

Figure 3.1: A CT scan of a crack being healed conducted by [Gómez-Meijide et al., 2016].

$$h = 1 - \exp\left(-\left(\frac{a_{\mathrm{g}}\rho g k}{\phi\mu d}t\right)^{b_{\mathrm{g}}}\right) \tag{3.1}$$

can be used to give an accurate description of how the crack heals over time t. Here ρ is the density of the bitumen, ϕ is the porosity of the asphalt, μ is the viscosity of the bitumen, g is acceleration due to gravity, k is the permeability of the asphalt, d is the height of the crack and a_{g} and b_{g} are constants dependent only on the morphology of the crack.

For ease of understanding this equation can be simplified to

$$h = 1 - \exp\left(-\left(A_{\mathrm{g}}t\right)^{b_{\mathrm{g}}}\right), \tag{3.2}$$

where

$$A_{\mathrm{g}} = \frac{a_{\mathrm{g}}\rho g k}{\phi\mu d}. \tag{3.3}$$

Doing this simplifies the remaining maths needed to analyse experiments from the literature.

3.2.2 Linking Healing Ratio to the Force Required to Break a Block of Asphalt

Later in this chapter three point bending experiments will be used to break a block of asphalt which will be left to heal and broken again. To gain more insight into the progress of healing during the experiments the maximum force required to break a partially healed block of asphalt must be linked to the height of the tip of the crack at any general point in the healing process. This is an essential step as it leads to the results of three point bending experiments being used to calibrate a computationally cheap equation which can be used to predict the healing of asphalt with time.

This can be done [García, 2012] using

$$M_{\mathrm{F}} = \frac{FL}{4} \tag{3.4}$$

and [Gere and Goodno, 2012, Barber, 2012, Jolicoeur, 2013]

$$\sigma\left(t\right) = \frac{M_{\mathrm{F}} H}{2I\left(t\right)}. \tag{3.5}$$

Here M_{F} is the moment arm, F is the force on the sample, t is the time the beam has been healing for, L is the distance between the two supports used in the three point bending test, σ is the maximum tension the beam can withstand at time t, H is the height of the sample and $I\left(t\right)$ is the 2^{nd} moment of area.

After rearranging this leads to the result

$$F\left(t\right) = \frac{8\sigma_{\mathrm{u}} I\left(t\right)}{LH}. \tag{3.6}$$

Here σ_{u} is the ultimate resisting strength of the beam. This relationship can be investigated in more detail by using the definition of the 2^{nd} moment of area [García, 2012]

$$I = \int_A n^2 dA. \tag{3.7}$$

Here n is the perpendicular distance from the axis of the beam to a point in A, the area of resistance of the beam. For an axis at the centroid of the beam running parallel to the supports

$$n = \left| y - \frac{H}{2} \right|, \tag{3.8}$$

where y is the vertical co-ordinate. After substituting this into (3.7) and taking out the effects of the breadth of the beam, b, we have

$$I = b \int_0^{Hh} \left(y - \frac{H}{2} \right)^2 dy. \tag{3.9}$$

Here h is the healing ratio of the crack given in (3.1). After solving the integral, the result

$$I = \frac{bH^3}{12} \left(4h^3 - 6h^2 + 3h \right) \tag{3.10}$$

is obtained. This can be substituted into (3.6) to give the force required to break the sample

$$F = \frac{2b\sigma_{\mathrm{u}}H^2\left(4h^3 - 6h^2 + 3h\right)}{3L}. \tag{3.11}$$

This equation can be used to illustrate how the force required to break a partially healed block of asphalt is dependent on how much the asphalt has healed. Fig. 3.2 gives a visual interpretation of the ratio of the original force that is required to break a block for a given healing ratio. Here we see a plateau in the effect of healing at the mid-point of the healing and rapid healing at the start and end of the healing process.

This behaviour is due to the fact that the force required to break the beam is proportional to the second moment of area which increases more when healing occurs away from the centroid of the beam. As the crack is modelled as healing from the bottom up this means that the healing in the middle of the process which occurs near the centroid of the beam has far less impact on the force required to break the beam than the healing which occurs at the start and end of the process which happen furthest away from the centroid.

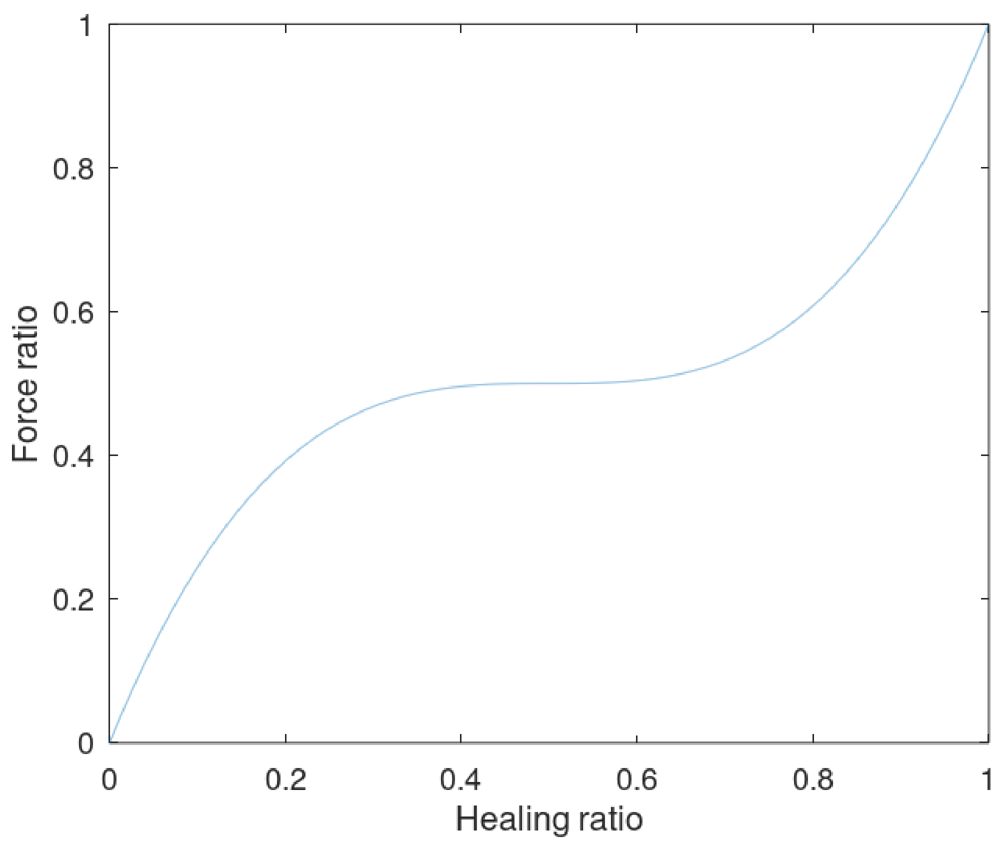

Figure 3.2: For a sample of asphalt which is broken then allowed to heal this represents the proportion of the original force required to break the sample for a second time.

In addition (3.2) can be substituted into (3.11) to directly link the force required to break a block of partially healed asphalt to the properties of the asphalt and the time the block has spent healing. This gives

$$F = \frac{2b\sigma_{\mathrm{u}}H^2\left(4\left(1-\exp\left(-\left(A_{\mathrm{g}}t\right)^{b_{\mathrm{g}}}\right)\right)^3-6\left(1-\exp\left(-\left(A_{\mathrm{g}}t\right)^{b_{\mathrm{g}}}\right)\right)^2+3\left(1-\exp\left(-\left(A_{\mathrm{g}}t\right)^{b_{\mathrm{g}}}\right)\right)\right)}{3L}. \tag{3.12}$$

Throughout the rest of this chapter this equation will be used in conjunction with three-point bending experiments to calibrate values of A_g and b_g for various healing methods and types of asphalt. These values can then be used with (3.2) or (3.12) to predict the healing behaviour of those types of healing methods and asphalt in a computationally cheap way.

3.3 Materials and Methodology

In this section the experiments performed and materials used in the experiments will be detailed. This includes the three-point bending test which was used to find the healing rate of the samples. It will also describe in detail how the oil capsules used in the asphalt were made.

3.3.1 Calcium Alginate Capsules

Oil capsules can be added to asphalt to improve its healing properties. When a capsule cracks it releases the oil inside the capsule into the asphalt to mix with the bitumen. This mixing of the bitumen and the oil softens the bitumen and allows it to flow more easily into cracks in the asphalt. The development of these capsules allows experiments to be conducted on asphalt self-healing without raising the asphalt to high temperatures.

In order to produce the capsules mix 550 ml of water, 50 ml of sunflower oil and 15 g sodium alginate to act as an emulsifier. This is mixed for 15 minutes until an emulsion is formed. Next 600 ml of water and 12 g of calcium carbonate are mixed in a separate beaker until the calcium carbonate completely dissolves. The emulsion is then placed into a burette and added to the calcium carbonate solution dropwise. The calcium carbonate solution is slowly mixed throughout to ensure that the capsules don't collect on a surface. When the drops of alginate emulsion meet the solution the calcium carbonate dissolved in the water reacts with the emulsion to form a hard shell to the capsule while leaving the emulsion inside the shell unchanged. Once the capsules are removed from the water they are placed in an oven at 40°C for three days to dry. After that they are frozen at -20 °C until they are mixed into the asphalt. This freezing prevents the sunflower oil in the capsules from spoiling.

Once produced and dried these capsules had a mean diameter of 2.82 mm with a standard deviation of 0.229.

3.3.2 Asphalt used in this Research

The gradation and design properties of the asphalt used in the experiments performed in this research can be seen in table 3.1. The bitumen used in production was paving grade 40/60 and the aggregate used was Tunstead Limestone. Capsules were also added to the mixture in varying sizes and quantities as well as a control sample with no capsules. Capsules were added in quantities of 0.5% 0.75% 1% 1.25% 1.5% with all percentages being in terms of weight of the total mixture.

The asphalt was mixed at 160°C using the mixer shown in Fig. 3.3 for three minutes with capsules being added in the last 30 seconds of mixing when required. This timing was to reduce capsule breakage during the mixing process while ensuring an even distribution of capsules throughout the asphalt. Prior to this the aggregate had been pre-heated for ten hours and the bitumen for four hours. The capsules were added at room temperature. Once the mixing was complete the mixture was pressed into slabs of dimension 306×306×60 mm using a roller compactor. This process is displayed in Fig. 3.4.

Capsule asphalt 1	
Binder class	40/60
Aggregate gradation (% passing)	
20 mm	100.0
10 mm	81.2
6.3 mm	61.1
4 mm	42.3
2 mm	28.5
0.5 mm	15.0
0.125 mm	9.2
0.063 mm	7.3
Binder content ($\%_{\mathrm{wt}}$)	4.5
Bulk density (kg/m^3)	2384
Air voids (%)	4.5

Table 3.1: A table to display the gradation and design properties of the capsule asphalt 1.

Finally the slabs were cut to beams of dimension 90×140×60 mm. In addition a notch of 10×2 mm was cut along the midpoint of each beam on the 90×140 mm face bisecting the 140 mm length. This was done to introduce a fault to the beam and ensure that it broke in a consistent position during the three-point bending tests later in the chapter.

3.3.3 Asphalt used in Induction and Infra-red Heating Tests

For the experiments performed by [Gómez-Meijide et al., 2016], analysed later in this chapter three distinct styles of asphalt were used. These styles varied in air void content allowing for the investigation of how the increase of air voids in a sample of asphalt impacts the healing process across a variety of methods.

The aggregates used in these experiments were a combination of limestone and metal grit 1 mm in diameter. The volumetric content of metal grit was 4% (11% by weight) and replaced the same volume of limestone of that fraction. The exact gradation of the asphalt can be seen in Fig. 3.5. The binder used was 40/60pen and made up 4.7% of the total mixture.

As previously mentioned what separated the classes of asphalt used here was the air void content. The first class called dense asphalt from this point forwards has 4.5% air void content. The semi-dense asphalt had air void content of 13%. The final class of asphalt used here had 21% air void content and will be referred to as porous asphalt.

All three classes of asphalt were prepared using the same method. First they were mixed for two minutes at 160°C then compacted using a roller compactor to form slabs of 310×310×50 mm. These slabs were then cut to form eight beams of 150×70×50 mm. Again a 2 mm thick and 10 mm deep notch was cut into each block in the 150×70 mm face, bisecting the 150 mm length of the block.

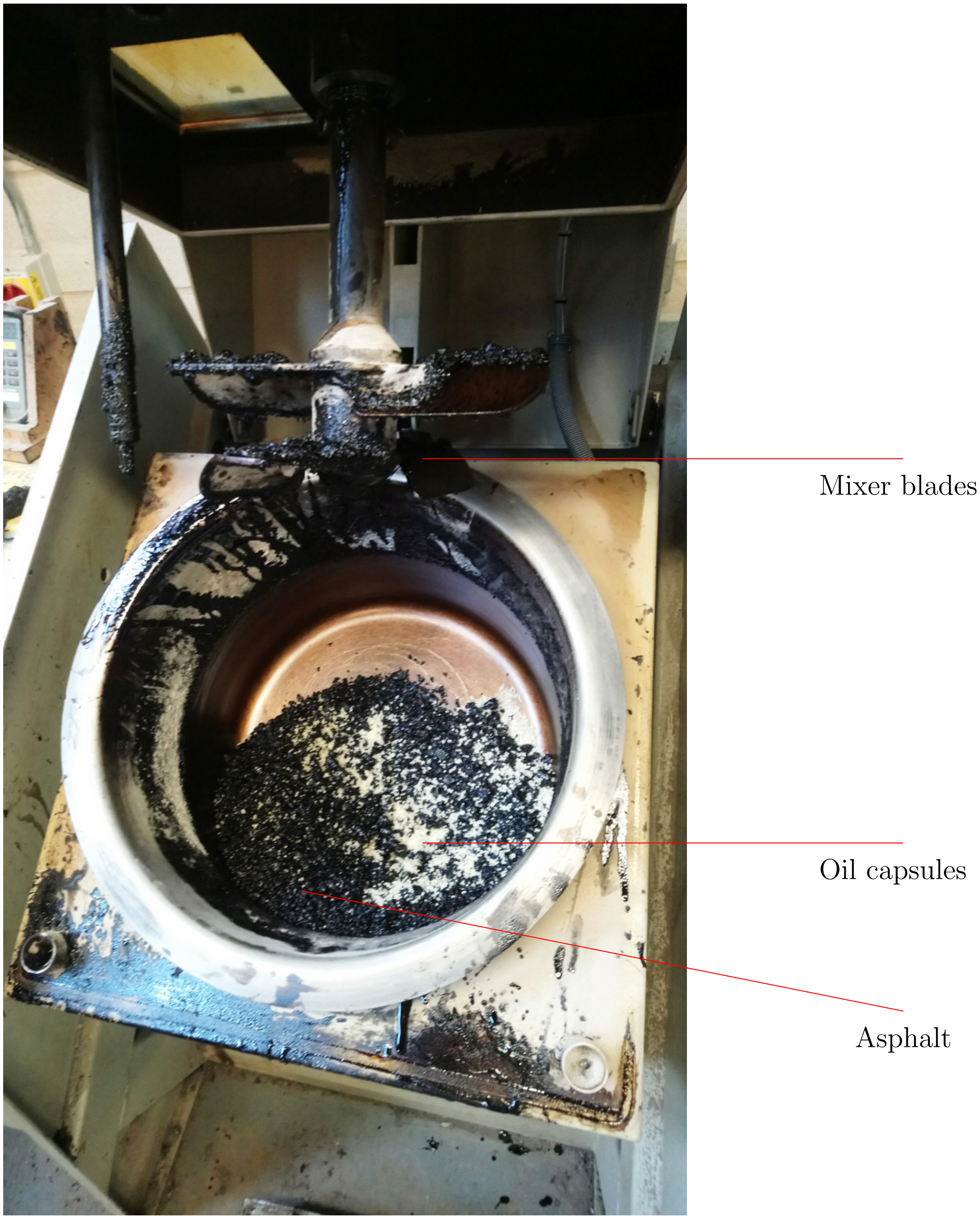

Figure 3.3: The binder, aggregate and oil capsules about to be mixed.

3.3.4 Asphalt used in Capsule Healing tests from the Literature

Throughout this chapter experiments conducted using multiple varieties of asphalt containing oil capsules will be analysed.

The asphalt used in the first and third set of capsule healing experiments, called capsule asphalt 2 from this point forwards, was a dense asphalt mixture AC 20 base (EN 13108-1) made from Tunstead limestone aggregate with density 2.700 g/cm^3. The

Figure 3.4: The slab compression process taking place using a roller compactor. Here the materials that make up the asphalt are being compressed by the machine to form a 306×306×60 mm slab of asphalt.

gradation of this asphalt can be found in table 3.2. During the mixing process capsules were added in quantities of 0.1%, 0.25% and 0.5% by weight with control samples with no capsules also being produced. Sunflower oil was added to the control samples at 0.004% weight of the asphalt during the mixing process to account for the oil released from capsules breaking during mixing.

The asphalt was mixed at 160°C for two minutes with the aggregate and binder being pre-heated for twelve hours and four hours respectively. The capsules were added at the beginning of the mixing process at room temperature. The asphalt was then compacted into slabs measuring 306×306×60 mm using a roller compactor. These slabs were then

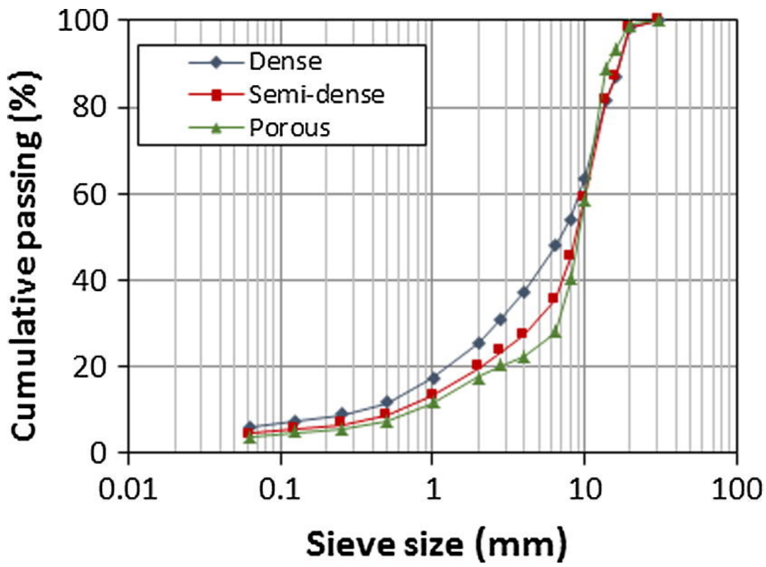

Figure 3.5: The gradation curves of asphalt used in the induction and infra-red healing tests analysed here. Results and graphic taken from [Gómez-Meijide et al., 2016].

Capsule asphalt 2	
Binder class	40/60
Aggregate gradation (% passing)	
20 mm	100.0
10 mm	80.2
6.3 mm	60.3
4 mm	45.3
2 mm	29.7
0.5 mm	15.5
0.125 mm	9.9
0.063 mm	8.0
Binder content ($\%_{\mathrm{wt}}$)	4.5
Bulk density (kg/m^3)	2384
Air voids (%)	4.5

Table 3.2: A table to display the gradation and design properties of the asphalt used in [Al-Mansoori et al., 2018a] and [Al-Mansoori et al., 2018b].

cut to 150×100×60 mm with a 5×5 mm notch cut into the centre of the underside of the beam to facilitate the three-point bending test. This asphalt was used in the experiments conducted in [Al-Mansoori et al., 2018a] and [Al-Mansoori et al., 2018b].

The second class of asphalt used in capsule healing experiments has gradation found in table 3.3. This asphalt will be referred to as capsule asphalt 3 from this point forwards. Here 191.6 g of limestone sand was mixed with 24 g bitumen. Capsules were also added to half the asphalt in a quantity equal 12.1% of the weight of the bitumen.

The oil capsules used in this asphalt differed slightly in composition compared to

Capsule asphalt 3	
Binder class	40/60
Aggregate gradation (% passing)	
2 mm	100.0
0.5 mm	52.2
0.125 mm	33.5
0.063 mm	27.1
Binder content ($\%_{\text{wt}}$)	11.1%

Table 3.3: The gradation of the asphalt mastic used in the second set of experiments analysed in this chapter. From [Al-Mansoori et al., 2017a].

those used across the rest of this research. To produce the initial emulsion required to make the capsules 200 g oil and 400 g water were mixed with 15 g sodium alginate as opposed to the 50 g oil, 400 g water and 15 g sodium alginate used to produce the oil capsules used in this research.

Before the mixing process began the limestone aggregate was pre-heated to 140°C for ten hours while the binder was pre-heated at 170°C for 2 hours. This was mixed by hand before adding the oil capsules at 20°C and mixing for a further 20 seconds. This mixture was then poured into a Teflon™ mould and compacted by hand to produce several beams measuring 30×30×100 mm. These beams had a small triangular notch in the underside of the beam to improve the reliability of the three-point bending test. This asphalt was produced for experiments performed in [Al-Mansoori et al., 2017a].

The next style of asphalt analysed in this research will be a standard dense asphalt mixture AC-13 which from here onwards will be referred to as capsule asphalt 4. The main mixture comprised of basalt gravel of density 2.976 g/cm^3, limestone filler of density 2.996 g/cm^3 and 77.5 pen bitumen. The gradation of the aggregate used here is in table 3.4.

Capsule asphalt 4	
Binder pen	77.5
Aggregate gradation (% passing)	
16 mm	100.0
13.2 mm	96.2
9.5 mm	75.2
4.75 mm	47.4
2.36 mm	30.8
1.18 mm	23.9
0.6 mm	16.6
0.3 mm	12.3
0.15 mm	9.1
0.075 mm	6.9
Binder content ($\%_{\text{wt}}$)	4.7

Table 3.4: The gradation of the asphalt used in [Norambuena-Contreras et al., 2019a].

Prior to the mixing process the bitumen was pre-heated to 160°C for four hours and the aggregate also pre-heated to this temperature but for twelve hours. These were mixed at 160°C with the capsules being added at room temperature in the last 15 seconds of mixing. This was then compressed into slabs of 306×306×60 mm using a roller compactor which were cut to form beams of dimensions 150×100×60 mm. Again a notch was cut into the underside of the beam measuring 5×5 mm bisecting the face. This asphalt was featured in experiments conducted in [Norambuena-Contreras et al., 2019a].

The final style of asphalt analysed here was a stone mastic asphalt which will be referred to as capsule asphalt 5. This was made using Tunstead limestone following the gradation in Fig. 3.6 as well as 40/60 pen bitumen.

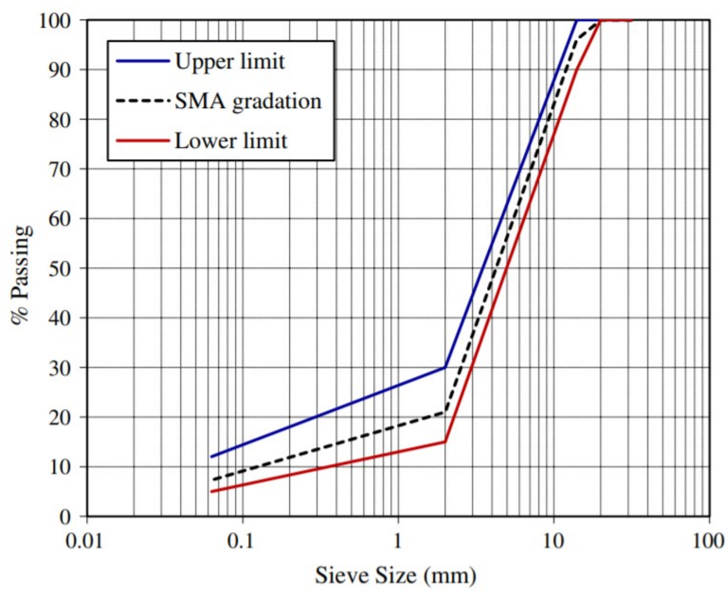

Figure 3.6: The gradation curves of asphalt used in the final set of capsule healing experiments. Experiments and graphic taken from [Norambuena-Contreras et al., 2019b].

To manufacture beams for the three-point bending test the aggregate and binder were both pre-heated at 160°C, the aggregate for twelve hours and the binder for four hours. These were mixed for three minutes at 120°C at 120 rpm. The capsules, kept at 20°C for two hours beforehand, were then added for an additional 20 seconds of mixing to half of the samples. The mixture was then compressed into a slab of dimensions 306×306×60 mm then cut into individual beams of size 150×100×60 mm. these beams had a 5×5 mm notch on the underside along their midpoint.

3.3.5 Three-point Bending Test

A series of three point bending tests were performed on asphalt over a range of healing temperatures and containing varying quantities of capsules. This gave a measure for the progress of the self-healing process in each case.

First each beam was broken in a three point bending test which measured the load required to break the beam. Here the beams experienced a loading speed of 2 mm per minute until they broke. Next the both halves of the beams were placed into a steel mould with a malleable plastic sheet between them to prevent premature healing and compressed at a speed of 2 mm per minute for 2 minutes 30 seconds. This ensured that the capsules would break and release oil into the sample. The plastic sheet was then removed and the two parts of the beam were re-moulded and given time to heal in a temperature controlled cabinet at the appropriate temperature. After the beams had been left to heal the level of healing was assessed by using a three point bending test on the healed beam, again at a loading speed of 2 mm per minute, and comparing the new load required to break the sample to the load which was required to make the initial break.

An image of set-up of the three-point bending test can be seen in Fig. 3.7. As can be seen in the picture a hydraulic rod compresses the sample. A combination of a 1 mm notch in the bottom of the sample and a small metal bar placed between the sample and the rod ensures that the sample breaks roughly along it's centre line.

Figure 3.7: An image displaying the set-up of the three-point bending test. Here a hydraulic rod will break the asphalt sample.

3.3.6 Alternative Healing Methods

While the process for breaking the beams in the three-point bending test is consistent across this research and the literature that was analysed the healing rate of the asphalt was accelerated in a variety of ways throughout the experiments performed in the literature.

When induction heating was used to heal the samples a 6 kW induction heating generator was used. The heater ran at a power of 2800 W, a frequency of 248 kHz and a current of 80 A. The distance between the coil and upper side of the healing beams was 20 mm and the beams were heated for a range of times between 15 s and 240 s.

To heal samples with infra-red light samples were first embedded in white sand leaving only the upper surface exposed. This was done to reduce radiation leakage from the sides of the beams. During the process 250 W infra-red lamps were set at heights of 30 cm, 70 cm or 11 cm from the surface of the beams for healing times ranging from five minutes to four days.

In the case of both induction and infra-red healing the beams were allowed four hours to cool at room temperature before being frozen at -20°C. They then had the three point bending test performed on them again.

3.3.7 Pendulum Test

To measure the skid resistance of the asphalt a pendulum or skid test was used. This comprised of saturating the surface of a sample of asphalt with water and allowing a pendulum to fall in such a way that the entire width of the rubber slider of the pendulum was in contact with the surface for 124 mm during its travel. For the test a Transport Road Laboratories (TRL) slider with rubber hardness of International Rubber Hardness Degree (IRHD) 55 was used.

The average of five measurements of the maximum height the pendulum reached after coming into contact with the sample was then taken as the pendulum test value.

3.4 Results and Discussion

In this section the results of the experiments detailed in the last section will be given. This will begin with the results of the three point bending tests performed during this research.

The next task this section will tackle is the calibration of the values of A_{g} and b_{g} from (3.12). This will be achieved by curve fitting the equation to results from this research and the literature.

After this the results of the pendulum tests clarifying the safety of using asphalt with large amounts of capsules as a road surface will be presented.

This section will conclude with a discussion of insights gained from the previous steps. It will compare the results from the various methods of healing types, how the type of asphalt used impacts self healing as well as extrapolating the equation for healing in order to question the idea of a maximum healing range which is common in literature.

3.4.1 Results and Analysis of Capsule Induced Healing for High Quantities of Capsules

The results of the three-point bending tests conducted as a part of this research can be seen in Fig. 3.8. This displays the average result of two sets of runs of the experiment for each period of healing and each quantity of capsules used to make up the asphalt being broken.

These results were then used to calibrate the values of A_{g} and b_{g} which best fit a healing profile given by (3.12). This was done by running an algorithm to determine the values of A_{g} and b_{g} which minimised the error term

$$\sqrt{\sum \frac{(F_{\mathrm{Theory}} - F_{\mathrm{Experimental}})^2}{N}}, \tag{3.13}$$

where each $F_{\mathrm{Experimental}}$ is the force required to break the sample at a point in time and each F_{Theory} is the predicted force given by the model at the same point in time. N is the number of points being compared. The results of this analysis can be seen in table 3.5. Throughout the whole of this chapter when values of A_{g} and b_{g} are calibrated it will be done using this method.

Asphalt Type	Capsule %	Temperature (°C)	A_{g}	b_{g}
Capsule asphalt 1	0	20	3.73E-12	0.183
Capsule asphalt 1	0.75	20	0.000396	1.000
Capsule asphalt 1	1	20	0.000170	0.609
Capsule asphalt 1	1.25	20	1.25E-6	0.281
Capsule asphalt 1	1.5	20	6.17E-12	0.126

Table 3.5: The values of A_{g} and b_{g} for the three-point bending experiments performed during this research.

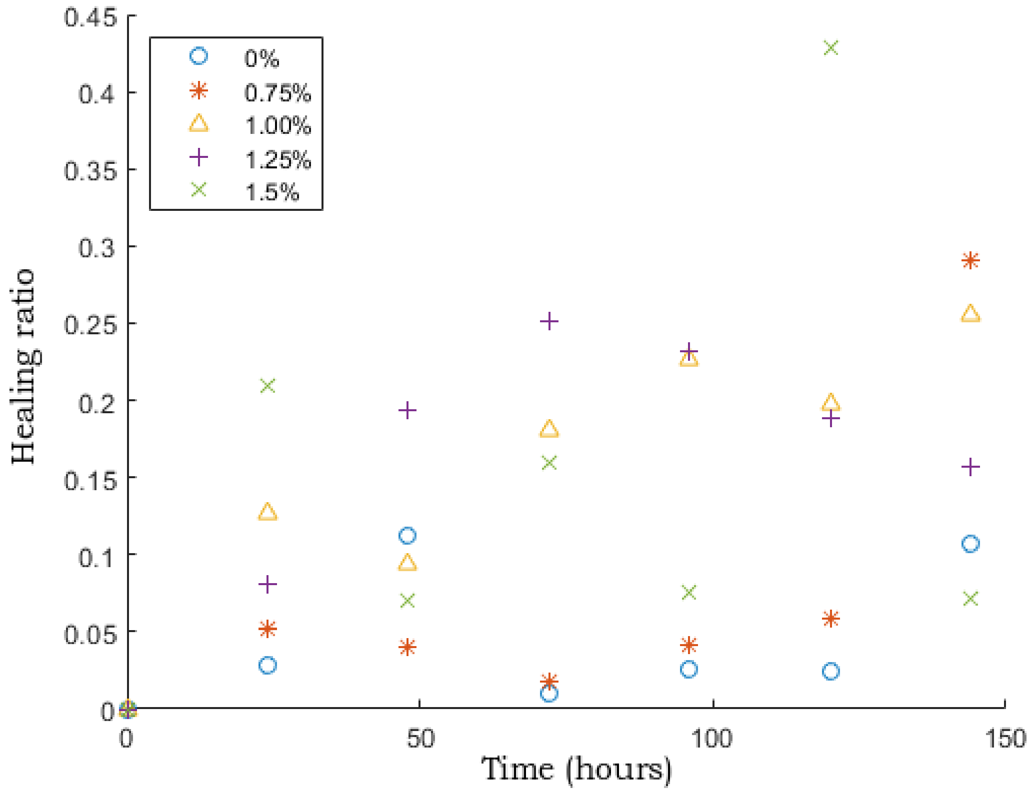

Figure 3.8: The results of the three-point bending tests performed throughout the course of this research.

3.4.2 Analysis of Capsule Induced Healing Results from Literature for Varying Temperatures

In order to compare the effects of altering the temperature on asphalt during the healing process two sets of experiments from the literature were analysed and the healing ratios produced were used to calibrate the experimental value of A_{g} and b_{g} given in (3.12). This was done by finding the values of A_{g} and b_{g} which produced a curve which best fit the experimental results over a range of times by minimising (3.13). An example of one of these curves is given in Fig. 3.9.

The results of the first set of experiments to be analysed were taken from [Al-Mansoori et al., 2018a]. The experiments consisted of performing the three-point bending test at temperatures of -5°C, 5°C, 10°C, 15°C, 20°C, 30°C, 40°C and 50°C. This was performed on both samples with no oil capsules and samples with 0.5 wt.% oil capsule content. The time periods used in the healing process were 6 hrs, 17 hrs, 24 hrs, 48 hrs, 72 hrs, 96 hrs, 120 hrs, 137 hrs, 144 hrs, 168 hrs, 187 hrs and 192 hrs. The test was performed on capsule asphalt 2 and the results can be seen in table 3.6.

The second set of experiments to be evaluated used values from [Al-Mansoori et al., 2017a]. These consisted of performing the three-point bending test at temperatures of

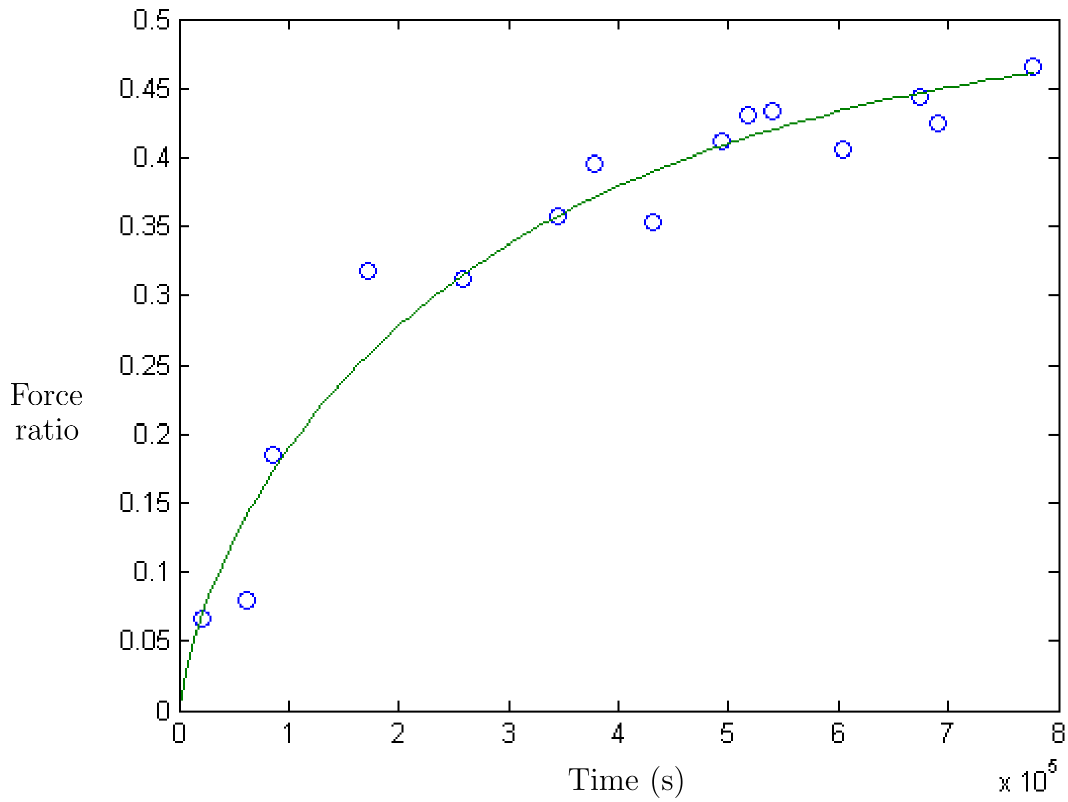

Figure 3.9: Here the healing ratio is compared to the amount of time spent heating the sample. The blue circles represent experimental result while the green curve shows the general trend given by the model. On the y-axis is the ratio of force required to break the healed sample compared to that required to break it originally.

5°C, 10°C, 15°C and 20°C. This was performed on both samples with no oil capsules and samples with 0.5 wt.% oil capsule content. The time periods used in the healing process were 6 hrs, 17 hrs, 24 hrs, 48 hrs, 72 hrs, 96 hrs, 105 hrs, 120 hrs, 137 hrs, 144 hrs, 150 hrs, 168 hrs, 187 hrs, 192 hrs and 216 hrs. The test was performed on capsule asphalt 2 and the results can be seen in table 3.7.

A visual representation of the results of the first two sets of experiments can be found in Fig. 3.10. This graph features a log plot of the results of the calibrated values of A_{g} for both of the first two sets of experiments plotted against temperature. The gradient on the lines of best fit vary from 0.96-4.97

3.4.3 Analysis of Capsule Induced Healing Results from Literature for Varying Quantities of Capsules

Next to examine the impact of altering the amount of capsules contained in the asphalt during the healing process three further sets of experiments were performed and the healing ratios produced were again used to calibrate the experimental value of A_{g} and

Asphalt Type	Capsule %	Temperature (°C)	A_g	b_g
Capsule asphalt 2	0	-5	3.23E-12	0.423
Capsule asphalt 2	0	5	1.16E-7	1.394
Capsule asphalt 2	0	10	1.08E-8	0.691
Capsule asphalt 2	0	15	1.24E-8	0.676
Capsule asphalt 2	0	20	2.68E-9	0.488
Capsule asphalt 2	0	30	9.24E-8	0.602
Capsule asphalt 2	0	40	5.44E-6	0.917
Capsule asphalt 2	0	50	2.00E-5	1.684
Capsule asphalt 2	0.5	-5	4.40E-10	0.471
Capsule asphalt 2	0.5	5	2.16E-7	0.970
Capsule asphalt 2	0.5	10	7.23E-8	0.554
Capsule asphalt 2	0.5	15	1.36E-6	1.141
Capsule asphalt 2	0.5	20	1.73E-6	1.194
Capsule asphalt 2	0.5	30	3.67E-6	0.947
Capsule asphalt 2	0.5	40	1.83E-4	0.231
Capsule asphalt 2	0.5	50	2.10E-5	1.892

Table 3.6: The values of A_g and b_g for the first set of experiments, each was calibrated using the experimental healing ratios at twelve different times ranging from six to 192 hours of healing. The results analysed were taken from [Al-Mansoori et al., 2018a].

Asphalt Type	Capsule %	Temperature (°C)	A_g	b_g
Capsule asphalt 3	0	5	1.21E-9	0.310
Capsule asphalt 3	0	10	7.70E-8	0.554
Capsule asphalt 3	0	15	2.88E-7	0.725
Capsule asphalt 3	0	20	1.34E-6	1.067
Capsule asphalt 3	0.5	5	1.53E-6	1.214
Capsule asphalt 3	0.5	10	2.25E-6	1.183
Capsule asphalt 3	0.5	15	4.32E-6	1.172
Capsule asphalt 3	0.5	20	5.58E-6	1.009

Table 3.7: The values of A_g and a_g for the second set of experiments, each was calculated using the experimental healing ratios at fifteen different times ranging from six to 216 hours of healing. The experiments evaluated here can be found in [Al-Mansoori et al., 2017a].

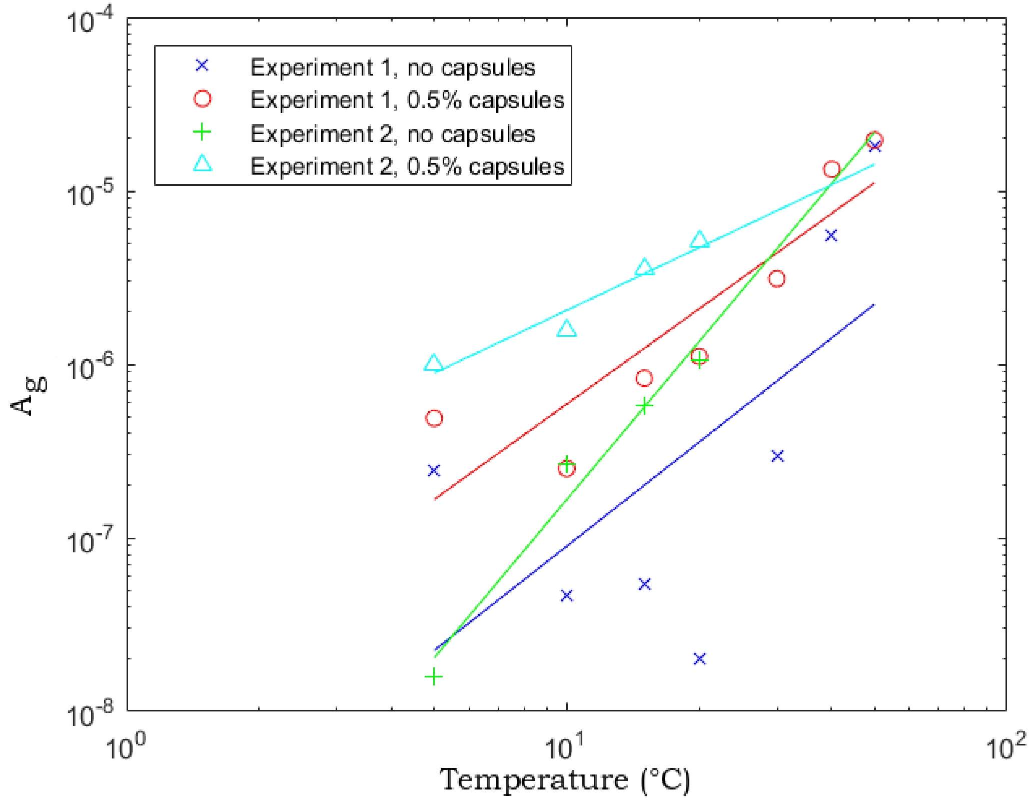

Figure 3.10: A comparison of experiments which varied temperature across a range of values. Here the calculated value of A_{g} is plotted against the temperature.

b_{g} given in (3.12). This was performed by minimising (3.13) to find the values of A_{g} and b_{g} which produced a curve which best fit the experimental results over a range of times.

The first set of experiments which varied capsule quantity were analysed used results generated in [Al-Mansoori et al., 2018b]. During these experiments the three-point bending test was performed at a temperature of 20°C. This used both samples with no oil capsules and samples with 0.1 wt.%, 0.25 wt.% and 0.5 wt.% oil capsule content. The time periods used in the healing process were 6 hrs, 17 hrs, 24 hrs, 48 hrs, 72 hrs, 96 hrs, 120 hrs, 137 hrs, 144 hrs, 168 hrs, 187 hrs and 192 hrs. The test was performed on capsule asphalt 1 and the results can be seen in table 3.8.

The second set of experiments relating to capsule quantity used data from [Norambuena-Contreras et al., 2019a]. Here the three-point bending test at a temperature of 20°C. This was performed on both samples with no oil capsules and samples with 0.5 wt.%, 0.75 wt.% and 1.0 wt.% oil capsule content. The time periods used in the healing process were 5 hrs, 24 hrs, 48 hrs, 72 hrs, 96 hrs, 120 hrs, 144 hrs, 168 hrs, 192 hrs and 216 hrs. The test was performed on capsule asphalt 4 and the results can be seen in table 3.9.

The final set of experiments to be analysed in this section were taken from [Norambuena-Contreras et al., 2019b]. During these experiments the three-point bending test was used

Asphalt Type	Capsule %	Temperature (°C)	A_g	b_g
Capsule asphalt 2	0	20	2.68E-9	0.488
Capsule asphalt 2	0.1	20	2.33E-8	0.664
Capsule asphalt 2	0.25	20	1.79E-7	0.619
Capsule asphalt 2	0.5	20	1.73E-6	0.488

Table 3.8: The values of A_g and b_g for the third set of experiments, each was calibrated using the experimental healing ratios at twelve different times ranging from six to 192 hours of healing. The values of A_g and b_g were generated using experimental results taken from [Al-Mansoori et al., 2018b].

Asphalt Type	Capsule %	Temperature (°C)	A_g	b_g
Capsule asphalt 4	0	20	2.46E-11	0.225
Capsule asphalt 4	0.5	20	7.14E-7	0.695
Capsule asphalt 4	0.75	20	1.58E-6	0.876
Capsule asphalt 4	1	20	1.74E-6	0.769

Table 3.9: The values of A_g and b_g for the fourth set of experiments, each was calibrated using the experimental healing ratios at ten different times ranging from five to 216 hours of healing. The experiments that this set of analysis was performed on are seen in [Norambuena-Contreras et al., 2019a].

at a temperature of 20°C. This was performed on both samples with no oil capsules and samples with 0.5 wt.% oil capsule content. The time periods used in the healing process were 5 hrs, 24 hrs, 48 hrs, 72 hrs, 96 hrs, 120 hrs, 144 hrs, 168 hrs, 192 hrs and 216 hrs. The test was performed on capsule asphalt 5 and the results can be seen in table 3.10.

Asphalt Type	Capsule %	Temperature (°C)	A_g	b_g
Capsule asphalt 5	0	20	3.61E-7	0.704
Capsule asphalt 5	0.5	20	2.36E-6	0.553

Table 3.10: The values of A_g and b_g for the fifth set of experiments, each was calibrated using the experimental healing ratios at ten different times ranging from five to 216 hours of healing. These were found by analysing the results of experiments from [Norambuena-Contreras et al., 2019b].

A visual representation of the results of the last three sets of experiments can be found in Fig. 3.11. This graph features a plot of the results of the derived values of A_g for both of the first two sets of experiments plotted against the amount of capsules in the samples being healed.

Fig. 3.12 displays a p-p plot of the values of b_g across all of the sets of capsule healing experiments against the normal distribution. b_g has a p-value of 0.1772 for the Anderson Darling test showing no significant deviation from the normal distribution. This fits with the initial hypothesis of b_g being only dependent on the morphology of the crack in question and not otherwise dependent on the properties of the asphalt being healed.

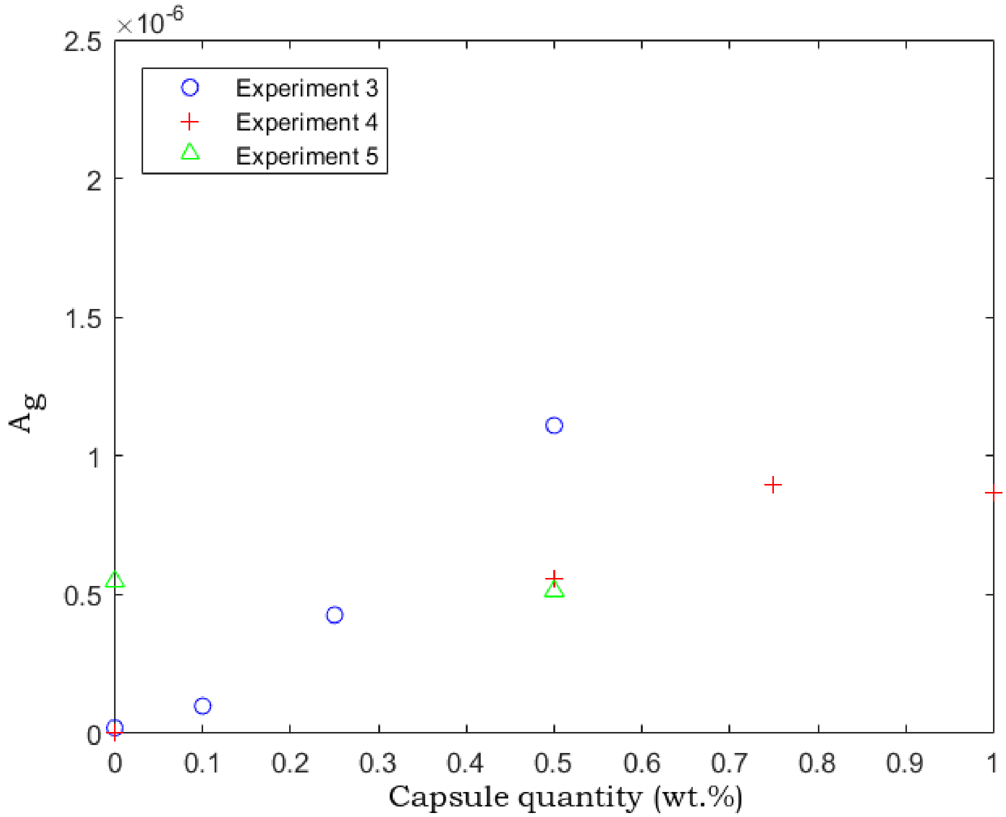

Figure 3.11: A comparison of experiments which varied capsule percentage across a range of values. Here the calibrated value of A_{g} is plotted against the percentage weight of capsules the asphalt consisted of. All experiments here were performed at 20°C.

3.4.4 Analysis of Infra-Red Heating Induced Healing Results from Literature

Here the analysis of the three-point bending tests performed in [Gómez-Meijide et al., 2016] will be conducted. The values of A_{g} and b_{g} will be found which best fit the healing profile for the results by minimising (3.13).

These experiments were conducted on three types of asphalt with various quantities of air voids. These were dense asphalt, semi-dense asphalt and porous asphalt. During the experiments samples were heated for a large selection of times ranging from 5 to 5760 minutes. Table 3.11 gives a full list of the values of A_{g} and b_{g} derived from these results.

3.4.5 Analysis of Induction Heating Induced Healing Results from Literature

The final set of experiments to be analysed are those in [Gómez-Meijide et al., 2016] which feature three-point bending experiments with healing driven by induction heating.

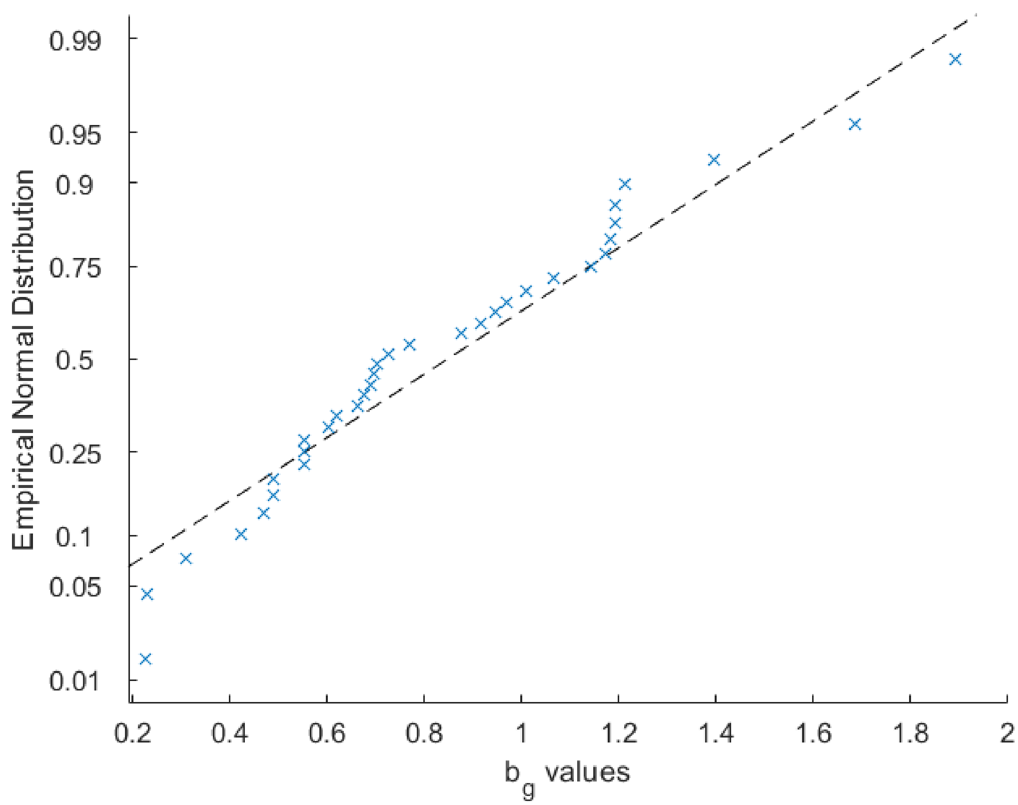

Figure 3.12: A p-p plot comparing the values of b_g to a normal distribution. The dotted line is a reference line for the normal distribution.

Here tests were performed on dense asphalt, semi-dense asphalt and porous asphalt beams.

During these experiments heating times ranged from 15 to 180 seconds and the results were analysed to calibrate the values of A_g and b_g which fit best. This was done by fitting a curve which minimised (3.13). Table 3.12 displays the results of the initial analysis.

Interestingly values of b_g found in samples warmed through induction heating are significantly higher than those found in any of the other experiments, with each class of asphalt analysed having values of b_g higher than 1. This is significant as it implies that the healing ratio grows exponentially with the time the samples were healed for. While at first this appears to contradict the hypothesis that b_g is solely dependent on crack morphology on closer examination the results appear to highlight a different flaw in the model. The assumption that the properties of the asphalt remain constant during the healing process.

As previously stated

$$A_g = \frac{a_g \rho g k}{\phi \mu d}. \tag{3.14}$$

This means that A_g is dependent on the viscosity of the bitumen in the asphalt which in turn is dependent on the temperature of the bitumen. As the heating took place over

Asphalt Type	Height of Infra-red Heater (cm)	A_g	b_g
Dense Asphalt	30	6.56E-4	0.625
Semi-dense Asphalt	30	9.19E-4	0.697
Porous Asphalt	30	1.81E-4	0.671
Dense Asphalt	70	4.42E-6	0.283
Semi-dense Asphalt	70	4.40E-4	0.495
Porous Asphalt	70	1.50E-4	0.436
Dense Asphalt	110	3.57E-5	0.649
Semi-dense Asphalt	110	7.90E-4	1.179
Porous Asphalt	110	7.37E-4	0.891

Table 3.11: The values of A_g and b_g found by analysing the results of three point bending tests performed in [Gómez-Meijide et al., 2016].

Asphalt Type	A_g	b_g
Dense Asphalt	4.29E-4	3.492
Semi-dense Asphalt	4.13E-4	2.407
Porous Asphalt	7.55E-4	3.163

Table 3.12: The A_g and b_g calibrated from the three-point bending results found in [Gómez-Meijide et al., 2016] featuring the use of induction heating.

such a short period of time (between 15 to 180 seconds) the value of A_g would have increased with the temperature of the sample which, unlike the other healing methods displayed in this chapter, would not have had time to stabilise during the healing. As the value of A_g would have increased over the course of the healing this likely artificially raised the values of b_g found for this set of experiments.

Unfortunately without knowing exactly how the temperature of the samples varied during the course of the healing process and how that in turn impacted the viscosity of the bitumen in the asphalt it becomes very difficult to analyse these experiments any further. This is something compounded by the uneven heat distribution caused by the induction heating, both in the drastic difference in heating of the side of the sample closer to the induction heater and the increases in heat being centred around the metal particles in the road.

3.4.6 Pendulum Test Results

The pendulum test was performed on the capsule asphalt 1 samples used in the three-point bending test both before and after the capsules were broken through further compression of the beams. This was done to check the results fall within safety limits for commercial production of roads even if a greater number of capsules were used than had been seen in previous research. The results of this can be seen in Fig. 3.13 where it can be seen that the Pendulum test values (PTV) fall well above the required PTV of 40 even after compression of the samples, indicating that the surface is safe for use in roads in this respect.

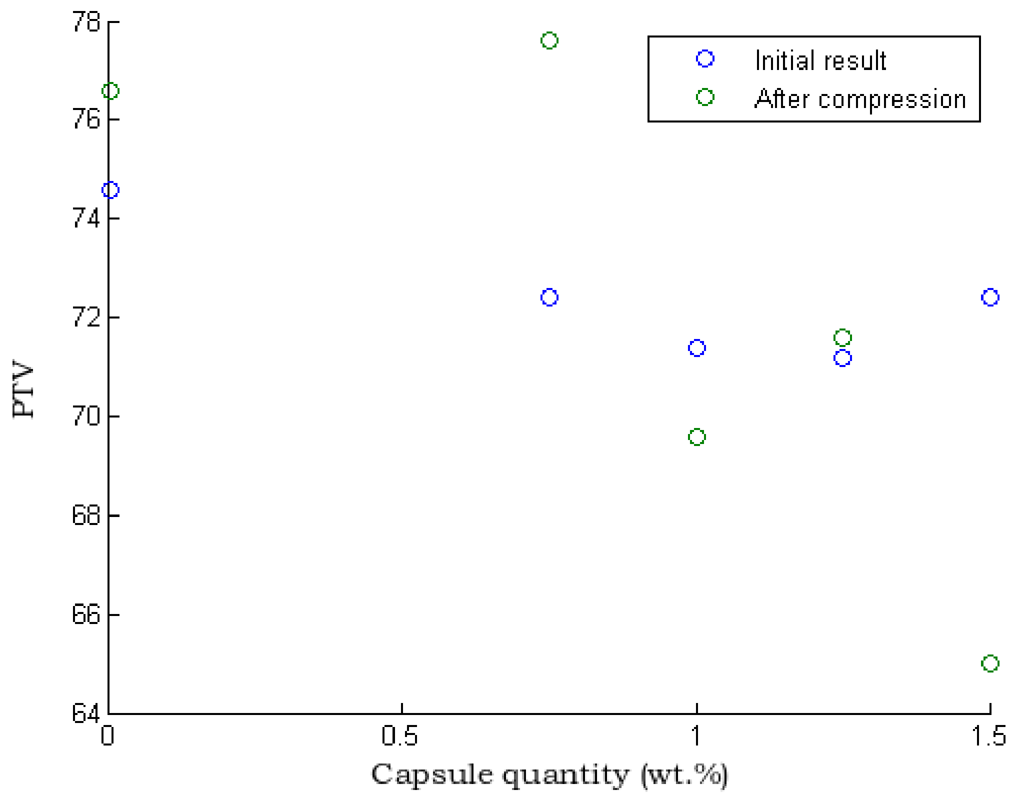

Figure 3.13: Results of pendulum tests on capsule asphalt 1. The initial results are shown in blue and the results after a sample has been broken and compressed are shown in green. The percentage of capsules in a sample is given on the x-axis while the pendulum test value is given on the y-axis.

3.4.7 Air Void Impact on Healing

The results of the experiments analysed here show that increased air voids in asphalt increase the healing potential. When considered side by side the Infra-red heating induced tests are consistent in this. However porous asphalt also required considerably less force to break initially so caution should be taken with this conclusion. While the more dense asphalt was slower to recover a proportion of its original strength it generally still took more force to break than the porous asphalt at any stage of the healing process.

3.4.8 Comparison of Capsule Induced Healing Results

When looking at the results for the capsule induced healing experiments performed as part of this research it shows that asphalt without oil capsules consistently performs worse than asphalt containing any level of oil capsules.

The best performing quantities of oil capsules for healing here were at the 1% and 1.25% range which both showed consistent healing across the entire timespan of the experiments. Samples with an oil capsule quantity of 1.5% also had some impressive results however this was inconsistent.

When comparing these results to those from the literature it becomes apparent that while there is a significant difference between the healing results of samples with and without capsules this difference is not as significant or consistent as results seen elsewhere in the literature.

3.4.9 Considerations of a Maximum Healing Range for Capsule Induced Healing

One point to note is that in the raw data of many of the capsule healing experiments performed in the literature the healing of samples appears to stop very close to the point where 50% of the force required to break samples originally is required to break the healed beams. In fact there was at least one run of experiments in each capsule focused paper which featured this trend. The only research analysed here regarding capsules where this barrier was clearly exceeded for certain conditions took place in [Al-Mansoori et al., 2018a] and [Al-Mansoori et al., 2017a].

In some of the papers [Norambuena-Contreras et al., 2019b, Al-Mansoori et al., 2018a, Norambuena-Contreras et al., 2019a] this was naturally assumed to be a boundary on how much the asphalt was capable of healing under these conditions. However (3.12) would indicate that this is not the case. Due to the difference in 2^{nd} moment of area healing in the centre of the crack has a far smaller effect on the force required to break the sample than healing at the top or bottom of the crack. This is due to the centre of the crack being closer to the centroid of the beam. As such when $b_{\mathrm{g}} \leqslant 1$, which would be the case for the majority of cracks, a natural plateau would occur in the ratio of force required to break the sample originally compared to the force required after healing at the 50% mark. This would be compounded by the tendency of the healing ratio to increase at an exponentially decreasing rate to give the impression of a maximum ceiling for healing when none exists.

To demonstrate this phenomenon an example of a healing profile extrapolated from the results in [Norambuena-Contreras et al., 2019b] can be seen in Fig 3.14 with experimental data points given for reference.

3.4.10 Contrasting Healing Methods

There are several trade offs to consider when deciding between various styles of self healing. In the results analysed here large increases in temperature produce the most impressive healing. Induction is of the three methods by far the fastest to produce results. However asphalt containing capsules heated to 40°C and infra-red healing also managed to consistently produce healing rates over 50% over the course of the experiments. Unheated asphalt containing oil capsules proved to be the slowest of the healing methods however still did produce significant results and has the major advantage over the other methods of not needing any active attention in order to heal.

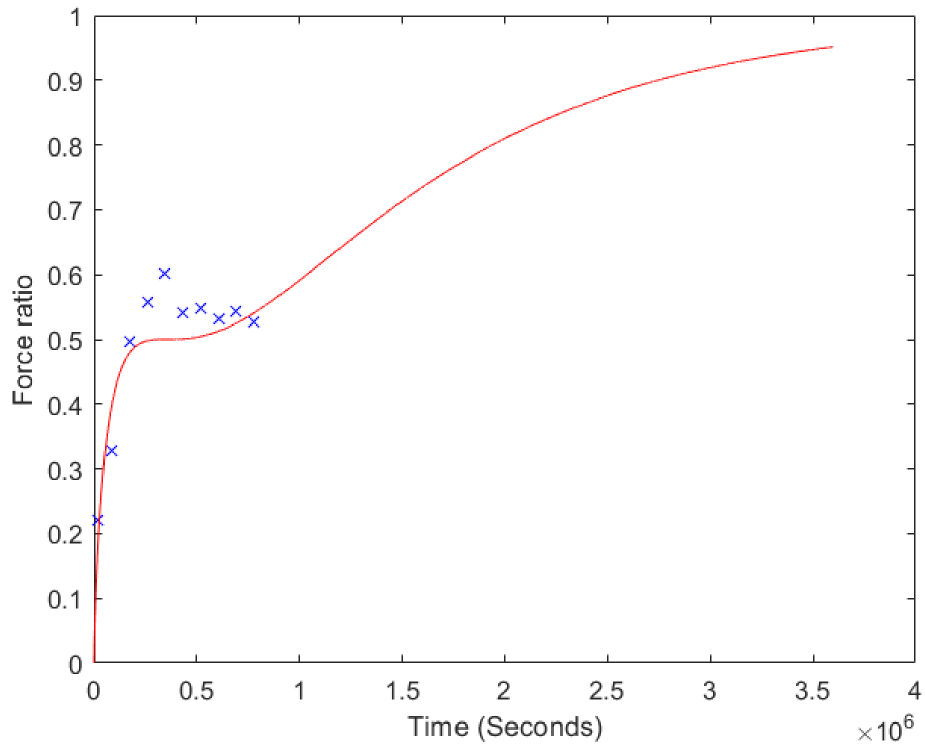

Figure 3.14: An extrapolated healing profile for capsule asphalt 4 with 1% capsule content. The ratio of force required to break the healed sample to force required to break the sample originally is on the y-axis.

3.5 Summary and Conclusions

Throughout this chapter of the thesis the results of the healing of asphalt broken in laboratory conditions has been analysed and compared to the previous chapter.

The first outcome of this chapter was the development of an equation derived from the gravity driven model for the force required to break a beam with time spent healing. The equation is dependent on the physical properties of the system and the morphology of the crack being healed. This gives a better insight into the asphalt self-healing process. Variables in this equation were calibrated for various types of asphalt and healing methods by comparing to results from the literature.

A set of healing experiments were performed on asphalt containing a large number of capsules. While these didn't quite reach the same level of healing results seen by oil capsules used in the literature there was still significantly more healing in asphalt containing oil capsules than in those without. The highest levels of consistent healing were seen by samples comprised of 1% and 1.25% capsules.

A pendulum test was also performed on asphalt containing a large number of capsules to allay fears that the increase in oil capsules would make surfaces constructed from this material unsafe to drive on. These tests confirmed that roads constructed from this material would provide enough friction to fall within safety limits.

In addition a series of experiments studying the healing rates of asphalt have been analysed and show definite positive correlation between the healing rate and temperature as well as between the healing rate and the amount of oil capsules which were contained in the broken samples.

The results of the healing profiles generated here also call into question the assumption that asphalt containing capsules have a maximum healing range. Instead they suggest that this is merely a temporary delay in the increase of the force required to break a beam due to the underlying mechanics of the three-point bending test.

A future possibility for research in this area would be running healing tests on capsule enhanced asphalt for longer periods of time than those previously to test the hypothesis that the perceived maximum healing limit is only a minor delay in the self-healing process. Running tests with a greater variety of capsule quantities to fully explore the effect they have on the self healing process would also be beneficial to our understanding. Finally it would be useful to examine the effects of a non-constant temperature on the healing rate during the self-healing process.

Chapter 4

Slow Gravity and Surface Tension Driven Healing of a Variety of Orientations of Cracks in Asphalt

4.1 Introduction

The focus of the next chapter of the thesis will be on studying the effect of the orientation of cracks in asphalt on the healing rate.

The chapter will begin with outlining the different classes of crack which will be studied over it's course as well as clarifying the differences to the base assumptions of the model which will be required to study different orientations of crack. As with chapter 2 the model will assume that the bitumen flow is driven by surface tension and gravity and the entire domain can be considered to be a porous medium.

After this the chapter will take a look at the exact alterations to the numerical methods used to produce the simulation of a self-healing crack when the orientation of the system is changed. This will ensure a working simulation of a variety of different orientations of crack can be produced.

Finally I will focus on validating the results of the numerical solution for all orientations through a long-running series of experiments. These experiments will measure the flow of bitumen into a series of different cracks with the bitumen contained in a Hele-Shaw cell in order to simulate a porous medium. The comparison of the results of these experiments to the predictions made using the numerical solution will be used to validate the model.

4.2 Theory

Throughout this section the theory behind self-healing in cracks in different orientations will be examined. Firstly the scenario of an inverted vertical crack originating at the base of the asphalt will be studied. Next the situation of a horizontal crack will be looked at and finally the occurrence of multiple vertical cracks in the same piece of asphalt with one appearing at the bottom of the sample and the other stemming from the top will be subject to examination.

To begin with a full mathematical framework will be presented to allow for the intuitive understanding of each of these systems. This framework will establish a model which assumes the movement of bitumen is driven by surface tension and gravity and can be characterised as movement within a porous medium throughout the system including within the cracks. This will allow a solid basis for the rest of the theory examined in the remainder of the chapter.

After this boundary integral methods will be used to give a numerical solution to the pressure gradient at each point on the interface of the system. This information can then be used to compute the movement of the crack over time.

4.2.1 Common Modelling Assumptions

Throughout the chapter a common set of conditions will be used in the modelling of all three classes of crack. The width of all the cracks studied are assumed to be thin relative to the height of the cracks and dimensions of the asphalt as a whole. The asphalt is considered to be a porous medium and as discussed in the second chapter of this research it will be assumed that the fluid flow will still be characterised as flow within a porous medium while the bitumen moves in the area defined by the initial crack.

The domain of the bitumen will vary with the type of crack being examined but will be defined by the Cartesian co-ordinates x and y and will have a velocity field of $\mathbf{u}\,(x, y, t)$ and pressure field of $p = (x, y, t)$. Here t represents time.

The substitution $\bar{p} = p + \rho g\,(y - h)$ will be used to make a modified pressure field $\bar{p}$ and simplify a large quantity of the following equations. Here p is the pressure at a point in the system, h is the initial vertical distance between the top of the asphalt and the origin, ρ is the density of the bitumen and g is acceleration due to gravity.

In addition, to simplify the mathematics involved the same non-dimensional scaling as the second chapter will be used with length, pressure, time and velocity being scaled with d, $\rho g d$, $\frac{\phi \mu d}{\rho g k}$ and $\frac{\rho g k}{\phi \mu}$ respectively. Here d is the height of the crack, ϕ is the porosity of the medium, k is the permeability of the asphalt and μ is the kinematic viscosity of the bitumen. The dimensionless variables which come from this non-dimensionalisation are $\hat{x} = \frac{x}{d}$, $\hat{y} = \frac{y}{d}$, $\hat{p} = \frac{\bar{p}}{\rho g d}$, $\hat{t} = t\frac{\rho g k}{\phi \mu d}$, $\hat{\mathbf{u}} = \mathbf{u}\frac{\phi \mu}{\rho g k}$ and $\hat{\kappa} = d\kappa$. Here κ is the curvature of the surface.

Given this, for $\hat{t} \geqslant 0$ and in the domain of the bitumen Darcy's law applies to the bitumen and can be expressed as [Prada and Civan, 1999, Shikhmurzaev and Sprittles, 2012]

$$\hat{\mathbf{u}} = -\nabla \hat{p}. \tag{4.1}$$

The conservation of mass condition also applies and is given by [Valdés-Parada et al., 2013, Kaasschieter, 1999]

$$\Delta \hat{p} = 0. \tag{4.2}$$

On the surface of the fluid the stress jump condition [Minale, 2014, Duchesne et al., 2019] can be written in terms of the normal part

$$\hat{p} = \frac{\hat{\kappa}}{Bo} + (\hat{y} - 1) + \delta \hat{\mathbf{n}} \cdot \hat{\mathbf{e}} \cdot \hat{\mathbf{n}} \tag{4.3}$$

and the tangential part

$$\delta \hat{\mathbf{n}} \cdot \hat{\mathbf{e}} \cdot \hat{\mathbf{t}} = 0 \tag{4.4}$$

when expressed in the dimensionless variables. Here $\hat{\mathbf{n}}$ and $\hat{\mathbf{t}}$ are respectively the normal and tangential vectors to the surface of the bitumen while $\hat{\mathbf{e}}$ is the rate of strain tensor which is expressed by

$$\hat{\mathbf{e}} = \frac{1}{2} \left(\nabla \hat{\mathbf{u}} + (\nabla \hat{\mathbf{u}})^T \right). \tag{4.5}$$

The Bond number, Bo, is given by the equation

$$Bo = \frac{\rho g d^2}{\gamma}, \tag{4.6}$$

where γ is the surface tension of the bitumen. The dimensionless parameter δ can be expressed as

$$\delta = \frac{k}{\phi d^2}. \tag{4.7}$$

As discussed in the second chapter of this research it is assumed that $\delta \ll 1$ meaning that at leading order (4.3) reduces to

$$\hat{p} = \frac{\hat{\kappa}}{Bo} + \hat{y} - 1. \tag{4.8}$$

From this point on the boundary conditions for each class of crack diverge and so will be investigated separately in the following sections.

4.2.2 Modelling an Inverted Crack

The inverted crack will be the first class of crack to be investigated. In this situation a thin vertical crack of height d has formed at the bottom of a piece of asphalt at a depth h from the surface. A schema of this style of crack with the original variables is in Fig. 4.1. In the figure the original values of variables are used as opposed to their non-dimensionalised variants to give a clearer view of the physical system being modelled.

Two different domains of this crack will be analysed in this chapter. Firstly the semi-infinite case will be looked at for a better representation of healing in asphalt. Here h will be assumed infinite and the model extends infinitely in the $\pm\hat{x}$ directions.

In this case the boundary conditions are

$$\hat{\mathbf{u}} \to 0, \;\; \hat{p} \to 0, \;\; \text{as } \hat{y} \to \infty, \tag{4.9}$$

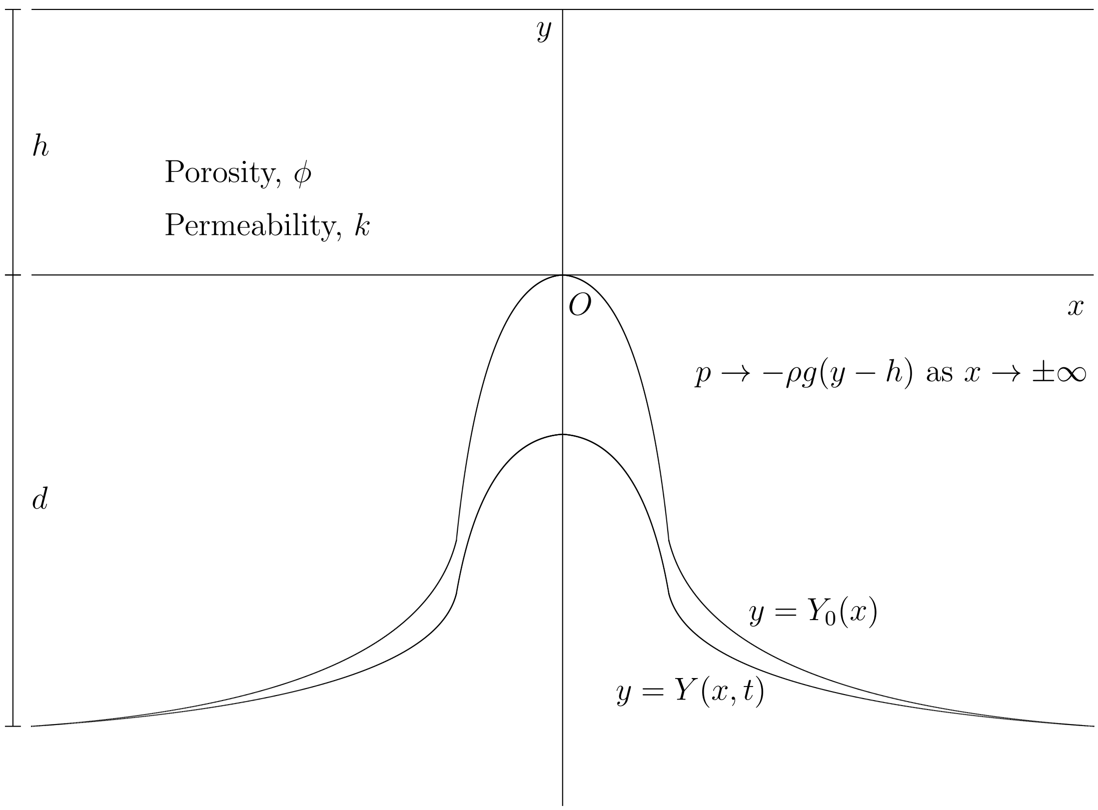

Figure 4.1: An inverted crack of height d formed in asphalt at a depth h away from the surface of the sample. The line $y = Y_0(x)$ gives the initial position of the interface of the bitumen while the line $y = Y(x,t)$ gives its position at a later time t.

$$\hat{\mathbf{u}} \to 0, \;\; \hat{p} \to 0, \;\; \text{as } \hat{x} \to \pm\infty \tag{4.10}$$

and

$$\hat{\mathbf{u}} = 0, \;\; \hat{Y}\left(\hat{x}, \hat{t}\right) = \hat{Y}_0\left(\hat{x}\right), \;\; \text{when } \hat{t} = 0. \tag{4.11}$$

In addition the no-slip and no-penetration conditions are imposed at $y = -d$ or equivalently in non-dimensionalised form $\hat{y} = -1$. Here $\hat{\mathbf{u}}$ is velocity of the bitumen, $\hat{p}$ the pressure, $\hat{x}$ and $\hat{y}$ are the Cartesian co-ordinates, $\hat{Y}_0$ is the initial profile of the boundary and $\hat{Y}\left(\hat{x}, \hat{t}\right)$ is the profile of the interface at time $\hat{t}$.

Secondly the finite case will be examined allowing easier comparison to experiment. Here h will be finite and boundaries on the domain will exist at $\pm\hat{x}_{(\max)}$. This results in the boundary conditions

$$\hat{\mathbf{u}} \to 0 \;\text{ at the domain boundaries } \hat{y} = -1 \;\text{ and }\; x = \pm\hat{x}_{\max} \tag{4.12}$$

as well as

$$\hat{\mathbf{u}} = 0, \;\; \hat{Y}\left(\hat{x}, \hat{t}\right) = \hat{Y}_0\left(\hat{x}\right), \;\; \text{when } \hat{t} = 0. \tag{4.13}$$

In addition, the kinematic condition at the free surface [Cruse and Rizzo, 1968] is given by

$$\frac{\partial \hat{Y}}{\partial \hat{t}} + \hat{u}\frac{\partial \hat{Y}}{\partial \hat{x}} = \hat{v} \tag{4.14}$$

holds for both the semi-infinite and finite domains. Here $\hat{u}$ and $\hat{v}$ are the velocity in the $\hat{x}$ and $\hat{y}$ direction respectively.

4.2.3 Modelling a Horizontal Crack

The second class of crack to be looked at in this research will be the horizontal crack. This is a crack of height d in asphalt stemming from the side of a sample with the initial height of the tip a depth of h below the surface at time $\hat{t} = 0$. A visual representation of this crack using the original variables is in Fig. 4.2.

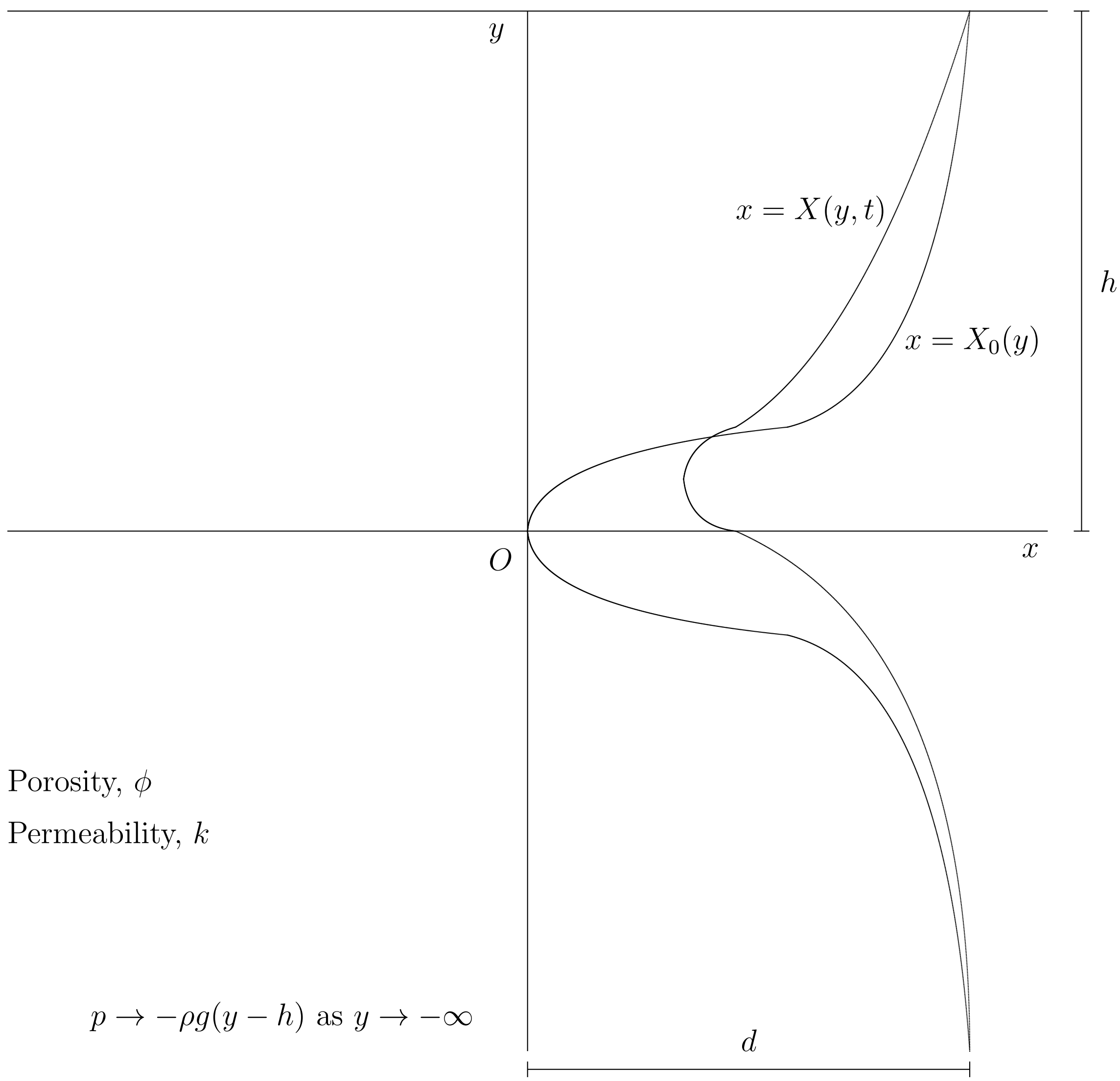

Figure 4.2: A horizontal crack of height d formed in asphalt. The distance between the tip of the crack and the surface of the asphalt at time $t = 0$ is h. The line $x = X_0(y)$ gives the initial position of the interface of the bitumen while the line $x = X(y,t)$ gives its position at a later time t.

Again a domain better suited to modelling asphalt and one more comparable to experiments performed in this chapter will be reviewed here. To begin the semi-infinite case will be analysed to represent healing in asphalt. Here h will be assumed infinite and the model extends infinitely in the $\pm\hat{y}$ directions with boundaries at $x = \pm d$ or $\hat{x} = \pm 1$ when expressed in non-dimensionalised units. Here the boundary conditions are

$$\hat{\mathbf{u}} \to 0, \;\; \hat{p} \to 0, \;\; \text{as} \;\; \hat{y} \to \pm\infty \tag{4.15}$$

and

$$\hat{\mathbf{u}} = 0, \;\; \hat{X}\left(\hat{y}, \hat{t}\right) = \hat{X}_0\left(\hat{y}\right), \;\; \text{when} \;\; \hat{t} = 0. \tag{4.16}$$

In addition the no-slip and no-penetration conditions are imposed at $\hat{x} = \pm 1$. Here $\hat{\mathbf{u}}$ is velocity of the bitumen, $\hat{p}$ the pressure, $\hat{x}$ and $\hat{y}$ are the Cartesian co-ordinates, $\hat{X}\left(\hat{y}, \hat{t}\right)$ represents the free surface and $\hat{X}_0\left(\hat{y}\right)$ is its initial position.

As well as this the finite case will be looked at to allow a valid comparison to experiment. Here h will be finite as well as boundaries on the domain which exist at $\hat{x} \pm 1$. This results in the boundary conditions

$$\hat{\mathbf{u}} \to 0 \;\text{at the domain boundaries}\; \hat{x} = \pm 1 \;\text{and}\; \hat{y} = -\frac{h}{d} \tag{4.17}$$

as well as

$$\hat{\mathbf{u}} = 0, \;\; \hat{X}\left(\hat{y}, \hat{t}\right) = \hat{X}_0\left(\hat{y}\right), \;\; \text{when} \;\; \hat{t} = 0. \tag{4.18}$$

As well as these conditions, at the free surface

$$\frac{\partial \hat{X}}{\partial \hat{t}} + \hat{v}\frac{\partial \hat{X}}{\partial \hat{y}} = \hat{u} \tag{4.19}$$

is applicable [Cruse and Rizzo, 1968] for both the semi-infinite and finite domains. Here $\hat{u}$ and $\hat{v}$ are the velocity in the $\hat{x}$ and $\hat{y}$ direction respectively.

4.2.4 Modelling two Simultaneous Vertical Cracks

The final class of crack to be examined in this chapter will be the case where there are two vertical cracks in the same piece of asphalt, one stemming from the top of the piece and another from the bottom. In this case the crack stemming from the top of the asphalt to the origin of the system will have height $d_1 = h$, the crack at the bottom of the system will have height d_2 and the vertical distance be height of the two cracks will be taken to be d_3. Fig. 4.3 shows a visual display of the crack in the original variables.

The semi-infinite case will be reviewed first to model healing in asphalt. The model extends infinitely in the $\pm\hat{x}$ directions with boundary at $y = -\left(d_2 + d_3\right)$ or when presented in non-dimensionalised variables when length is scaled with d_1, $\hat{y} = -\left(d_2 + d_3\right)/d_1$. The boundary conditions are

$$\hat{\mathbf{u}} \to 0, \;\; \hat{p} \to 0, \;\; \text{as} \;\; \pm\hat{x} \to \infty \tag{4.20}$$

and

$$\hat{\mathbf{u}} = 0, \;\; \hat{Y}_{\mathrm{a}}\left(\hat{y}, \hat{t}\right) = \hat{Y}_{\mathrm{a0}}\left(\hat{x}\right), \;\; \hat{Y}_{\mathrm{b}}\left(\hat{y}, \hat{t}\right) = \hat{Y}_{\mathrm{b0}}\left(\hat{x}\right), \;\; \text{when} \;\; \hat{t} = 0. \tag{4.21}$$

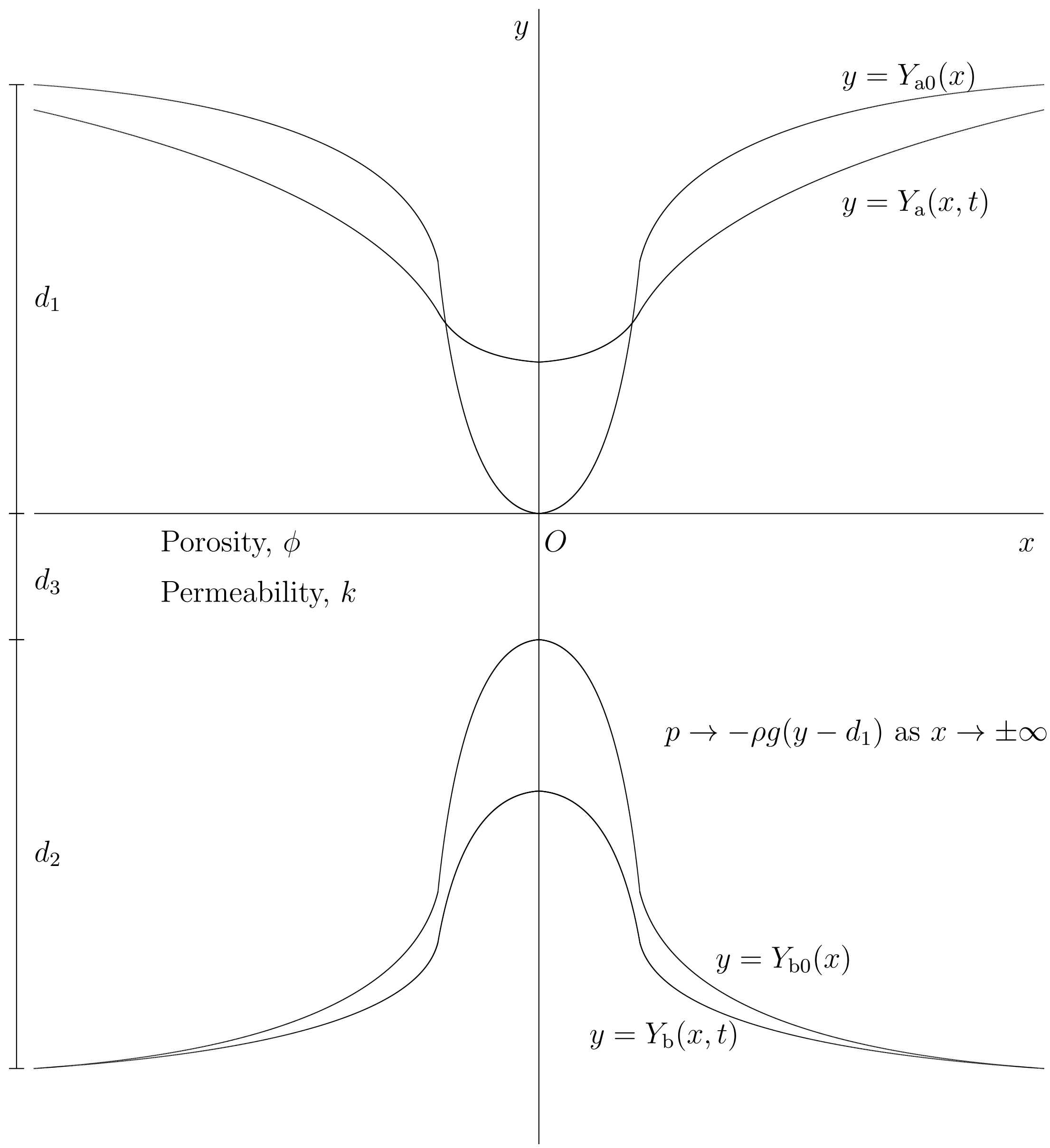

Figure 4.3: Two vertical cracks of height d_1 and d_2 formed in asphalt. There is a distance of d_3 between the initial tips of the two cracks at time $t = 0$. The lines $y = Y_{a0}(x)$ and $y = Y_{b0}(x)$ give the initial positions of the interface of the bitumen while the lines $y = Y_a(x,t)$ and $y = Y_b(x,t)$ give their positions at a later time t.

The no-slip and no-penetration conditions are also imposed at $\hat{y} = -(d_2 + d_3)/d_1$. Here $\hat{\mathbf{u}}$ is velocity of the bitumen, $\hat{p}$ the pressure, $\hat{x}$ and $\hat{y}$ are the Cartesian co-ordinates, $\hat{Y}_a\left(\hat{y}, \hat{t}\right)$ and $\hat{Y}_b\left(\hat{y}, \hat{t}\right)$ are the positions of the upper and lower cracks respectively while $\hat{Y}_{a0}\left(\hat{x}\right)$ and $\hat{Y}_{b0}\left(\hat{x}\right)$ are their respective initial positions.

Finally the finite case will be analysed to give a valid comparison to experiment. Here boundaries on the domain will exist at $\pm\hat{x}_{\max}$ and $\hat{y} = -(d_2 + d_3)/d_1$. This results in the boundary conditions

$$\hat{\mathbf{u}} \to 0 \text{ at the domain boundaries } \hat{x} = \pm\hat{x}_{\max} \text{ and } \hat{y} = -\frac{(d_2 + d_3)}{d_1} \tag{4.22}$$

as well as

$$\hat{\mathbf{u}} = 0,\ \hat{Y}_{\mathrm{a}}\left(\hat{y}, \hat{t}\right) = \hat{Y}_{\mathrm{a0}}\left(\hat{x}\right),\ \hat{Y}_{\mathrm{b}}\left(\hat{y}, \hat{t}\right) = \hat{Y}_{\mathrm{b0}}\left(\hat{x}\right),\ \text{when } \hat{t} = 0. \tag{4.23}$$

Finally, at the free surfaces [Cruse and Rizzo, 1968]

$$\frac{\partial \hat{Y}_a}{\partial \hat{t}} + \hat{u}\frac{\partial \hat{Y}_a}{\partial \hat{x}} = \hat{v} \tag{4.24}$$

and

$$\frac{\partial \hat{Y}_b}{\partial \hat{t}} + \hat{u}\frac{\partial \hat{Y}_b}{\partial \hat{x}} = \hat{v} \tag{4.25}$$

both apply for the semi-infinite and finite domains. Here $\hat{u}$ and $\hat{v}$ are the velocity in the $\hat{x}$ and $\hat{y}$ direction.

4.2.5 Numerical Solution

Here boundary integral methods will be used in conjunction with Green's functions to find a numerical solution to the pressure gradient on the surface of the various cracks being analysed. This in turn will allow for the computation of the movement of the boundary with time.

Here the relationships [Fernández-Guasti et al., 2012]

$$\nabla \cdot (\phi_1 \nabla \phi_2 - \phi_2 \nabla \phi_1) = \phi_1 \nabla^2 \phi_2 - \phi_2 \nabla^2 \phi_1 \tag{4.26}$$

and [Stolze, 1978]

$$\int\int_{A_c} \nabla \cdot (\phi_1 \nabla \phi_2 - \phi_2 \nabla \phi_1)\, dA_c = \int_S \hat{\mathbf{n}} \cdot (\phi_1 \nabla \phi_2 - \phi_2 \nabla \phi_1)\, dC \tag{4.27}$$

are used where $\hat{\mathbf{n}}$ is the normal vector to the boundary C which surrounds area A_c, with $\hat{\mathbf{n}}$ pointing outwards. The relationship holds for any two twice differentiable fields ϕ_1 and ϕ_2.

Here ϕ_1 is substituted for the pressure on the boundary, $\hat{\mathbf{p}}$ and ϕ_2 is substituted for the Green's function appropriate to the domain of the model. As per the derivation in chapter 3 this leads to the result

$$\mathbf{A}\hat{\mathbf{p}}' = (\mathbf{B} - \pi\mathbf{I})\,\hat{\mathbf{p}}. \tag{4.28}$$

Here $\hat{\mathbf{p}}'$ is the pressure gradient on the surface of the crack, $\mathbf{I}$ is the identity matrix and $\mathbf{A}$ and $\mathbf{B}$ are matrices which have values dependent on the relationship between the pressures at various points on the boundary, their distance apart and the Green's function defining the domain.

This gives a value of the pressure gradient at the boundary which in turn can be used to compute the movement of the surface of the crack over time.

4.2.6 Domains for the Numerical Solution

The domain of the simulation is decided by the Green's function used and substituted for ϕ_2 in (4.26) and (4.27). The Green's function used to define the domain of the simulation varies depending on the crack being modelled.

In the cases of the inverted vertical crack and modelling two simultaneous vertical cracks in asphalt a domain of infinite length in the $\pm\hat{x}$ directions is used with a finite depth coinciding with the crack's base, a. To do this the method of images is used [Pozrikidis, 2002], giving a Green's function of

$$G = \frac{1}{4\pi} \ln \left(\frac{(\hat{x} - \hat{x}_0)^2 + (\hat{y} + \hat{y}_0 - 2a)^2}{(\hat{x} - \hat{x}_0)^2 + (\hat{y} - \hat{y}_0)^2} \right). \tag{4.29}$$

Here G is the Green's function, $\hat{x}$ and $\hat{y}$ are the coordinates of the varying point on the surface while $\hat{x}_0$ and $\hat{y}_0$ the coordinates of the constant singular source.

Here the closed surface over which the integration in the boundary integral method will take place is defined as the free surface of the bitumen, including the crack over all of which $\hat{p}$ is defined. The domain is also considered bounded by the lines $\hat{x} = \pm b$ for the limit as b approaches ∞ and the line $\hat{y} = a$. On these three lines the velocity of the fluid is considered to be zero.

A horizontal crack in asphalt however, can be better modelled by using a domain infinite in the $\pm\hat{y}$ directions however bounded in the $\pm\hat{x}$ directions. This can be accomplished by using

$$G = \frac{1}{4\pi} \ln \left(2 \left(\cosh \left(\frac{2\pi (\hat{y} - \hat{y}_0)}{b} \right) - \cos \left(\frac{2\pi (\hat{x} - \hat{x}_0)}{b} \right) \right) \right) + \frac{(\hat{y} - \hat{y}_0)}{4b}. \tag{4.30}$$

This is a variation on the Green's function, G found in [Linton, 1999, Moroz, 2006]. Here b is the width of the domain in the $\hat{x}$ direction, $\hat{x}$ and $\hat{y}$ are the coordinates of the varying point on the surface. $\hat{x}_0$ and $\hat{y}_0$ give the coordinates of the constant singular source. This Green's function treats the domain infinitely repeating with no flow between adjacent sections.

The domain for this Green's function is defined formally by considering a surface bound by the free surface where $\hat{p}$ is defined and on the lines $\hat{y} = \pm a$ in the limit as a tends to ∞ and $\hat{x} = \pm b$ on which the velocity of the fluid will be zero. Here on lines where the velocity of fluid is equal to zero the integral over the boundary collapses to an integral over the free surface as the condition that the pressure gradient is also equal to zero on those lines.

For all classes of crack when comparing results of the simulations to those of the crack flow experiments the boundaries of the experiments must be observed. This requires the use of the method of images [Li, 1998] combined with (4.30) to produce

$$G = \frac{1}{4\pi} \ln \left(\frac{\left(\cosh \left(\frac{2\pi(\hat{y} - \hat{y}_0)}{b} \right) - \cos \left(\frac{2\pi(\hat{x} - \hat{x}_0)}{b} \right) \right)}{\left(\cosh \left(\frac{2\pi(\hat{y} + \hat{y}_0 - 2a)}{b} \right) - \cos \left(\frac{2\pi(\hat{x} - \hat{x}_0)}{b} \right) \right)} \right) - \frac{\hat{y}_0 - a}{2b} \tag{4.31}$$

as a Green's function G. Here the domain repeats periodically in the $\pm\hat{x}$ directions and uses the method of images to enforce a boundary on the bottom of the domain at $\hat{y} = a$.

Once again $\hat{x}$ and $\hat{y}$ are the coordinates of the varying point on the surface while $\hat{x}_0$ and $\hat{y}_0$ give the coordinates of the constant singular source. Once again for the sections of the boundary on which the velocity is equal to zero the equation (4.28) reduces to an integral over just the free surface.

In this case the closed domain is bounded by the free surface or surfaces depending on the crack where $\hat{p}$ is known. In addition it is bounded by the lines $\hat{x} = \pm b$ and $\hat{y} = a$ on which, the condition that the velocity of the fluid is zero holds. As with the previous domains the boundary integral equation here collapses to just an integral over the free surface.

4.2.7 Time-stepping

The time-stepping for the simulation of all three classes of crack studied here was conducted using the Crank Nicholson method. This is an implicit time-stepping method which can be expressed by [Crank and Nicolson, 1947]

$$\hat{Y}^{n+1} = \hat{Y}^{n} + \frac{1}{2}\left[f_g\left(\hat{t}^{n}, \hat{Y}^{n}\right) + f_g(\hat{t}^{n+1}, \hat{Y}^{n+1})\right]\Delta\hat{t}. \tag{4.32}$$

Here $\hat{Y}^n$ is the position of the surface before the n^{th} time-step takes place, $\hat{t}^n$ is the time before the n^{th} time-step takes place, $\Delta\hat{t}$ is the size of the time-step and $f_g\left(\hat{t}^n, \hat{u}^n\right)$ is the value of the pressure gradient on the surface. In the method the value of $\hat{Y}^{n+1}$ is derived iteratively.

4.3 Materials and Methods

In this section the experiments performed for this section of the research will be explained in full. In addition the materials used in said experiments will be clarified. In this case the experiments performed were a variation of the crack flow test performed in the first chapter of this thesis however here they were performed in a variety of orientations to judge the effect of this on the healing of cracks.

4.3.1 Bitumen

Throughout the chapter five different types of bitumen were used to ensure the comparisons to the model could be replicated over a variety of surface tensions and viscosities. The relevant properties of each of the styles of bitumen used can be found in Table 4.1.

Bitumen type	Surface tension (Nm^{-1})	Dynamic viscosity (MPl)
Sample 1	0.0324	0.103
Sample 2	0.0374	0.784
Sample 3	0.0318	0.328
Sample 4	0.0300	1.103
Sample 5	0.0391	0.892

Table 4.1: A table with the surface tensions and viscosities of each type of bitumen used in the chapter.

4.3.2 Crack Flow Test

To further validate the accuracy of the model experiments were performed with cracks of two different sizes. Here the experiment was performed under multiple different orientations.

First a sheet of bitumen of dimensions 73×23×1 mm was produced by pouring heated bitumen into a moulds. The sheets of bitumen had triangular gaps in them to simulate a crack, allowing for the observation of the bitumen flowing into the gap. The gaps were in two sizes with maximum widths of 10 mm and 20 mm. The height of the crack was always 10 mm. After the bitumen was placed in the mould it was frozen for a period of at least two hours at -20°C to allow removal without deformation of the sheet.

The sheets of bitumen were placed between two glass plates to form a Hele-Shaw cell. Here the thickness of the sample ensured that it behaved as if in a porous medium [Nield and Bejan, 2006, Richardson, 1972]. All sides of the sheet were then sealed with plasticine to create a barrier and prevent the bitumen from leaking out the sides of the plates.

Finally the samples were placed in an oven which had been pre-heated to 45°C for at least 30 mins. Pictures were taken every 30 minutes to record the movement of the bitumen. An example of the experimental set-up of each orientation of crack can be seen in Fig. 4.4, Fig. 4.5 and Fig. 4.6. Here at least four repeats of each experiment were performed to ensure the reliability of the results.

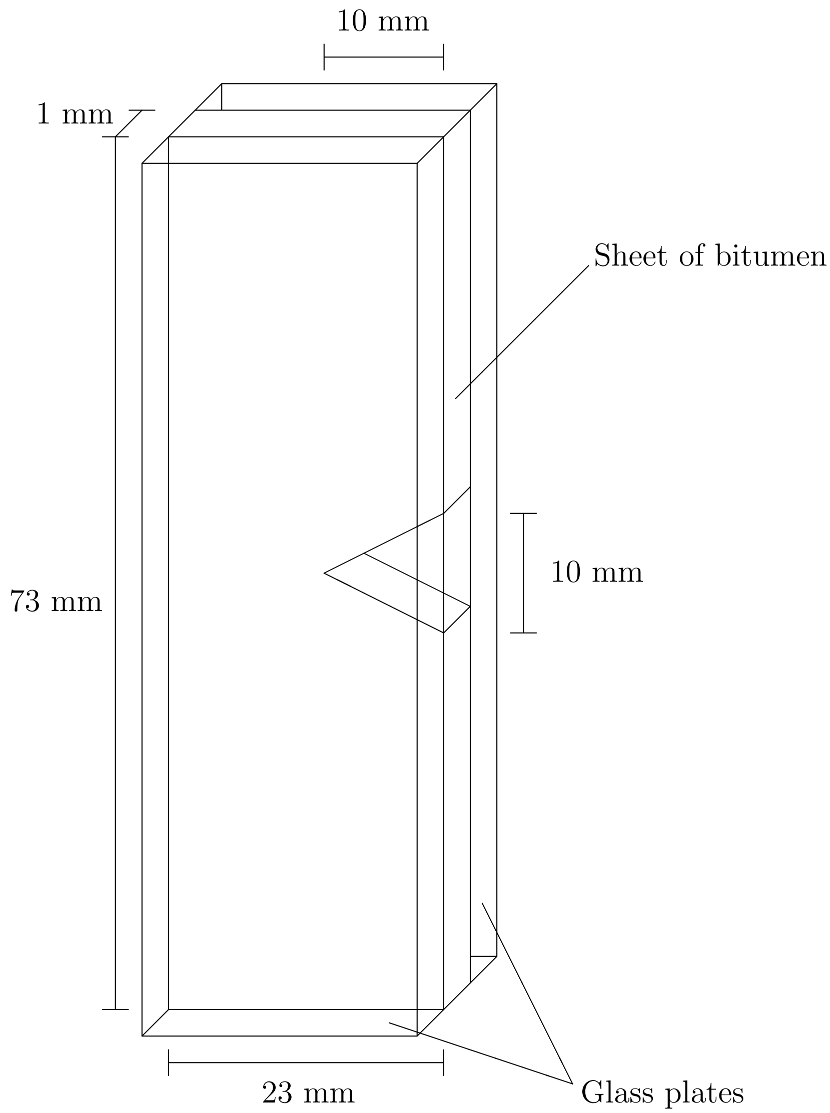

Figure 4.4: The above schema displays the set-up of the crack flow test. It comprises of a 73×23×1 mm sheet of bitumen with a triangular section removed sandwiched between two glass plates. After being placed in an oven at 45°C the flow of this sheet of bitumen is monitored over time. This image displays the triangular section taken out of the sheet of bitumen to have a height of 10mm and a maximum width of 10 mm. Another set of experiments were also run using triangles with a height of 10 mm and maximum width 20 mm.

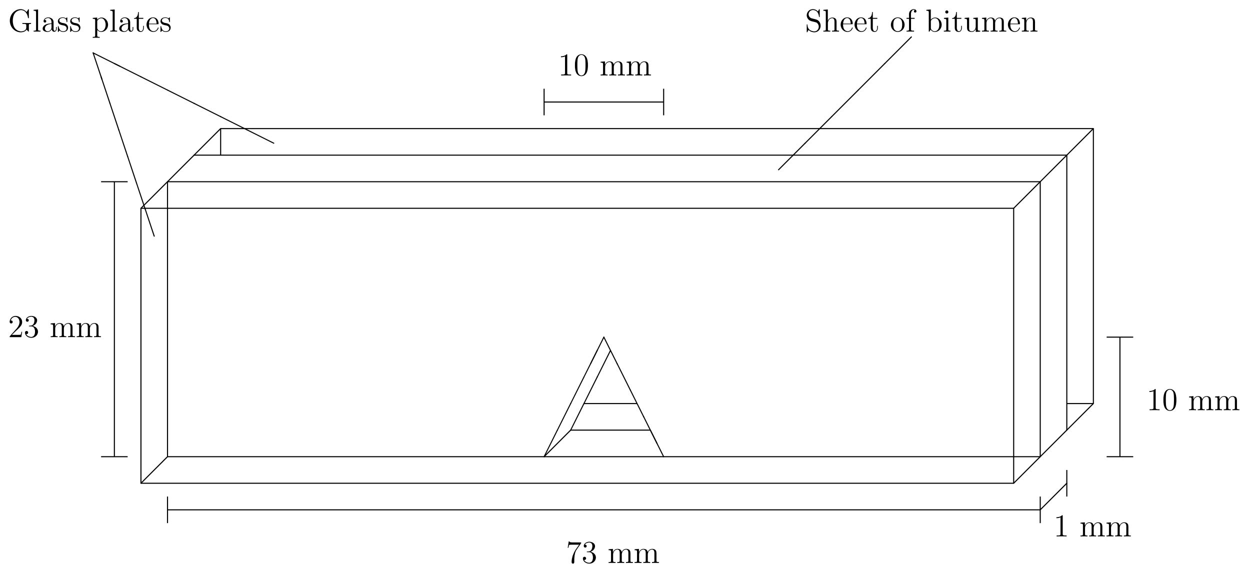

Figure 4.5: The above schema displays the set-up of the crack flow test. It comprises of a 73×23×1 mm sheet of bitumen with a triangular section removed sandwiched between two glass plates. After being placed in an oven at 45°C the flow of this sheet of bitumen is monitored over time. This image displays the triangular section taken out of the sheet of bitumen to have a height of 10mm and a maximum width of 10 mm. Another set of experiments were also run using triangles with a height of 10 mm and maximum width 20 mm.

4.3.3 Surface Tension Test

To prepare samples of bitumen for testing each type of bitumen was heated at 130°C and then poured over a glass slide. These were then laid to rest for 24 hours and covered to prevent dust from contaminating the samples. After the rest period a goniometer was used to measure the curvature of a series of drops of test liquids resting on the bitumen samples. In these tests water, ethylene glycol and diiodomethane were used as the test liquids.

As the surface energy of the test liquids is known this can be used with the equation

$$\gamma_{\mathrm{S}} = \gamma_{\mathrm{SL}} + \gamma_{\mathrm{L}} \cos\theta, \tag{4.33}$$

where γ_{S} is the surface energy of the bitumen, γ_{SL} is the solid-liquid interface energy, γ_{L} is the surface energy of the test liquid and θ is the contact angle between the bitumen and the test liquid. This allows the surface energy of the bitumen to be calculated.

4.3.4 Viscosity Tests

To measure the viscosity of the bitumen a Brookfield viscometer was used. Prior to any measurements taking place the heater and spindle of the viscometer were both preheated for one hour. After this 9.5 g of bitumen was placed in a tube and placed in the heater for a further 30 mins to bring it up to the temperature. After this heating

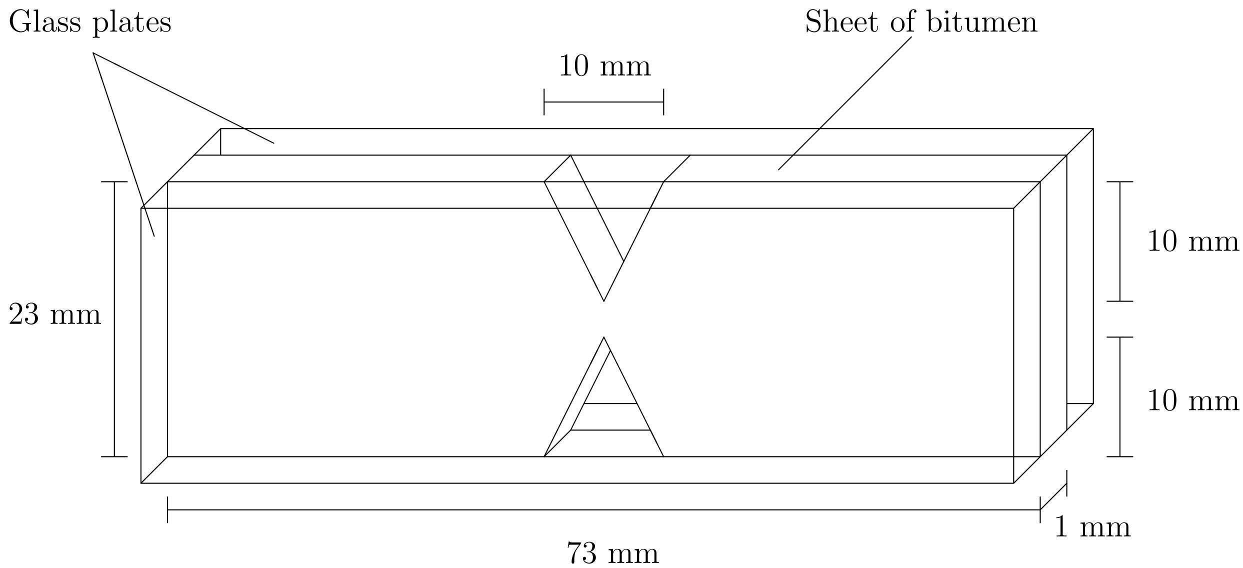

Figure 4.6: The above schema displays the set-up of the crack flow test. It comprises of a 73×23×1 mm sheet of bitumen with two triangular sections removed sandwiched between two glass plates. After being placed in an oven at 45°C the flow of this sheet of bitumen is monitored over time. This image displays the triangular sections taken out of the sheet of bitumen to have a height of 10 mm and a maximum width of 10 mm. Another set of experiments were also run using triangles with a height of 10 mm and maximum width 20 mm.

had taken place the viscometer was used to measure the viscosity of each of the bitumen samples. Two repeats of each measurement were made to ensure no significant deviation in measurements occurred.

4.4 Results and Discussion

In this section the results of computing the numerical method will be presented and compared to the results of the laboratory experiments laid out in the previous section. This will begin with looking at the case of an inverted crack, then move on to horizontal cracks before concluding by examining the results pertaining to two simultaneous vertical cracks. While no extra verification of the numerics is presented in this section the results of the verification performed in 2.4.2 and 2.4.3 are applicable to the code used here.

Throughout this section a representative Bond number was needed to compute the solutions. This was chosen by assuming a bitumen density of 1030 kgm^{-3}, a crack height of 0.01 m, an acceleration due to gravity of 9.81 ms^{-2} and a surface tension of 0.03 Nm^{-1}. Using these with (2.16) gives a Bond number of 33.681. This Bond number will be used for calculations that are not directly compared to experiments which use bitumen with a known value of surface tension.

4.4.1 Inverted Crack Results

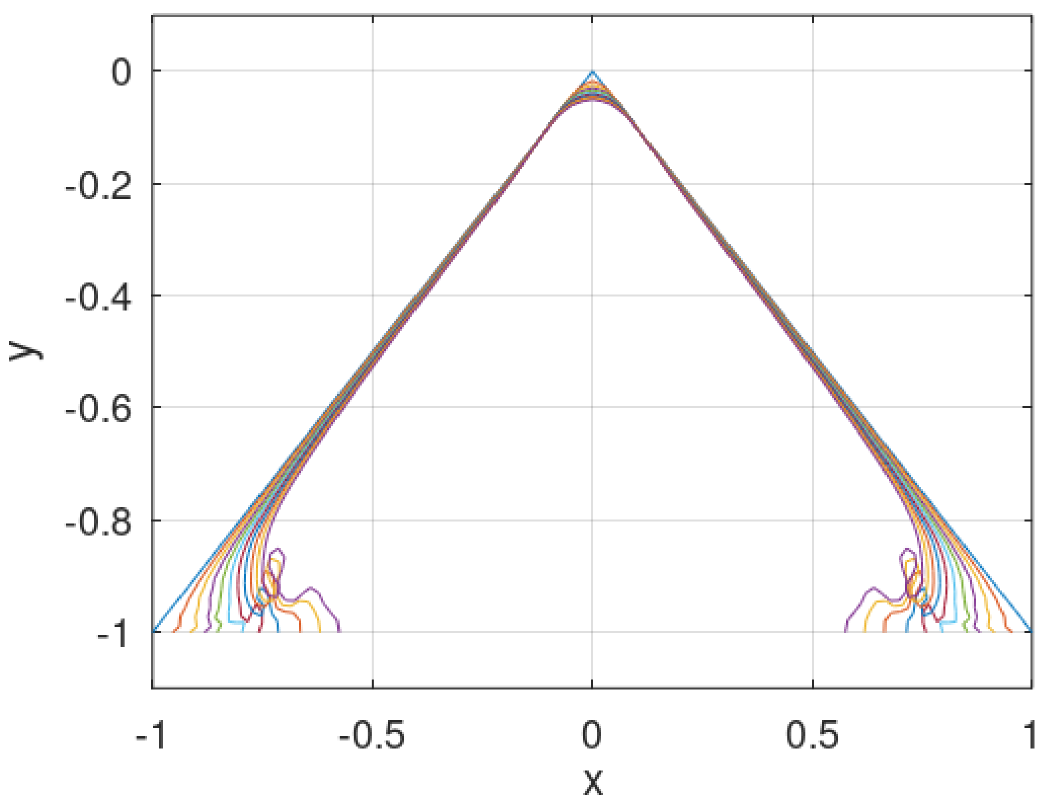

Figure 4.7: The evolution of an inverted crack with time under the effects of gravity and surface tension. The blue line represents the initial crack and the other lines the evolution of the surface. Here the Bond number was taken to be $B_o = 33.681$.

The first style of crack to be simulated was a vertical one originating at the bottom of a piece of asphalt. Here you can see the predicted healing profile of a triangular crack with width equal to twice its height at its base in Fig. 4.7.

To compute the numerical solution for this figure (4.29) was used as a Green's function with the base of the domain defined as $\hat{y} = -1$. Here 151 equally spaced points were used to represent the surface with a Bond number of $B_o = 33.681$ used. The advections to the surface were made in steps of $\hat{t} = 0.00001$ with the lines on the graph corresponding to the evolution of the surface every 50 time-steps. Here surface tension and gravity are both included as driving forces for the movement of the crack.

There are a few behaviours of note in in this graph. Firstly we see that the flow of bitumen into the crack is concentrated both at the tip of the crack and to a greater extent at its base. This is likely due to the increased pressure lower down in the domain.

Some of the features of this graph make more sense when contrasted against the numerical solution of a crack healed only by gravity. In Fig. 4.8 the healing of the same crack is examined with the effects of surface tension removed.

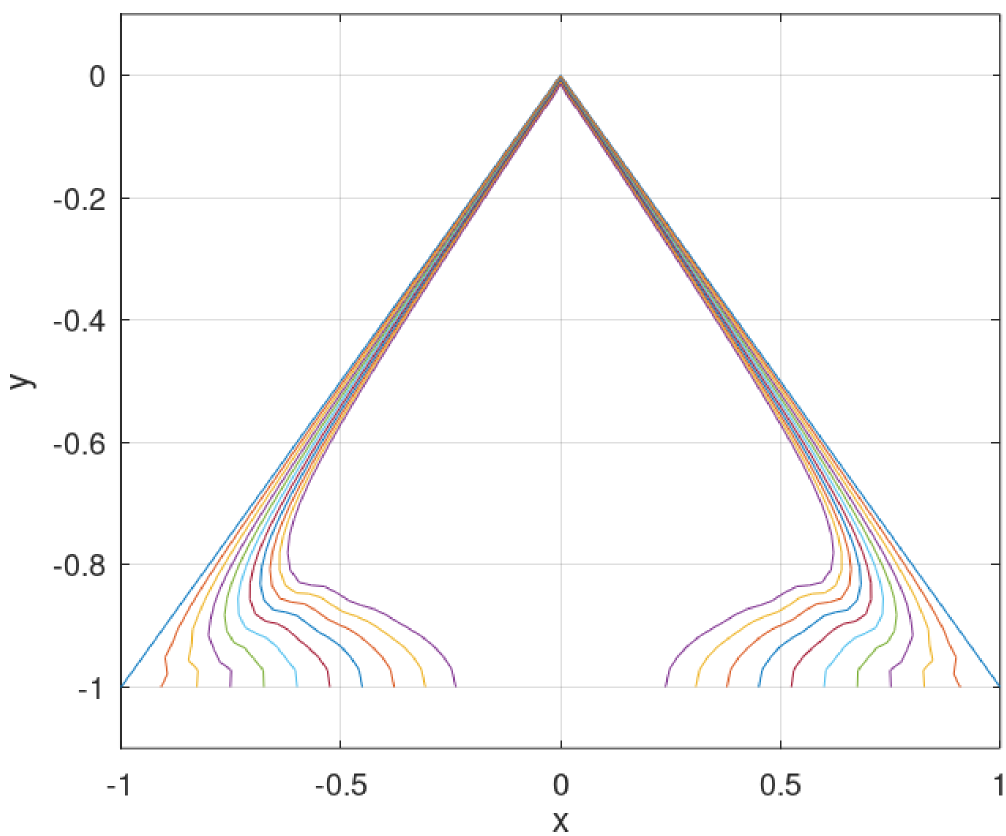

Figure 4.8: The evolution of an inverted crack with time under just the effect of gravity. The blue line represents the initial crack and the other lines the evolution of the surface. Here the Bond number was taken to be $B_o = 33.681$.

To produce this graph (4.29) was the chosen Green's function with the base of the domain defined as $\hat{y} = -1$. Again 101 equally spaced points were used to represent the surface with a Bond number of $B_o = 33.681$ used. Time-steps of $\hat{t} = 0.00005$ were used to move the surface with the lines on the graph corresponding to the evolution of the surface every 20 time-steps. In this case only gravity is used to drive the movement of the crack.

Here we see a lot of similarities to the behaviours seen in Fig. 4.7, but also a few key differences. Firstly the flow of bitumen into the tip of the crack is nearly absent when the surface tension is removed. This indicates that the flow into that area was mainly driven by surface tension due to the high curvature at the tip of the crack and not by the effects of gravity.

The next big difference between the two figures is the behaviour of the bitumen at the base of the domain. In Fig. 4.8 the bitumen flows freely into the base of the crack, driven by gravity and the comparatively higher pressure lower down in the crack. In Fig. 4.7 however, the effects of gravity and surface tension act in opposition slowing the movement. Here we also see instabilities form. It appears that rather than act to stop the instabilities as would be expected in reality here the surface tension slows the base of the front of bitumen moving into the crack causing overextension in the top part of the front which leads to the instabilities seen here.

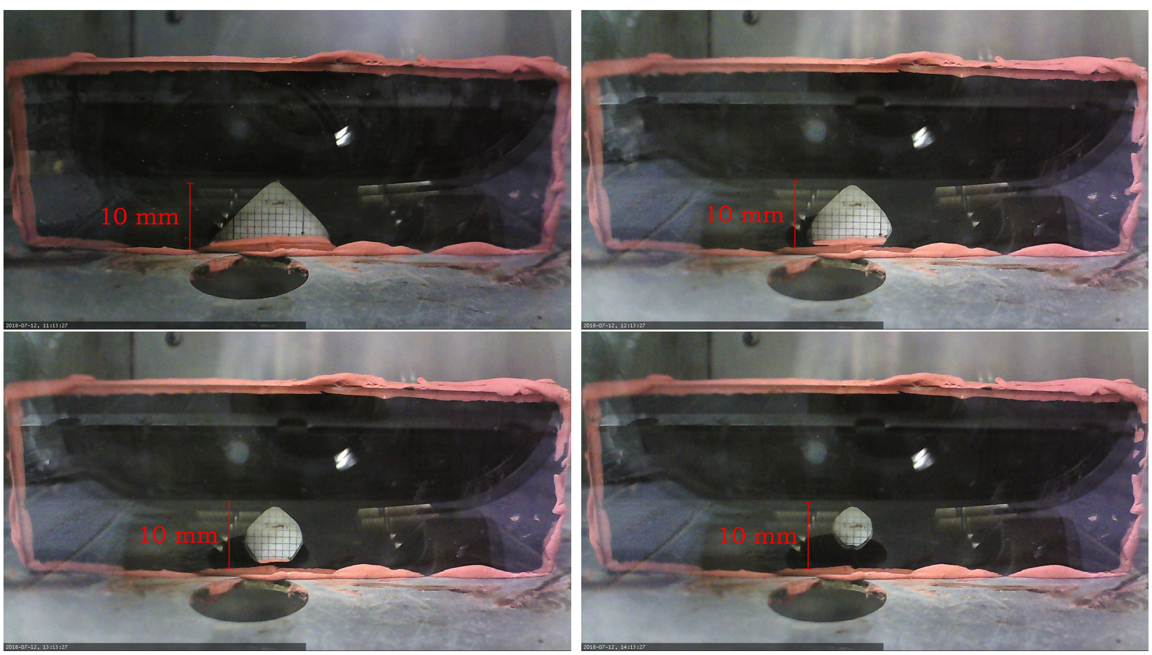

Figure 4.9: The movement of bitumen into a 10 mm tall crack initially 20 mm wide at its widest point. Top left is before heating, top right is after 60 minutes, bottom left is after 120 minutes and bottom right is after 180 minutes.

An illustrative example of the experimental results of the crack healing test for the inverted vertical crack can be seen in Fig. 4.9. Here the top left image shows the initial state of the crack, the top right gives its condition after 60 mins, the bottom left after

120 mins and bottom right after 180 mins.

As can be clearly seen the flow of bitumen is mainly concentrated at the bottom of the crack. The tip of the crack on the other hand fills slightly in the first 60 mins but remains stationary thereafter. These general behaviours do correspond with the behaviours predicted in the numerical results, however the surface of the crack does not experience any of the instabilities seen there. While this initially seems to represent the gravity driven healing most closely it is worth noting that the steepness of the fronts of bitumen moving into the base of the crack exceeds that of the gravity driven healing and more closely corresponds to the healing seen when gravity and surface tension are both applied before instabilities occur.

The apparent movement of the tip of the crack throughout this set of experiments is displayed in Fig. 4.10 and Fig. 4.11. Due to instabilities the numerical results were not stable enough to run to simulate the 150 min duration of the experiment and so could not be included here.

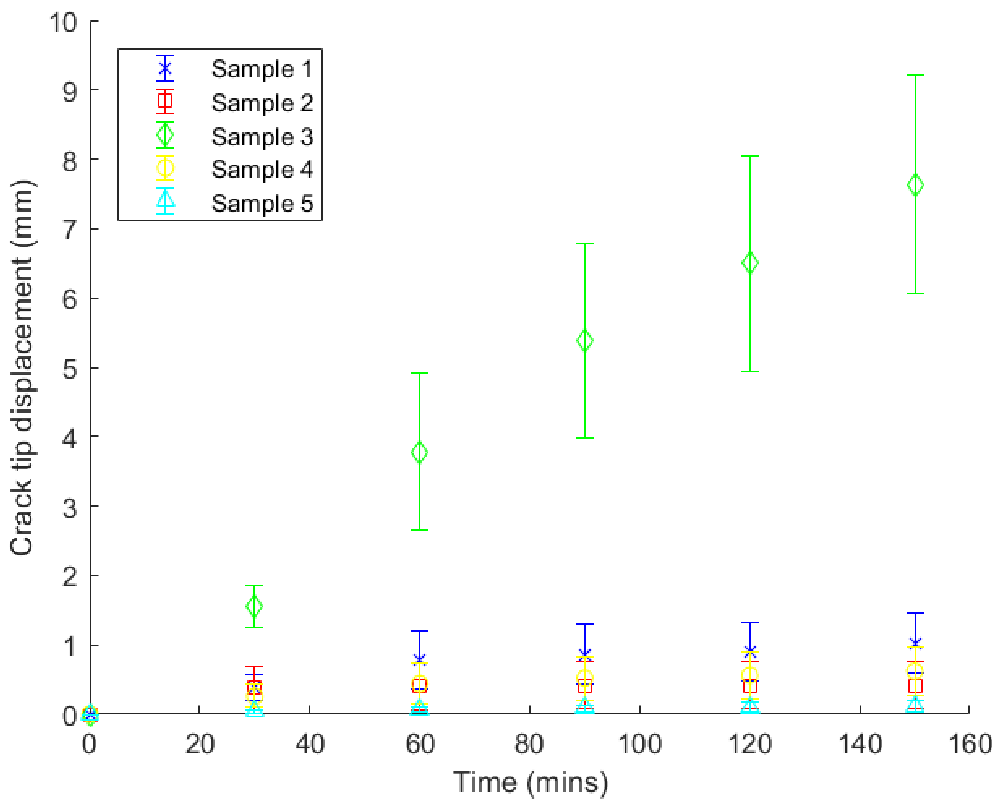

Figure 4.10: The experimental results for the movement of the tip of the 10 mm wide inverted vertical crack with time.

Here with the exception of sample 3, which proved an outlier in both cases we see only very small movement of the tip of the crack. The results for the narrower crack show considerably more healing here which fits with the concept of the movement of the tip of the crack in this case being driven mainly by surface tension. For the narrower

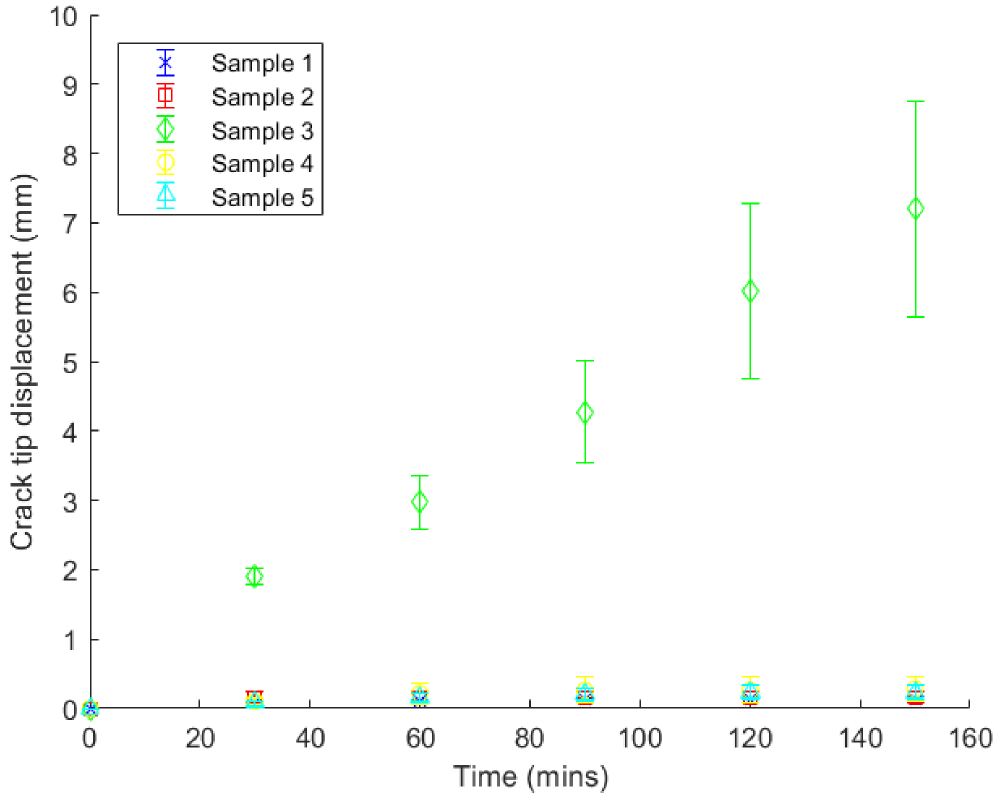

Figure 4.11: The experimental results for the movement of the tip of the 20 mm wide inverted vertical cracks with time.

crack the curvature at the tip will be much higher so the increased flow lies in line with intuition.

4.4.2 Horizontal Crack Results

The second class of crack to be analysed was the horizontal crack. The predicted healing profile of a crack with width twice its length at its widest point is displayed in Fig. 4.12.

To produce this graph (4.30) was the chosen Green's function, bounded by $\hat{x} = \pm 3.65$. Here 101 equally spaced points were used to represent the surface. A Bond number of $B_o = 33.681$ used. Time-steps of $\hat{t} = 0.0001$ were used to move the surface with the lines on the graph corresponding to the evolution of the surface every 20 time-steps. In this case both gravity and surface tension were included in the relevant equations.

In the initial time-steps the majority of the flow of bitumen into this crack occurs at the tip. This is likely due to surface tension and a response to the high levels of curvature at the tip of the crack. Once the tip of the crack has been smoothed out the flow into the tip slows and it appears that the whole crack appears to flow upwards.

A example of the healing of a crack during the crack healing experiments carried out can be seen in Fig. 4.13. In these pictures the top left image shows the initial state of

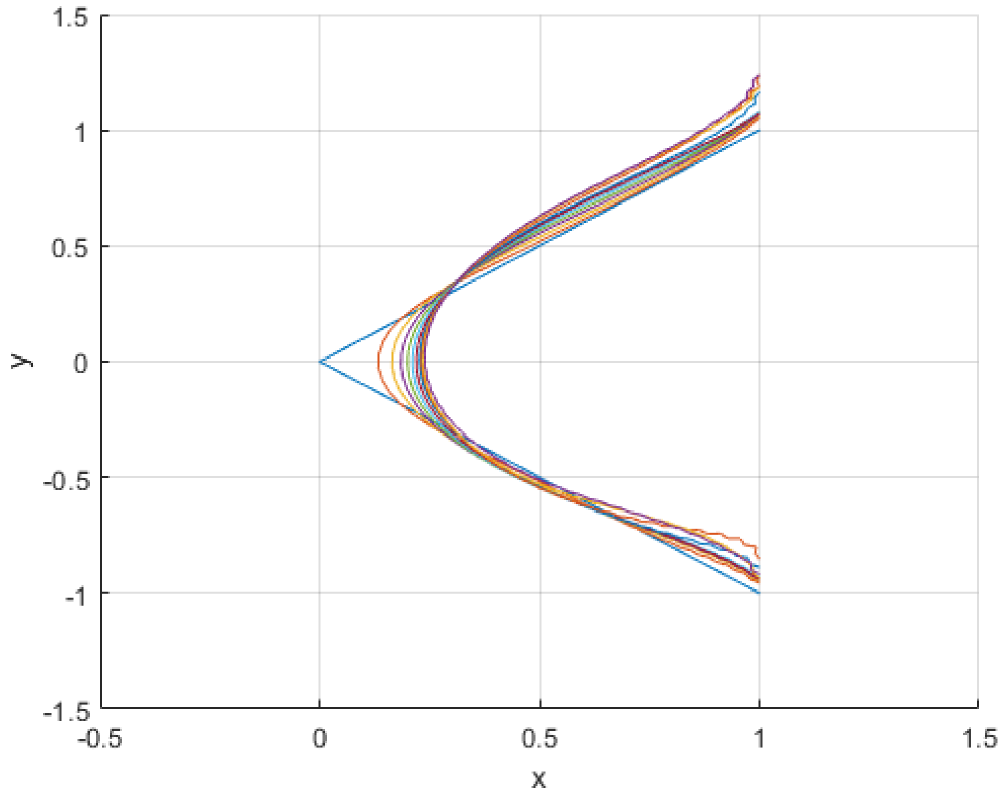

Figure 4.12: The predicted evolution of a horizontal crack with time. The blue line represents the initial crack and the other lines the evolution of the surface. Here the Bond number was taken to be $B_o = 33.681$.

the crack, the top right gives its condition after 60 mins, the bottom left after 120 mins and bottom right after 180 mins.

The greatest initial movement of the crack in the first 60 mins of healing is present near the tip although there is also a narrowing of the width of the crack at its widest point by roughly 1 mm in each direction while this happens. For the next two hours the top surface of the crack remains steady while the bottom surface rises and the tip of the crack moves further to the right.

Comparing the results of the numerical method and the laboratory experiment some behaviours are shared such as the initial movement of bitumen into the tip of the crack and the movement of the bottom of the crack upwards during the healing process. One behaviour which was not shared however was the movement of the top side of the crack. Both the initial downwards movement of the top of the interface and its lack of movement in the later stages of the experiment might be explained by adhesion of the bitumen to the glass. It is possible that here the bitumen being attached to the glass plate shortly before the experiment began led to it adhering to the surface of the glass and spreading slightly during the beginning of the experiment. This same adhesion to the glass could act to prevent the movement of the bitumen away from the glass throughout the experiment.

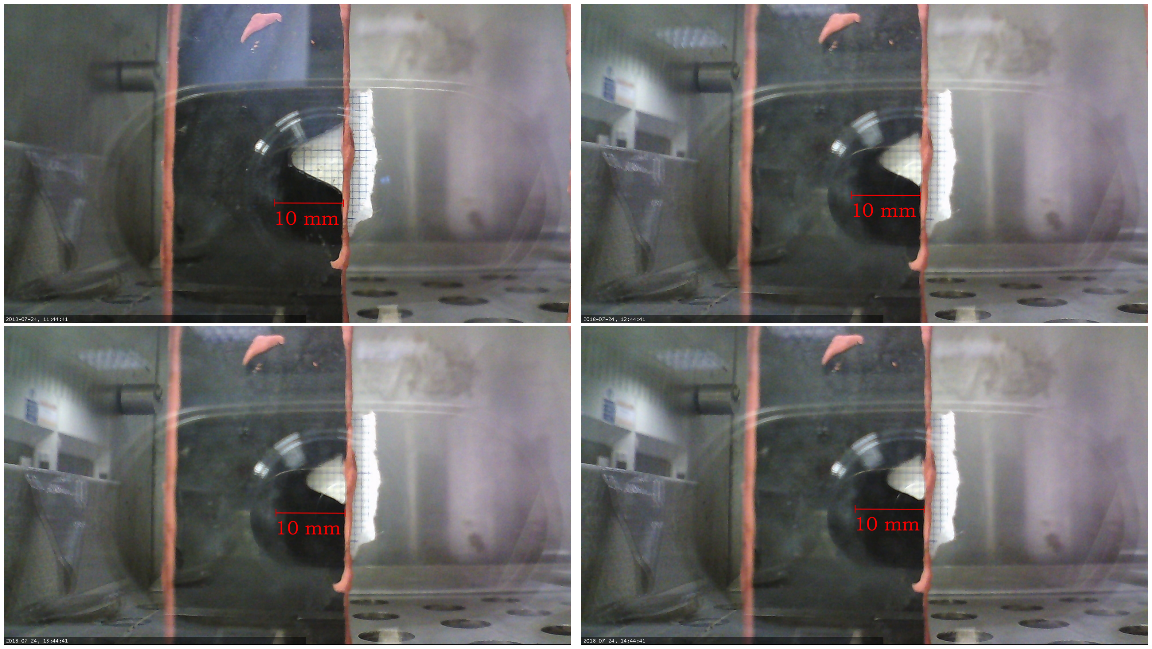

Figure 4.13: The movement of bitumen into a 10 mm tall crack initially 10 mm wide at its widest point. Top left is before heating, top right is after 60 minutes, bottom left is after 120 minutes and bottom right is after 180 minutes.

This is a possibility that the two dimensional model didn't account for.

The results of the horizontal movement of the tip of the crack in both the simulation and the experiment can be found in Fig. 4.14 and Fig. 4.15.

Here we see that the movement of the crack is much greater for the narrower crack. This would be expected because the curvature of the crack is greater the narrower it is and so the flow due to surface tension would be faster. the results of the numerical method for the wider crack show good agreement with the experimental results, with only the results for sample 1 showing significant deviation. However for the narrower crack while the numerical results follow the same general trend as the experimental results they show closer grouping than the experimental results and aren't reliable in predicting the movement of the tip of the crack with accuracy.

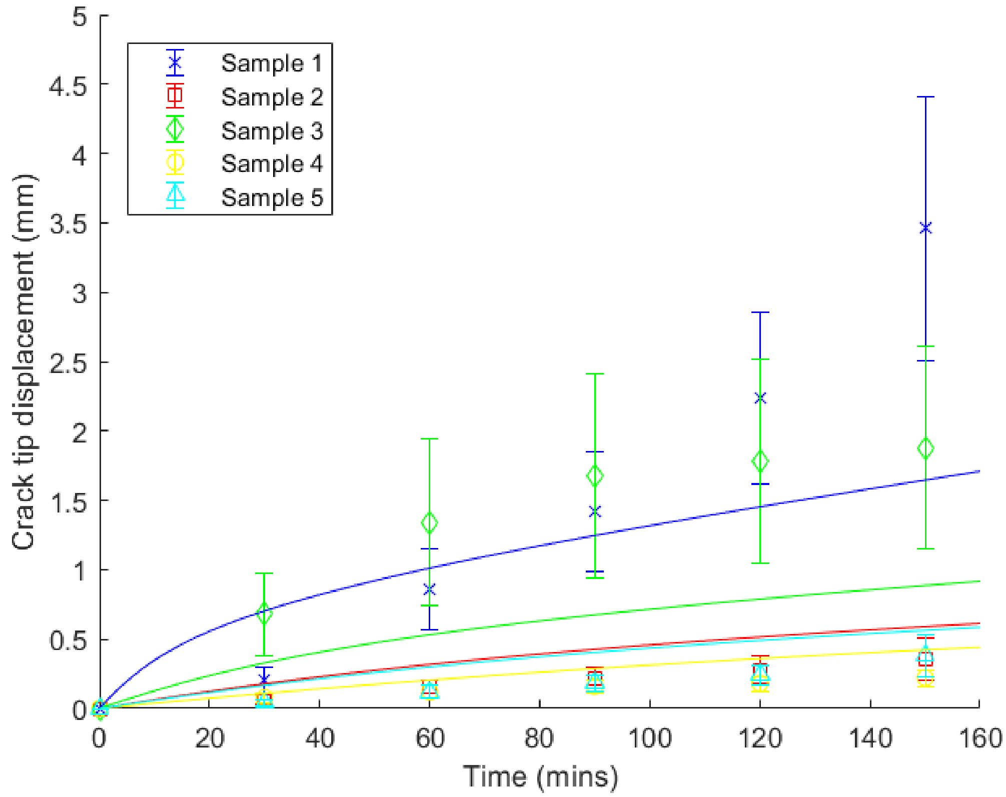

Figure 4.14: The predicted movement of the tip of a 10 mm wide horizontal crack with time compared to experimental results. The predictions are given by the solid line.

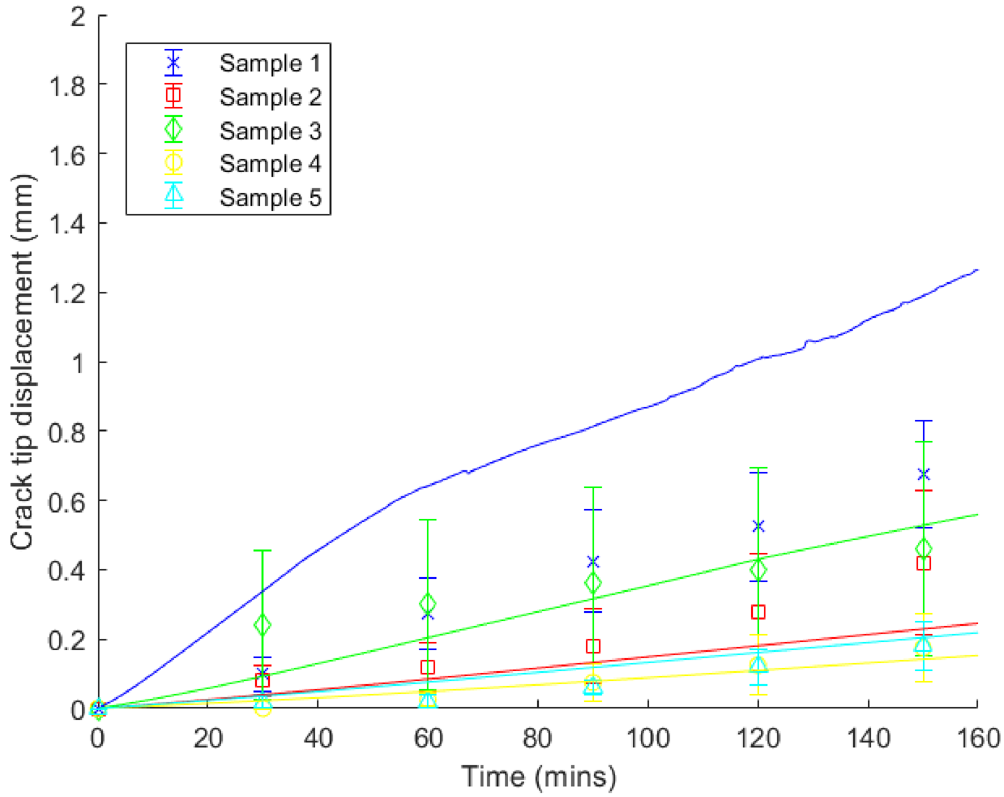

Figure 4.15: The predicted movement of the tip of a 20 mm wide horizontal crack with time compared to experimental results. The predictions are given by the solid line.

4.4.3 Multiple Vertical Cracks Results

The final class of damaged asphalt to be analysed here is one which has two vertical cracks in it. One stemming from the bottom of the asphalt and one from the top. The results of the simulation of these cracks when they have height equal to half their maximum width is in Fig. 4.16.

To produce this graph (4.31) was the chosen Green's function with the base of the domain defined as $\hat{y} = -1$ and also being bounded by $\hat{x} = \pm 3.65$. Here 101 equally spaced points were used to represent the bottom surface while 301 points were used to represent the top surface. A Bond number of $B_o = 33.681$ used. Time-steps of $\hat{t} = 0.00002$ were used to move the surface with the lines on the graph corresponding to the evolution of the surface every 4 time-steps. In this case both gravity and surface tension were included in the relevant equations.

Here the movement of bitumen into the crack is almost entirely centred at the base of the bottom crack. This is logical given the relatively high pressure at the bottom of the domain. In this case the healing follows broadly the same pattern as was seen when looking at the inverted crack independently. This pattern also includes similar instabilities in the base of the bottom crack after large time periods.

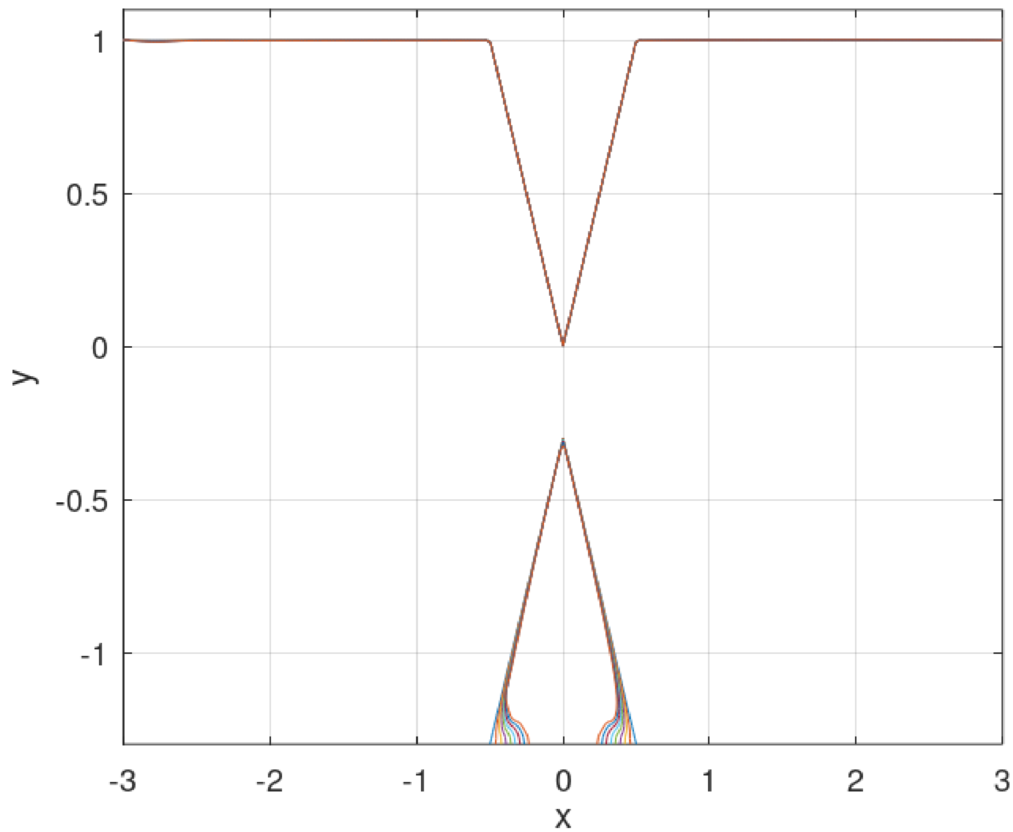

Figure 4.16: The predicted evolution of a horizontal crack with time. The blue line represents the initial cracks and the other lines the evolution of the surface. Here the Bond number was taken to be $B_o = 33.681$.

The experiments show that the healing of each crack takes place largely similarly to how each class of crack would heal on its own. An example of the healing of a sample crack can be found in Fig. 4.17. Here the top left image shows the crack at the beginning of the experiment, the top right image presents the crack after 60 mins, the bottom left after 120 mins and the bottom right after 180 mins.

Comparing the results of these experiments to the behaviours of the interface in the numerical results provides some similarities. Firstly the movement of bitumen is largely focused at the base of the bottom crack in both cases. Here the top crack sees little movement compared to the flow of the two fronts into the bottom crack. As with the case of the inverted crack the instabilities in the later stages of the movement of the bottom crack were not replicated in experiment.

The average progress of the tip of the cracks throughout these experiments can be seen in Fig. 4.18 and Fig. 4.19. These give the results of the healing of both cracks separately with the positive values representing the healing of the top crack and the negative values representing the downwards progression of the tip of the bottom crack.

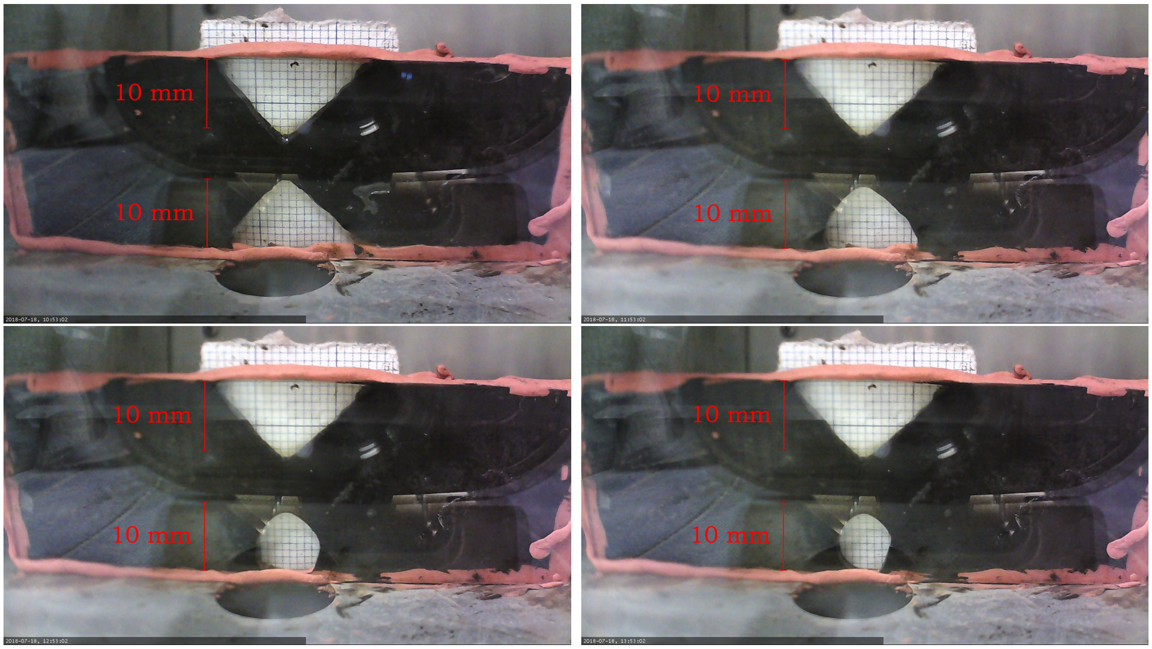

Figure 4.17: The movement of bitumen into two 10 mm tall cracks initially 20 mm wide at their widest point. Top left is before heating, top right is after 60 minutes, bottom left is after 120 minutes and bottom right is after 180 minutes.

Due to instabilities the numerical results were not stable enough to run to simulate the 150 min duration of the experiment and so could not be included here.

The results from the movement of the tip of the crack over time for this experiment are hard to categorise neatly. Disregarding the movement of sample 3 for the narrow crack as an outlier the movement of the tips of the top and bottom crack are relatively even. This would imply that the main impact of the gravity driven healing was to fill the base of the bottom crack while surface tension being roughly equal between the cracks was more impactful on the movement of the tips of the crack.

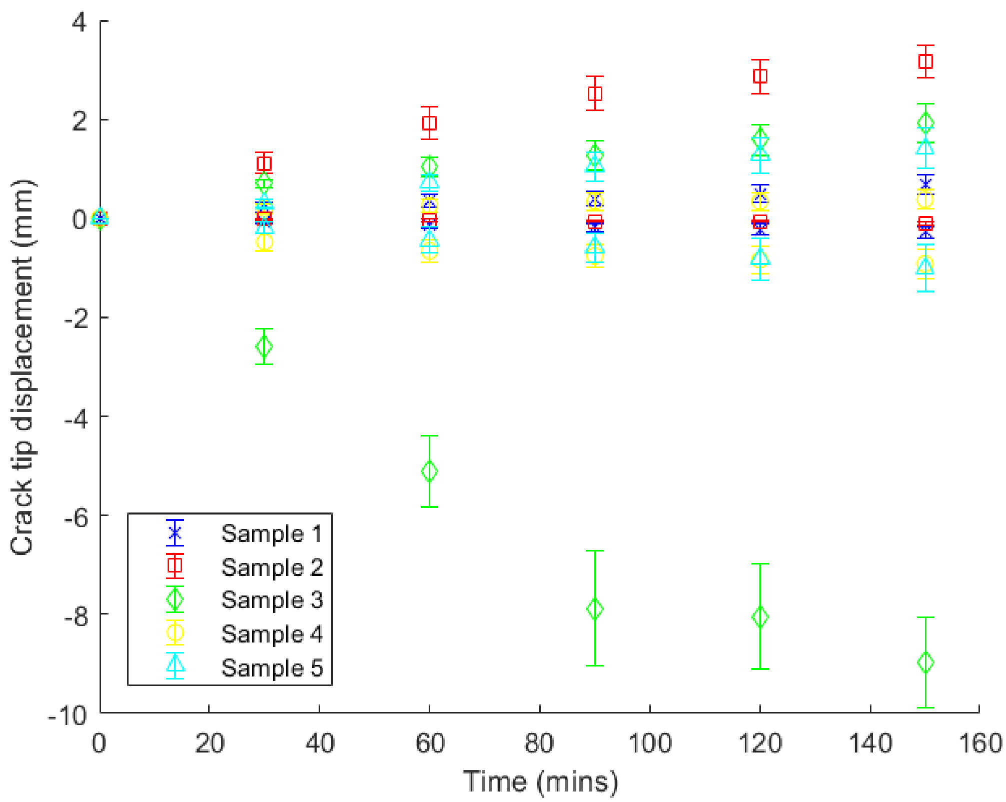

Figure 4.18: The experimental results for the movement of the tip of the two 10 mm wide vertical cracks with time. Negative results display the movement of the bottom crack downwards while positive results display the movement of the higher crack upwards.

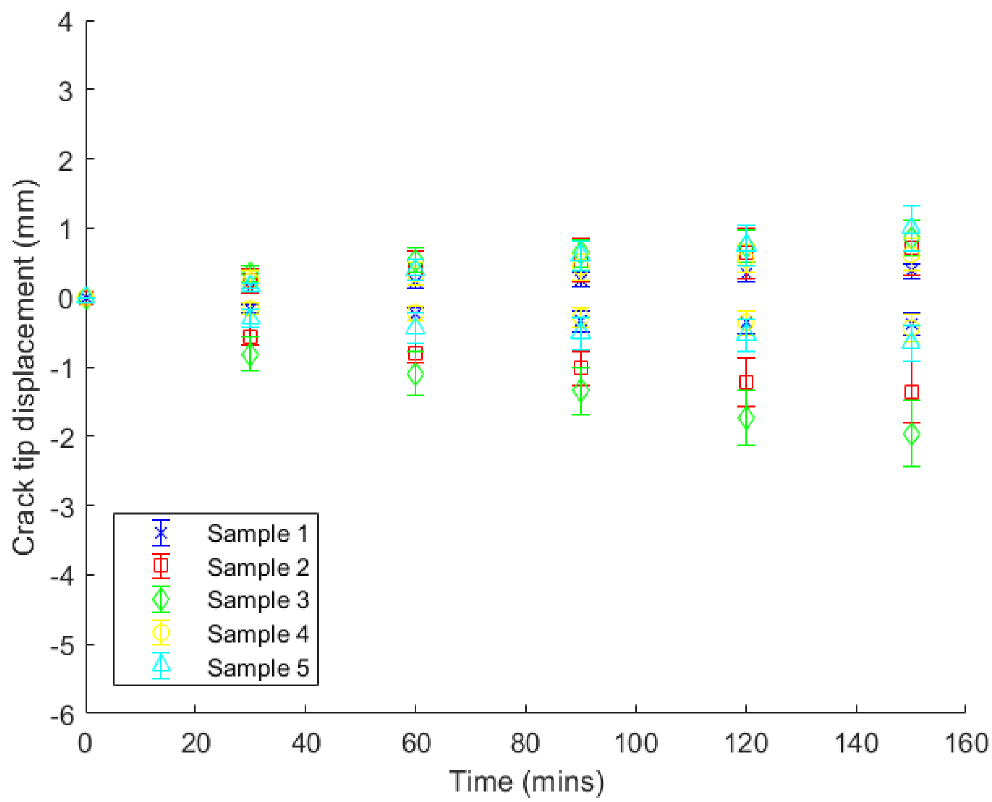

Figure 4.19: The experimental results for the movement of the tip of the two 20mm wide vertical cracks with time. Negative results display the movement of the bottom crack downwards while positive results display the movement of the higher crack upwards.

4.5 Summary and Conclusions

During this chapter a method of simulating the healing of cracks within asphalt of different orientations was formulated. This was then verified through a series laboratory experiments for each orientation.

To begin with models for the movement of asphalt into three different orientations of cracks in asphalt were constructed. This included an inverted vertical crack, a horizontal crack and two vertical cracks in the same piece of asphalt. These models assumed that flow within the domain was characterised as flow within a porous medium, including within the crack and that the flow was driven by surface tension and gravity. This was used to provide a framework to work around for the rest of the chapter

After this was completed I constructed a numerical method using boundary integral methods to create a simulation which can predict the movement of the various different classes of crack. This was done by selecting Green's functions to control the appropriate domain of the simulation.

Next a run of laboratory experiments were conducted which were directly compared to results from the model. Here the similarities and differences between the numerical and experimental results were analysed.

An avenue of future research highlighted here which would be of benefit to the field would include the progression to a three dimensional model. This would especially benefit the case of the inverted crack where the method of release of the air inside the crack would be of great interest.

Chapter 5

Summary and Conclusions

5.0.1 Research Summary

This research has focused on generating an increased understanding of the self-healing process in asphalt. This was performed by creating a series of models to simulate the movement of a variety of classes of cracks and using these models to provide direct comparison between different established healing methods for asphalt self-healing.

It began with an overview of the topic in the form of a literature review. This was done to establish a foundation for the research to take place, as well as giving an insight into the current state of the literature.

Over the course of the second chapter a model was created to describe the flow of bitumen into a crack in a porous medium under the influence of gravity and surface tension. The model assumed that flow throughout the system, including within the crack, could be classified as flow within a porous medium. A method to simulate the process was constructed using boundary integral methods which was then verified by a series of laboratory experiments.

After the model was defined the pressure fields surrounding different types of crack were found using conformal mapping. Exact solutions to an infinitesimally thin crack and a triangular crack were given as well as approximations to the pressure field at the tip of an infinitesimally thin crack and a generic crack. This step allowed for the calculation of the small time asymptotic solution to the initial movement of the interface.

This was followed by a numerical solution which was used to compute the healing of a crack with time over a number of different domains. This solution was constructed using boundary integral methods combined with selecting an appropriate Green's function for the domain in question.

The accuracy of the numerical solutions for each domain were then compared to the analytical solutions. The two solutions showed strong similarities to each other, helping to verify the numerical solution.

Next a series of novel experiments were conducted observing the flow of bitumen in a Hele-Shaw cell. The agreement between the simulations and the experimental results was used to further validate the results of the simulations.

As the final part of the chapter the results of the numerical method were used to calibrate an equation which measures the progress of the healing of a crack over time in asphalt. This equation offers a computationally cheap method of predicting the healing of a crack with time.

The third chapter focused on the comparison of different methods of triggering the self-healing process in asphalt. Firstly a method to extract a healing profile from the results of three-point bending tests was established, then this was used to evaluate the effectiveness of experiments performed as part of this research as well as those from the literature. This equation was then calibrated by comparison to results from experiments performed as part of this research and those from the literature.

The chapter started by using the gravity driven healing equation found in the previous chapter to construct a novel equation for the force required to break a partially healed beam of asphalt during three-point bending. This created an equation which was used to produce a healing profile for different forms of asphalt self-healing.

The next part of the research was the analysis of three-point bending experiments using asphalt with a high capsule content. Here the asphalt containing capsules consistently outperformed the control samples with asphalt containing 1% and 1.25% capsules by mass performing consistently well. However, the results weren't as consistent as those found elsewhere in the literature, possibly due to the larger number of capsules used relative to other sources.

A large number of three-point bending experiments were analysed, both those conducted as part of this research and from the literature. These experiments showed clear advantages to larger quantities of calcium alginate capsules being contained in asphalt as well as higher temperatures being used in the healing process.

Induction heating induced healing was the next part of the literature for which analysis was attempted. However, this exposed a vulnerability in the model. Namely that it wasn't designed to cope with the asphalt properties changing throughout the healing process as is seen here, especially the rapid rise in temperature which was present in these experiments.

As part of the analysis of the viability of using oil capsules as a method to promote self-healing in asphalt a pendulum test was performed on the asphalt containing a large quantity of capsules. This was done to ensure that incorporating a large quantity of oil capsules in a road did not reduce the friction of the road enough to stop it from being safe to drive on. The asphalt with oil capsules in was well within driving safety standards, with the lowest performing sample scoring a PTV of 65 compared to the PTV of 40 required for use in roads.

In the literature it was generally acknowledged that capsule induced healing had a maximum limit. However, the healing profiles generated in this chapter suggest that this is in fact only a temporary reduction in the increase of force required to break a healing beam using three-point bending with time as opposed to a limit of the amount the beam can heal with time. This implies that the maximum limit of healing identified in other research could be just a temporary plateau which can be overcome with enough time spent healing.

The fourth chapter of this research was dedicated to the modelling of an inverted vertical crack, a horizontal crack and two simultaneous vertical cracks in asphalt as they went through the self healing process. This featured the calculation of a numerical method using boundary integral methods and the verification of said numerical method through laboratory experiment.

To begin this section of the research a series of models were constructed to provide a mathematical framework for the calculations to follow. Here each class of crack was studied and the underlying mechanics of the flow of bitumen into the crack was set out. These models assumed that the flow was characterised as flow within a porous medium including within the cracks and was driven primarily by surface tension and gravity.

This was followed by the derivation of numerical solutions to the pressure gradient at the free surfaces of the models. These solutions were generated for each of the three crack types and over multiple different domains. The solutions were generated by using boundary integral methods combined with carefully selected Green's functions to provide the appropriate domains for the calculations. These solutions were then used to create simulations of the self-healing process for cracks in different orientations.

Experiments were then performed to validate these calculations. While there were many shared characteristics between the numerical and experimental results the similarities were weaker than those seen in the second chapter.

5.0.2 Future Avenues of Research

There are a wide range of potential avenues for further research in this area.

Firstly, the ability to vary the properties of the bitumen in the asphalt with time would provide value to the field. An example of when this could prove useful would be in the understanding of the healing of asphalt through induction heating. In this case the rapid healing results in the temperature of the bitumen changing quickly and unevenly throughout the healing period.

Another possibility for future research would be the implementation of a three dimensional model. In particular this would give a better idea of the escape route of the air in an inverted vertical crack. The knowledge of how much the asphalt is weakened by the movement of the air, if at all, would be of interest in the study of that class of crack.

One more idea for potential research projects would be the testing of long term oil capsule induced healing experiments. These could be used to test the hypothesis generated here that the perceived maximum healing limit is just a by-product of using a three-point bending test to measure the healing of asphalt.

Other research avenues include the introduction of large aggregates for the bitumen to flow around. In addition the analysis of different healing methods could give a more complete view of the topic. Finally an analysis of healing in different types of asphalt could also prove valuable.

Bibliography

Y. Agzenai, J. Pozuelo, J. Sanz, I. Perez, and J. Baselga. Advanced self-healing asphalt composites in the pavement performance field: Mechanisms at the nano level and new repairing methodologies. *Recent Patents on Nanotechnology*, 9(1):43–50, 2015.

T. Al-Mansoori, R. Micaelo, I. Artamendi, J. Norambuena-Contreras, and A. Garcia. Microcapsules for self-healing of asphalt mixture without compromising mechanical performance. *Construction and Building Materials*, 155:1091 – 1100, 2017a.

T. Al-Mansoori, R. Micaelo, I. Artamendi, J. Norambuena-Contreras, and A. Garcia. Microcapsules for self-healing of asphalt mixture without compromising mechanical performance. *Construction and Building Materials*, 155:1091 – 1100, 2017b.

T. Al-Mansoori, J. Norambuena-Contreras, and A. Garcia. Effect of capsule addition and healing temperature on the self-healing potential of asphalt mixtures. *Materials and Structures*, 51(2):53, 2018a.

T. Al-Mansoori, J. Norambuena-Contreras, R. Micaelo, and A. Garcia. Self-healing of asphalt mastic by the action of polymeric capsules containing rejuvenators. *Construction and Building Materials*, 161:330 – 339, 2018b.

C. Alessandri and V. Mallardo. Crack identification in two-dimensional unilateral contact mechanics with the boundary element method. *Computational Mechanics*, 24(2):100–109, 1999.

J. R. Barber. *Intermediate Mechanics of Materials*. Springer Science & Business Media, 2012.

G. K. Batchelor. *An introduction to fluid dynamics*. Cambridge university press, 2000.

D. Bigoni and D. Capuani. Time-harmonic green's function and boundary integral formulation for incremental nonlinear elasticity: dynamics of wave patterns and shear bands. *Journal of the Mechanics and Physics of Solids*, 53(5):1163–1187, 2005.

J. M. Boulton-Stone. A comparison of boundary integral methods for studying the motion of a two-dimensional bubble in an infinite fluid. *Computer methods in applied mechanics and engineering*, 102(2):213–234, 1993.

Y. Cao, W. W. Schultz, and R. F. Beck. Three-dimensional desingularized boundary integral methods for potential problems. *International Journal for Numerical Methods in Fluids*, 12(8):785–803, 1991.

S. N. Chandler-Wilde, I. G. Graham, S. Langdon, and E. A. Spence. Numerical-asymptotic boundary integral methods in high-frequency acoustic scattering. *Acta numerica*, 21:89–305, 2012.

D. Cheng. *Surface free energy of asphalt-aggregate system and performance analysis of asphalt concrete based on surface free energy.* Texas A&M University, 2003.

F. Collino, F. Millot, and S. Pernet. Boundary-integral methods for iterative solution of scattering problems with variable impedance surface condition. *Progress In Electromagnetics Research*, 80:1–28, 2008.

J. Crank and P. Nicolson. A practical method for numerical evaluation of solutions of partial differential equations of the heat-conduction type. *Mathematical Proceedings of the Cambridge Philosophical Society*, 43(1):50–67, 1947.

T. A. Cruse and F. J. Rizzo. A direct formulation and numerical solution of the general transient elastodynamic problem. i. *Journal of Mathematical Analysis and Applications*, 22(1):244 – 259, 1968.

J. Drelich and J. D. Miller. Surface and interfacial tension of the whiterocks bitumen and its relationship to bitumen release from tar sands during hot water processing. *Fuel*, 73(9):1504–1510, 1994.

J. Drelich, K. Bukka, J. D. Miller, and F. V. Hanson. Surface tension of toluene-extracted bitumens from utah oil sands as determined by wilhelmy plate and contact angle techniques. *Energy & fuels*, 8(3):700–704, 1994.

A. Duchesne, A. Andersen, and T. Bohr. Surface tension and the origin of the circular hydraulic jump in a thin liquid film. *Phys. Rev. Fluids*, 4:084001, 2019.

O. Egon. Surface energy and surface tension in solids and liquids. *Proc. R. Soc. Lond. A*, 316(1527):473–491, 1970.

G. M. Elphingstone Jr. *Adhesion and cohesion in asphalt-aggregate systems.* Texas A&M University, 1998.

M. Fernández-Guasti, U. Kulshreshtha, D. Singleton, and P. Roy. Green's second identity for vector fields. *International Scholarly Research Network*, 2012:973968, 7 pages, 2012.

J. Gallego, M.A. del Val, V. Contreras, and A. Páez. Heating asphalt mixtures with microwaves to promote self-healing. *Construction and Building Materials*, 42:1 – 4, 2013.

Á. García. Self-healing of open cracks in asphalt mastic. *Fuel*, 93:264 – 272, 2012.

Á. García, E. Schlangen, M. van de Ven, and G. Sierra-Beltrán. Preparation of capsules containing rejuvenators for their use in asphalt concrete. *Journal of hazardous materials*, 184(1-3):603–611, 2010.

Á. García, E. Schlangen, M. van de Ven, and Q. Liu. A simple model to define induction heating in asphalt mastic. *Construction and Building Materials*, 31:38–46, 2012.

Á. García, M. Bueno, J. Norambuena-Contreras, and M. N. Partl. Induction healing of dense asphalt concrete. *Construction and Building Materials*, 49:1 – 7, 2013.

L. Gaul, M. Kögl, and M. Wagner. *Boundary Element Methods for Engineers and Scientists an Introductory Course with Advanced Topics.* Springer, 2003.

J. M. Gere and B. J. Goodno. *Mechanics of Materials.* Cengage Learning, 2012.

J. A. Giompalo. *Permeability of hot mix asphalt concrete as affected by binder content.* PhD thesis, West Virginia University, 2010.

S. Goldman. Generalizations of the young–laplace equation for the pressure of a mechanically stable gas bubble in a soft elastic material. *The Journal of Chemical Physics*, 131(18):184502, 2009.

B. Gómez-Meijide, H. Ajam, P. Lastra-González, and A. Garcia. Effect of air voids content on asphalt self-healing via induction and infrared heating. *Construction and Building Materials*, 126:957 – 966, 2016.

A. González, J. Norambuena-Contreras, L. Storey, and E. Schlangen. Effect of rap and fibers addition on asphalt mixtures with self-healing properties gained by microwave radiation heating. *Construction and Building Materials*, 159:164–174, 2018.

P. M. Gresho and R. L. Sani. On pressure boundary conditions for the incompressible navier-stokes equations. *International Journal for Numerical Methods in Fluids*, 7(10): 1111–1145, 1987.

S. Gupte and S. Advani. Flow near the permeable boundary of a porous medium: An experimental investigation using lda. *Experiments in Fluids*, 22:408 – 422, 1997.

A. W. Hefer, A. Bhasin, and D. N. Little. Bitumen surface energy characterization using a contact angle approach. *Journal of Materials in Civil Engineering*, 18(6):759–767, 2006a.

A. W. Hefer, D. N. Little, and B. E. Herbert. Bitumen surface energy characterization by qa inverse gas chromatography. *Journal of Testing and Evaluation*, 35(3):233–239, 2006b.

C. W. Hirt and B. D. Nichols. Volume of fluid (vof) method for the dynamics of free boundaries. *Journal of computational physics*, 39(1):201–225, 1981.

T. Y. Hou, J. S. Lowengrub, and M. J. Shelley. Boundary integral methods for multicomponent fluids and multiphase materials. *Journal of Computational Physics*, 169 (2):302–362, 2001.

G. C. Hsiao and W. L. Wendland. Boundary integral methods in low frequency acoustics. *Journal of the Chinese institute of Engineers*, 23(3):369–375, 2000.

J. Hua, J. F. Stene, and P. Lin. Numerical simulation of 3d bubbles rising in viscous liquids using a front tracking method. *Journal of Computational Physics*, 227(6): 3358–3382, 2008.

Y. Huang, S. G. Mogilevskaya, and S. L. Crouch. Complex variable boundary integral method for linear viscoelasticity: Part i—basic formulations. *Engineering analysis with boundary elements*, 30(12):1049–1056, 2006.

C. Y. Hui and A. Jagota. Surface tension, surface energy, and chemical potential due to their difference. *Langmuir*, 29(36):11310–11316, 2013.

S. W. Ip and J. M. Toguri. The equivalency of surface tension, surface energy and surface free energy. *Journal of materials science*, 29(3):688–692, 1994.

M. A. Jensen and J. D. Freeze. A recursive green's function method for boundary integral analysis of inhomogeneous domains. *IEEE Transactions on Antennas and Propagation*, 46(12):1810–1816, 1998.

C. Jolicoeur. *The New Cider Maker's Handbook: A Comprehensive Guide for Craft Producers*. Chelsea Green Publishing, 2013.

C. H. Juang and S. N. Amirkhanian. Unified pavement distress index for managing flexible pavements. *Journal of Transportation Engineering*, 118(5):686–699, 1992.

E. F. Kaasschieter. Solving the buckley–leverett equation with gravity in a heterogeneous porous medium. *Computational Geosciences*, 3(1):23–48, 1999.

A. H. Khalid. *Free boundary problems in a Hele-Shaw cell*. PhD thesis, UCL (University College London), 2015.

A. C. King, J. Billingham, and S. R. Otto. *Differential Equations: Linear, Nonlinear, Ordinary, Partial*. Cambridge University Press, 2003.

E. Klaseboer, C. R. Fernandez, and B. C. Khoo. A note on true desingularisation of boundary integral methods for three-dimensional potential problems. *Engineering analysis with boundary elements*, 33(6):796–801, 2009.

L. Lee and R. J. LeVeque. An immersed interface method for incompressible navier–stokes equations. *SIAM Journal on Scientific Computing*, 25(3):832–856, 2003.

D. Lesueur. The colloidal structure of bitumen: Consequences on the rheology and on the mechanisms of bitumen modification. *Advances in Colloid and Interface Science*, 145(1–2):42 – 82, 2009.

K. Li. Fast computation technique of green's function and its boundary integrals for multilayered medium structures by using fourier series expansion and method of images. *International Journal of RF and Microwave Computer-Aided Engineering*, 8(6): 474–483, 1998.

C. M. Linton. Rapidly convergent representations for green' functions for laplace' equation. *Proceedings of the Royal Society of London. Series A: Mathematical, Physical and Engineering Sciences*, 455(1985):1767–1797, 1999.

D. N. Little and B. Amit. *Exploring Mechanism of Healing in Asphalt Mixtures and Quantifying its Impact*, pages 205–218. Springer Netherlands, 2007.

H. Liu and G. Cao. Effectiveness of the young-laplace equation at nanoscale. *Scientific Reports*, 6(1):23936, 2016.

J. Liu and J. Jin. A novel hybridization of higher order finite element and boundary integral methods for electromagnetic scattering and radiation problems. *IEEE Transactions on antennas and propagation*, 49(12):1794–1806, 2001.

N. Liu and L. Ma. Regularized tomographic piv for incompressible flows based on conservation of mass. *Applied optics*, 59(6):1667–1677, 2020.

Q. Liu. *Induction Healing of Porous Asphalt Concrete*. PhD thesis, Delft University of Technology, 2012.

S Bo Liu and Choon-Lai Tan. Two-dimensional boundary element contact mechanics analysis of angled crack problems. *Engineering Fracture Mechanics*, 42(2):273–288, 1992.

R. Lytton. Characterizing asphalt pavements for performance. *Transportation Research Record: Journal of the Transportation Research Board*, 1723:5–16, 2000.

V. Magnanimo, H. L. ter Huerne, and S. Luding. Asphalt durability and self-healing modelling with discrete particles approach. In A. Scarpas, N. Kringos, I. Al-Qadi, and A. Loizos, editors, *Proceedings of the 7th RILEM conference on cracking in pavements, 20-22 June 2012, Delft, the Netherlands*, volume 4 of *RILEM bookseries*, pages 1103 – 1114. Springer, 2012.

M. G. Markov. Effect of interfacial slip on the kinematic and dynamic parameters of elastic waves in a fluid-saturated porous medium. *Acoustical Physics*, 53(2):213–216, 2007.

P. A. Martin and F. J. Rizzo. Partitioning, boundary integral equations, and exact green's functions. *International journal for numerical methods in engineering*, 38(20): 3483–3495, 1995.

D. I. Meiron. Boundary integral formulation of the two-dimensional symmetric model of dendritic growth. *Physica D: Nonlinear Phenomena*, 23(1-3):329–339, 1986.

A. Menozzi, Á. García, M.N. Partl, G. Tebaldi, and P. Schuetz. Induction healing of fatigue damage in asphalt test samples. *Construction and Building Materials*, 74:162 – 168, 2015.

W. L. Meyer, W. A. Bell, B. T. Zinn, and M. P. Stallybrass. Boundary integral solutions of three dimensional acoustic radiation problems. *Journal of sound and vibration*, 59 (2):245–262, 1978.

Y. Mi and M. H. Aliabadi. Dual boundary element method for three-dimensional fracture mechanics analysis. *Engineering analysis with boundary elements*, 10(2):161–171, 1992.

R. Micaelo, T. Al-Mansoori, and A. Garcia. Study of the mechanical properties and self-healing ability of asphalt mixture containing calcium-alginate capsules. *Construction and Building Materials*, 123(Supplement C):734 – 744, 2016.

F. P. Miknis, A. T. Pauli, A. Beemer, and B. Wilde. Use of nmr imaging to measure interfacial properties of asphalts. *Fuel*, 84(9):1041–1051, 2005.

M. Minale. Momentum transfer within a porous medium. ii. stress boundary condition. *Physics of Fluids*, 26(12):123102, 2014.

Z. Minghao, L. Yuanjie, and C. Changjun. Boundary-integral equations and the boundary-element method for three-dimensional fracture mechanics. *Engineering analysis with boundary elements*, 13(4):333–338, 1994.

S. Mondal, M. Phukan, and A. Ghatak. Estimation of solid–liquid interfacial tension using curved surface of a soft solid. *Proceedings of the National Academy of Sciences*, 112(41):12563–12568, 2015.

A. Moroz. Quasi-periodic green's functions of the helmholtz and laplace equations. *Journal of Physics A: Mathematical and General*, 39(36):11247–11282, 2006.

T. N. Narasimhan and P. A. Witherspoon. An integrated finite difference method for analyzing fluid flow in porous media. *Water Resources Research*, 12(1):57–64, 1976.

S. P. Neuman. Theoretical derivation of darcy's law. *Acta mechanica*, 25(3):153–170, 1977.

J. C. Nicholls. *Asphalt surfacings.* CRC Press, 2014.

D. A. Nield and A. Bejan. *Convection in porous media.* Springer Science & Business Media, 2006.

J. Niessner, S. Berg, and S. M. Hassanizadeh. Comparison of two-phase darcy's law with a thermodynamically consistent approach. *Transport in porous media*, 88(1):133–148, 2011.

J. Norambuena-Contreras and A. Garcia. Self-healing of asphalt mixture by microwave and induction heating. *Materials & Design*, 106:404–414, 2016.

J. Norambuena-Contreras and I. Gonzalez-Torre. Influence of the microwave heating time on the self-healing properties of asphalt mixtures. *Applied Sciences*, 7(10):1076, 2017.

J. Norambuena-Contreras, E. Yalcin, A. Garcia, T. Al-Mansoori, M. Yilmaz, and R. Hudson-Griffiths. Effect of mixing and ageing on the mechanical and self-healing properties of asphalt mixtures containing polymeric capsules. *Construction and Building Materials*, 175:254 – 266, 2018.

J. Norambuena-Contreras, Q. Liu, L. Zhang, S. Wu, E. Yalcin, and A. Garcia. Influence of encapsulated sunflower oil on the mechanical and self-healing properties of dense-graded asphalt mixtures. *Materials and Structures*, 52(4):78, 2019a.

J. Norambuena-Contreras, E. Yalcin, R. Hudson-Griffiths, and A. García. Mechanical and self-healing properties of stone mastic asphalt containing encapsulated rejuvenators. *Journal of Materials in Civil Engineering*, 31(5):04019052, 2019b.

N. E. Nørlund. Hypergeometric functions. *Acta Mathematica*, 94(1):289–349, 1955.

E. Olsson and G. Kreiss. A conservative level set method for two phase flow. *Journal of computational physics*, 210(1):225–246, 2005.

C. Oltean, F. Golfier, and M. A. Buès. Experimental and numerical study of the validity of hele–shaw cell as analogue model for variable-density flow in homogeneous porous media. *Advances in Water Resources*, 31(1):82 – 95, 2008.

E. Papirer, J. Kuczynski, and B. Siffert. Surface properties of heavy petroleum distillation residues. *Fuel*, 64(2):283–285, 1985.

E. Papirer, J. Kuczynski, and B. Siffert. Characterization of the surface properties of heavy residues of oil distillation by inverse gas chromatography. *Chromatographia*, 23 (6):401–406, 1987.

A. T. Pauli. *Chemomechanics of Damage Accumulation and Damage-Recovery Healing in Bituminous Asphalt Binders*. PhD thesis, Delft University of Technology, 2014.

A. T. Pauli, W. Grimes, S. C. Huang, and R. E. Robertson. Surface energy studies of shrp asphalts by afm. *American Chemical Society, Division of Petroleum Chemistry, Preprints*, 48(1):14–18, 2003.

J. Pellicer, V. García-Morales, and M. J. Hernández. On the demonstration of the young-laplace equation in introductory physics courses. *Physics Education*, 35(2):126, 2000.

H. Power. The completed double layer boundary integral equation method for two-dimensional stokes flow. *IMA Journal of Applied Mathematics*, 51(2):123–145, 1993.

C. Pozrikidis. *A practical guide to boundary element methods with the software library BEMLIB*. CRC Press, 2002.

A. Prada and F. Civan. Modification of darcy's law for the threshold pressure gradient. *Journal of Petroleum Science and Engineering*, 22(4):237–240, 1999.

C. C. Puig, H. E. H. Meijer, M. A. J. Michels, L. H. G. J. Segeren, and G. J. Vancso. Characterization of glass transition temperature and surface energy of bituminous binders by inverse gas chromatography. *Energy & fuels*, 18(1):63–67, 2004.

A. Rahimian, S. K. Veerapaneni, and G. Biros. Dynamic simulation of locally inextensible vesicles suspended in an arbitrary two-dimensional domain, a boundary integral method. *Journal of Computational Physics*, 229(18):6466–6484, 2010.

S. Richardson. Hele shaw flows with a free boundary produced by the injection of fluid into a narrow channel. *Journal of Fluid Mechanics*, 56(4):609–618, 1972.

S. Richardson. On the no-slip boundary condition. *Journal of Fluid Mechanics*, 59(4): 707–719, 1973.

S. M. Roper and J. R. Lister. Buoyancy-driven crack propagation from an over-pressured source. *Journal of Fluid Mechanics*, 536:79–98, 2005.

S. Roux, F. Plouraboué, and J. P. Hulin. Tracer dispersion in rough open cracks. *Transport in Porous Media*, 32(1):97–116, 1998.

M. Z. Sarikaya, A. Akkurt, H. Budak, M. E. Türkay, and H. Yildirim. On some special functions for conformable fractional integrals. *Konuralp Journal of Mathematics (KJM)*, 8(2):376–383, 2020.

E. Schlemmer, J. Steffan, W. M. Rucker, and K. R. Richter. Accuracy improvement using a modified gauss-quadrature for integral methods in electromagnetics. *IEEE Transactions on magnetics*, 28(2):1755–1758, 1992.

W. W. Schultz and S. W. Hong. Solution of potential problems using an overdetermined complex boundary integral method. *Journal of Computational Physics*, 84(2):414–440, 1989.

X. Sheng, J. Jin, J. Song, C. Lu, and W. C. Chew. On the formulation of hybrid finite-element and boundary-integral methods for 3-d scattering. *IEEE transactions on antennas and propagation*, 46(3):303–311, 1998.

Y. D. Shikhmurzaev and J. E. Sprittles. Wetting front dynamics in an isotropic porous medium. *Journal of fluid mechanics*, 694:399–407, 2012.

R. Shuttleworth. The surface tension of solids. *Proceedings of the Physical Society. Section A*, 63(5):444–457, 1950.

M. R. Spiegel. *Schaum's outline series theory and problems of complex variables: with an introduction to conformal mapping and its application SI (metric) edition*. McGraw-Hill, 1972.

C. H. Stolze. A history of the divergence theorem. *Historia Mathematica*, 5(4):437–442, 1978.

S. Suresh. *Fatigue of Materials*. Cambridge University Press, 1998.

M. Sussman, E. Fatemi, P. Smereka, and S. Osher. An improved level set method for incompressible two-phase flows. *Computers & Fluids*, 27(5-6):663–680, 1998.

A. Tabaković and E. Schlangen. Self-healing technology for asphalt pavements. *Self-healing Materials*, pages 285–306, 2016.

C. L. Tan and R. T. Fenner. Elastic fracture mechanics analysis by the boundary integral equation method. *Proceedings of the Royal Society of London. A. Mathematical and Physical Sciences*, 369(1737):243–260, 1979.

Y. Tan and M. Guo. Using surface free energy method to study the cohesion and adhesion of asphalt mastic. *Construction and Building Materials*, 47:254–260, 2013.

F. X. Timmes and F. D. Swesty. The accuracy, consistency, and speed of an electron-positron equation of state based on table interpolation of the helmholtz free energy. *The Astrophysical Journal Supplement Series*, 126(2):501–516, 2000.

E. M. Toose, B. J. Geurts, and J. G. M. Kuerten. A boundary integral method for two-dimensional (non)-newtonian drops in slow viscous flow. *Journal of non-newtonian fluid mechanics*, 60(2-3):129–154, 1995.

S. O. Unverdi and G. Tryggvason. A front-tracking method for viscous, incompressible, multi-fluid flows. *Journal of computational physics*, 100(1):25–37, 1992.

F. J. Valdés-Parada, C. G. Aguilar-Madera, J. A. Ochoa-Tapia, and B. Goyeau. Velocity and stress jump conditions between a porous medium and a fluid. *Advances in water resources*, 62:327–339, 2013.

R. van Vossen, J. O. A. Robertsson, and C. H. Chapman. Finite-difference modeling of wave propagation in a fluid–solid configuration. *Geophysics*, 67(2):618–624, 2002.

E. I. Vargha-Butler, Z. M. Potoczny, T. K. Zubovits, C. J. Budziak, and A. W. Neumann. Surface tension of bitumen from contact angle measurements on films of bitumen. *Energy & fuels*, 2(5):653–656, 1988.

A. Vasil'ev. From the hele-shaw experiment to integrable systems: A historical overview. *Complex Anal. Oper. Theory*, 3:551–585, 2009.

J. Wang, S. L. Crouch, and S. G. Mogilevskaya. A complex boundary integral method for multiple circular holes in an infinite plane. *Engineering Analysis with Boundary Elements*, 27(8):789–802, 2003.

J. Wei and Y. Zhang. Influence of aging on surface free energy of asphalt binder. *International Journal of Pavement Research and Technology*, 3:343–351, 2010.

J. Wei, F. Dong, Y. Li, and Y. Zhang. Relationship analysis between surface free energy and chemical composition of asphalt binder. *Construction and Building Materials*, 71: 116 – 123, 2014.

S. W. J. Welch and J. Wilson. A volume of fluid based method for fluid flows with phase change. *Journal of computational physics*, 160(2):662–682, 2000.

S. Whitaker. Flow in porous media i: A theoretical derivation of darcy's law. *Transport in Porous Media*, 1(1):3–25, 1986.

S. R. White, N. R. Sottos, P. H. Geubelle, J. S. Moore, M. R. Kessler, S. R. Sriram, E. N. Brown, and S. Viswanathan. Autonomic healing of polymer composites. *Nature*, 409:794 – 797, 2001.

S. Xu and Z. J. Wang. An immersed interface method for simulating the interaction of a fluid with moving boundaries. *Journal of Computational Physics*, 216(2):454–493, 2006.

H. Zhang, Y. Bai, and F. Cheng. Rheological and self-healing properties of asphalt binder containing microcapsules. *Construction and Building Materials*, 187:138 – 148, 2018.